

Boris Shishkov
Andon Lazarov (Eds.)

Communications in Computer and Information Science

2544

Telecommunications and Remote Sensing

13th International Conference, ICTRS 2024
Virtual Event, December 19–20, 2024
Proceedings





Springer

Communications in Computer and Information Science

2544

Series Editors

Gang Li , *School of Information Technology, Deakin University, Burwood, VIC, Australia*

Joaquim Filipe , *Polytechnic Institute of Setúbal, Setúbal, Portugal*

Zhiwei Xu, *Chinese Academy of Sciences, Beijing, China*

Rationale

The CCIS series is devoted to the publication of proceedings of computer science conferences. Its aim is to efficiently disseminate original research results in informatics in printed and electronic form. While the focus is on publication of peer-reviewed full papers presenting mature work, inclusion of reviewed short papers reporting on work in progress is welcome, too. Besides globally relevant meetings with internationally representative program committees guaranteeing a strict peer-reviewing and paper selection process, conferences run by societies or of high regional or national relevance are also considered for publication.

Topics

The topical scope of CCIS spans the entire spectrum of informatics ranging from foundational topics in the theory of computing to information and communications science and technology and a broad variety of interdisciplinary application fields.

Information for Volume Editors and Authors

Publication in CCIS is free of charge. No royalties are paid, however, we offer registered conference participants temporary free access to the online version of the conference proceedings on SpringerLink (<http://link.springer.com>) by means of an http referrer from the conference website and/or a number of complimentary printed copies, as specified in the official acceptance email of the event.

CCIS proceedings can be published in time for distribution at conferences or as post-proceedings, and delivered in the form of printed books and/or electronically as USBs and/or e-content licenses for accessing proceedings at SpringerLink. Furthermore, CCIS proceedings are included in the CCIS electronic book series hosted in the SpringerLink digital library at <http://link.springer.com/bookseries/7899>. Conferences publishing in CCIS are allowed to use Online Conference Service (OCS) for managing the whole proceedings lifecycle (from submission and reviewing to preparing for publication) free of charge.

Publication process

The language of publication is exclusively English. Authors publishing in CCIS have to sign the Springer CCIS copyright transfer form, however, they are free to use their material published in CCIS for substantially changed, more elaborate subsequent publications elsewhere. For the preparation of the camera-ready papers/files, authors have to strictly adhere to the Springer CCIS Authors' Instructions and are strongly encouraged to use the CCIS LaTeX style files or templates.

Abstracting/Indexing

CCIS is abstracted/indexed in DBLP, Google Scholar, EI-Compendex, Mathematical Reviews, SCImago, Scopus. CCIS volumes are also submitted for the inclusion in ISI Proceedings.

How to start

To start the evaluation of your proposal for inclusion in the CCIS series, please send an e-mail to ccis@springer.com.

Boris Shishkov · Andon Lazarov
Editors

Telecommunications and Remote Sensing

13th International Conference, ICTRS 2024
Virtual Event, December 19–20, 2024
Proceedings

Editors

Boris Shishkov
Institute of Mathematics and Informatics
Bulgarian Academy of Sciences
Sofia, Bulgaria

Faculty of Information Sciences
University of Library Studies
and Information Technologies
Sofia, Bulgaria

IICREST
Sofia, Bulgaria

Andon Lazarov
Nikola Vaptsarov Naval Academy
Varna, Bulgaria

K.N. Toosi University of Technology
Tehran, Iran

ISSN 1865-0929

ISSN 1865-0937 (electronic)

Communications in Computer and Information Science

ISBN 978-3-031-99331-2

ISBN 978-3-031-99332-9 (eBook)

<https://doi.org/10.1007/978-3-031-99332-9>

© The Editor(s) (if applicable) and The Author(s), under exclusive license to Springer Nature Switzerland AG 2026

This work is subject to copyright. All rights are solely and exclusively licensed by the Publisher, whether the whole or part of the material is concerned, specifically the rights of translation, reprinting, reuse of illustrations, recitation, broadcasting, reproduction on microfilms or in any other physical way, and transmission or information storage and retrieval, electronic adaptation, computer software, or by similar or dissimilar methodology now known or hereafter developed.

The use of general descriptive names, registered names, trademarks, service marks, etc. in this publication does not imply, even in the absence of a specific statement, that such names are exempt from the relevant protective laws and regulations and therefore free for general use.

The publisher, the authors and the editors are safe to assume that the advice and information in this book are believed to be true and accurate at the date of publication. Neither the publisher nor the authors or the editors give a warranty, expressed or implied, with respect to the material contained herein or for any errors or omissions that may have been made. The publisher remains neutral with regard to jurisdictional claims in published maps and institutional affiliations.

This Springer imprint is published by the registered company Springer Nature Switzerland AG
The registered company address is: Gewerbestrasse 11, 6330 Cham, Switzerland

If disposing of this product, please recycle the paper.

Preface

Symbol wavelength spaced antennas as well as radar signal processing and bistatic inverse synthetic aperture radars all reflect current technical and technological advances in telecommunications, concerning satellite communication, mobile communication, networking, and so on. Next to that, we observe impressive developments in remote sensing concerning advanced recognition technologies and sensor networks as well as advanced ionospheric measurements. This relates to inspiring applications in drone technology, emergency management, and smart environments, to allow for context-aware servicing of users that is situation-specific in the sense that technical servicing depends on the situation of the user, the situation of the technical system itself, and is also aligned with external factors concerning rules, law-compliance, and public values. In all this, software technologies and artificial intelligence play a role too. Hence, research and collaborations that are crosscutting with regard to scientific disciplines and application areas are needed for advancing further the current developments in ICT (Information and Communication Technology) for the benefit of Society. This brings us together in the telecommunications and remote sensing community concerning ICTRS – the International Conference on Telecommunications and Remote Sensing, inspired by the work of Blagovest Shishkov, who established and led the ICTRS conference series until his decease in 2015.

This book contains the proceedings of ICTRS 2024 – the 13th edition of the conference, held online, during December 19-20, 2024 (<https://www.ictrs.org>). ICTRS is an annual event that brings together researchers and practitioners interested in the abovementioned topics.

Since the first event took place in Sofia, Bulgaria, in 2012, we have enjoyed twelve successful ICTRS editions. The conference has been held in different European countries (Bulgaria, The Netherlands, Luxembourg, Greece, Italy, and Spain) but took place virtually in 2020 and 2021.

The high quality of the ICTRS 2024 technical program was enhanced by intensive e-mail exchanges and online discussions on drone technology, following on from those in previous years. These, and other discussions, helped to stimulate community building and facilitated possible R&D project acquisition initiatives, which definitely contributed to maintaining the event's high quality and inspiring our steady and motivated community.

The ICTRS 2024 Program Committee consisted of 42 members from 17 countries (Australia, Brazil, Bulgaria, Canada, France, Germany, Greece, Iran, Ireland, Italy, Japan, The Netherlands, Russia, Spain, Turkey, UK, and USA, listed alphabetically) – all of them competent and enthusiastic representatives of prestigious organizations.

In organizing ICTRS 2024, we observed high ethical standards: we guaranteed at least three reviews per submitted paper (assuming reviews of adequate quality), under the condition that the paper fulfilled the ICTRS 2024 requirements. In assigning a paper for review, it was our responsibility to provide reviewers that had the relevant expertise. Sticking to a double-blind review process, we guaranteed that a reviewer would not

know who had (co-)authored the paper (we sent anonymized versions of the papers to the reviewers) and that an author would not know who had reviewed his/her paper. We required reviewers to respect the content of the paper and not disclose (parts of) its content to third parties before the conference (and also after the conference in case of rejection). We guarded against conflicts of interests by not assigning papers to reviewers who were immediate colleagues of any of the co-authors. In our decisions to accept/reject papers, we also guarded against discrimination based on age, gender, race, or religion. With regard to the EU data protection standards, we followed the GDPR requirements.

For the 13th consecutive year, ICTRS maintained a high scientific quality whilst providing a stimulating collaborative atmosphere.

ICTRS 2024 received 19 paper submissions from which 8 papers were selected for publication in the proceedings. Of these papers, seven full papers were selected for 30-minute oral presentations at the conference. The ICTRS 2024 chairs and authors hailed from Bulgaria, Canada, Greece, Iran, Kazakhstan, The Netherlands, and Russia (listed alphabetically).

ICTRS 2024 was organized and sponsored by the Interdisciplinary Institute for Collaboration and Research on Enterprise Systems and Technology (IICREST), with the cooperation of Delft University of Technology (TU Delft), Aristotle University of Thessaloniki (AUTH), and AMAKOTA Ltd. Further, ICTRS editions are held under the auspices of the International Union of Radio Science (URSI).

We would like to thank the authors, whose research and development achievements are recorded here. Next, the Program Committee members each deserve credit for the diligent and rigorous peer reviewing. Further, we would like to mention the excellent organization provided by the IICREST team (especially Canka Petrova and Aglika Bogomilova) and the support brought forward by AMAKOTA Ltd. Last but not least, we are grateful to Springer for their willingness to publish the ICTRS 2024 proceedings and we thank the editorial team for their professionalism and patience (regarding the preparation of the conference proceedings).

We wish you inspiring reading! We look forward to meeting you next year in Milan, Italy, for the 14th International Conference on Telecommunications and Remote Sensing (ICTRS 2025), details of which will be made available at <https://www.ictrs.org>.

December 2024

Boris Shishkov
Andon Lazarov

Organization

General Co-chairs

Marijn Janssen
Boris Shishkov

Delft University of Technology, The Netherlands
Institute of Mathematics and Informatics,
Bulgarian Academy of
Sciences/ULSIT/IICREST, Bulgaria

Program Co-chairs

Andon Lazarov
Dimitris Mitrakos

Nikola Vaptsarov Naval Academy, Bulgaria &
K.N. Toosi University of Technology, Iran
Aristotle University of Thessaloniki, Greece

Program Committee

Catherine Algani
Mauro Assis

Cnam, France
National Institute for Space Research and URSI,
Brazil

Vera Behar

Institute for Information and Communication
Technologies, Bulgarian Academy of Sciences,
Bulgaria

Maurice Bellanger

Cnam, France

Jun Cheng

Doshisha University, Japan

Yoshiharu Fuse

Japan Space Systems, Japan

Ivan Garvanov

ULSIT, Bulgaria

Marijn Janssen

Delft University of Technology, The Netherlands

Hristo Kabakchiev

Sofia University St. Kliment Ohridski, Bulgaria

Kazuya Kobayashi

Chuo University, Japan

Mohamed Latrach

ESEO, France

Frank Little

Texas A&M University, USA

Marco Luise

University of Pisa, Italy

Olga Maktseva

Southern Federal University, Russia

Andrea Massa

University of Trento, Italy

Wolfgang Mathis

Leibniz Universität Hannover, Germany

Lyudmila Mihaylova

Lancaster University, UK

Tomohiko Mitani	Kyoto University, Japan
Tadao Nagatsuma	Osaka University, Japan
Shoichi Narahashi	NTT Docomo, Inc., Japan
Elizabeth Nuncio	Fraunhofer Institute for High Frequency Physics and Radar Technologies, Germany
Mairtin O'Droma	University of Limerick, Ireland
Takashi Ohira	Toyohashi University of Technology, Japan
Yoshiharu Omura	Kyoto University, Japan
Jaques Palicot	CentraleSupélec, France
Brent Petersen	University of New Brunswick, Canada
Hermann Rohling	Hamburg University of Technology, Germany
Sana Salous	Durham University, UK
Hamit Serbest	Çukurova University, Turkey
Naoki Shinohara	Kyoto University, Japan
Boris Shishkov	Institute of Mathematics and Informatics, Bulgarian Academy of Sciences/ULSIT/IICREST, Bulgaria
Alexander Shmelev	Academician A. L. Mints Radiotechnical Institute, Russia
Jun-ichi Takada	Tokyo Institute of Technology, Japan
Hiroyuki Tsuji	National Institute of Information and Communications Technology, Japan
Marten van Sinderen	University of Twente, The Netherlands
Christos Verikoukis	Telecommunications Technological Centre of Catalonia, Spain
Julian Webber	ATR, Japan
Satoshi Yagitani	Kanazawa University, Japan
Tsuneki Yamasaki	Nihon University, Japan
Zhenyu Zhang	University of Southern Queensland, Australia

Contents

Full Papers

Multiuser HAP Architecture Using Symbol Wavelengths	3
<i>Samiha Lubaba and Brent R. Petersen</i>	
5G NR Waveform Application in Bistatic Inverse Synthetic Aperture Radars ...	16
<i>Andon Lazarov</i>	
Radar Detection in the Presence of Impulse Interference	28
<i>Ivan Garvanov and Magdalena Garvanova</i>	
Ionospheric Response to the Most Powerful Storm of Solar Cycle 25 in May 2024	43
<i>Olga A. Maltseva and Tatyana V. Nikitenko</i>	
UAV Detection and Recognition Technologies	60
<i>Magdalena Garvanova, Ivan Garvanov, Daniela Borissova, Nurassyl Kerimbayev, and Zhanbota Menlibay</i>	
Digital System for Registering Emergency Events in Electric Vehicles	75
<i>Radoslav Simionov, Kristian Lodkadhiev, Radostin Dolchinkov, Kamen Seymenliyski, and Silvia Letskovska</i>	
Modern Technological Solutions for Passive Buildings and Buildings with Zero Energy Consumption	87
<i>Kamen Seymenliyski, Atanas Yovkov, Eldar Zaerov, Velizar Todorov, Radoslav Simionov, and Hristo Mihaylov</i>	

Short Paper

Drone Technology and External Contextual Factors	103
<i>Boris Shishkov</i>	
Author Index	113

Full Papers



Multiuser HAP Architecture Using Symbol Wavelengths

Samiha Lubaba[✉] and Brent R. Petersen[✉]

Department of Electrical and Computer Engineering, University of New Brunswick,
Fredericton, NB, Canada

{samiha.lubaba,brent.petersen}@unb.ca

Abstract. This study presents an innovative approach to enhance communication systems on High Altitude Platforms (HAPs). Symbol-Wavelength-Spaced antennas and spread spectrum delay multiplexing are combined to increase system capacity, decrease interference, and improve spectrum efficiency. In order to determine the stability and effectiveness of the system, the study analyzes important performance measures, such as determinant, norm, and condition numbers. To enhance signal quality and reduce multiuser interference, a zero-forcing approach is used. The results demonstrate that antenna spacing at symbol-wavelength intervals provides the best performance, especially in line-of-sight communication situations. With its reliable and effective signal transmission, this architecture raises the bar for HAP-Based networks and offers exciting new developments for wireless communication systems in the future.

Keywords: Zero Forcing Technique · Spread Spectrum Delay Multiplexing · Symbol wavelength Spaced Antenna · Determinant · Norm · Condition Number

1 Introduction

Compared to terrestrial and satellite systems, High Altitude Platforms (HAPs) provide more coverage, reduced latency, and more flexible deployment. However, they also face a number of obstacles affecting its efficacy and efficiency in communication systems. The simultaneous transmission of signals by multiple users or devices frequently causes interference in communication systems. Particularly with the effective spectrum available, HAP networks must manage growing numbers of users while maintaining performance. Achieving clear and dependable communication is difficult, especially in complicated contexts with various signal channels.

To address these challenges, the suggested approach combines spread-spectrum delay multiplexing (SSDM) with antennas spaced by a symbol-wavelength, which facilitates improved spectrum management and minimizes

interference. Furthermore, the implementation of the (Zero Forcing) ZF technique enhances signal integrity by mathematically eliminating undesired signals. By optimizing antenna spacing, utilizing advanced performance metrics, and aligning interference, this solution significantly boosts system capacity and stability, thereby fostering more efficient and dependable HAP communication networks.

Advanced methods such as SSDM and symbol-wavelength-spaced antennas are critical for increased capacity, efficiency, and resistance to multipath effects in order to maximize their potential. The goal of the proposed architecture is to use these modern technologies in order to transform HAP communication networks.

By utilizing spatial diversity through many antennas, ultra-wideband technology can achieve high data rates when paired with Multiple-Input Multiple-Output (MIMO) techniques. It is necessary to space antennas by at least a symbol wavelength in order to preserve uncorrelated transmissions. MMSE (Minimum Mean Squared Error) declines with increasing antenna separation in LOS conditions, but beyond one symbol wavelength, further separation does not yield a substantial improvement, according to channel measurements using a vector network analyser; ultra wide band experiments validated the MMSE performance gain when antennas are spaced at a symbol wavelength using a constructed circular disc monopole [1, 2].

An effective method is to use beamforming multi-beam antenna systems, in which the antenna elements are arranged at intervals equal to half of the carrier wavelength. Antennas spaced by only carrier wavelength may have poor performance. By directing signals and minimizing interference, these systems guarantee robust signal reception and enhance communication quality [3, 4].

The methods for increasing cellular coverage using HAPs are covered in this study, along with performance indicators including signal-to-noise ratio (SNR) and spectral efficiency. Beam-Pointing algorithms are used in the study to improve coverage and capacity for customers in underserved or rural locations [5, 6]. Signal placement can create a great impact on optimization of HAP networks. To assess the effectiveness of Coded Orthogonal Frequency Division Multiplexing HAP (COFDM-HAP) systems, provided a channel model that matches stratospheric propagation circumstances including shadowing and Doppler spread [7]. Over several modulation schemes and bandwidths, COFDM paired with adaptive modulation and coding efficiently increases bit error rates and SNRs. The system operates most well at lower bandwidths, 5 MHz, and in optimal LOS situations. This suggests that COFDM-HAP is a reliable option for broadband wireless access over wide urban areas in the future [7].

The research addresses how to maximize system capacity for HAP constellations by utilizing matrix features, such as condition numbers. The relationship between condition numbers, determinants, and communication efficiency in linked HAP networks is highlighted by Mohammed et al. [8]. The use of matrix metrics in interference alignment (IA) methods for HAP systems, such as condition number and norms, is portraits in their work, and it is demonstrated how

they can improve system capacity and performance. IA refers to aligning interference signals in order that they barely affect the desired signals and is used in communication systems, especially MIMO systems, to maximize the data transfer capacity between numerous transmitters and receivers [9]. By making sure that interference only occupies a small portion of the communication dimensions and leaves the remaining space free for the desired signals, this method increases the total capacity of the system. Other previous research also focuses on maximizing the capacity between multiple HAPs and ground stations through IA, reducing interference and increasing the system capacity [10, 11].

2 System Model

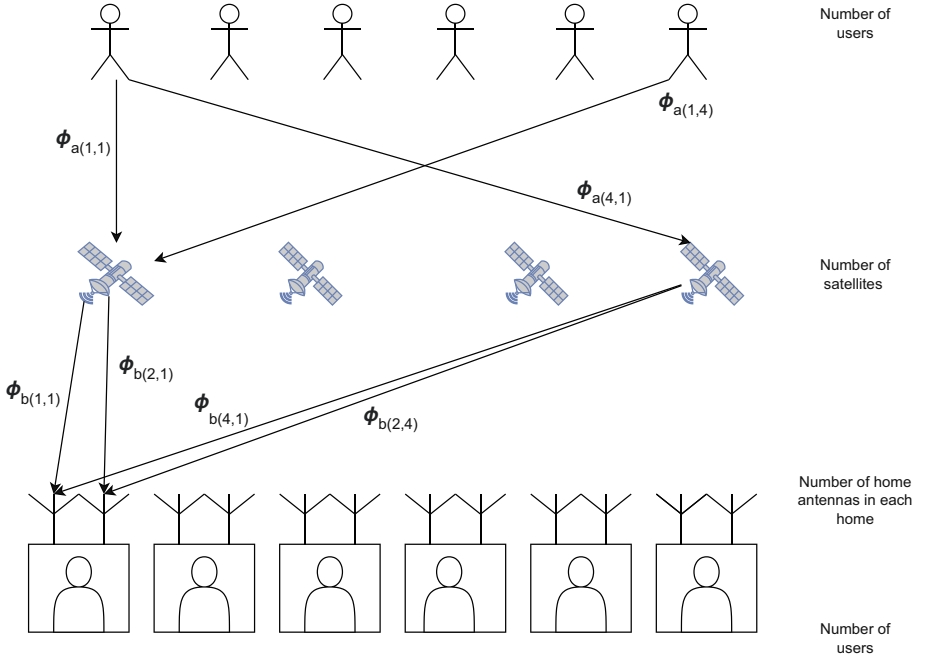


Fig. 1. Architecture for the proposed model, $N_s = 4, N_u = 6, K = 3, N_a = 2$ for each user.

The architecture for the proposed HAP system is shown in Fig. 1. The suggested architecture is dependent on several factors. Our current considerations for the model include the number of users N_u , number of satellites N_s , number

of home antennas per residence N_a , spreading factor, K , bandwidth W_b , symbol wavelength λ_s , constellation size in bits per symbol b and distances between home antennas Δg , with 0% excess bandwidth. ϕ_a denotes delay path between users and satellites and ϕ_b denotes the delay path between satellites and home antennas. This model is designed at the system capacity, which is the maximum number of users, $N_s = 6$. This maximum number is achieved from the equation

$$N_u = K N_a. \quad (1)$$

To demonstrate the performance of the system, this paper include time delays, crucial for understanding signal propagation and multipath effects in the system. The purpose of the proposed model is to evaluate the performance in different modulation schemes and architectural choices considers the worst situation having the maximum number of users.

3 Calculations

The ZF method is used. ZF offers a straightforward and efficient mathematical solution to the multiuser interference problem while also integrating effectively with the determinant, norm, and condition performance criteria. The system is less open to noise and interference when the matrix is well conditioned. The ZF filter increases the determinant to improve signal quality and reduce user interference, thus ensuring that the system operates at a stable and optimal level. The ZF situation in proposed system signifies points of stability, optimal performance, or minimized interference, which are essential for efficient communication and signal processing in systems involving multiple antennas and satellites.

The ZF method aims to eliminate interference by solving for a filter that nullifies unwanted signal components. The ZF calculation essentially solves for \overline{W}^T , where the filter matrix is designed to cancel out interference between the different users and satellite links. \overline{W}^T is the vector transpose matrix of filters in end users. This matrix represents the filter coefficients applied at the end users, transposed in Eq. 3. The matrix equations are

$$\overline{T}^T = [T \ 0 \ 0 \ 0 \ 0 \ 0] \quad \text{and} \quad (2)$$

$$\overline{W}^T = \begin{bmatrix} W_1(f - \frac{1}{T}) & W_2(f - \frac{1}{T}) & W_1(f) & W_2(f) & W_1(f + \frac{1}{T}) & W_2(f + \frac{1}{T}) \end{bmatrix}. \quad (3)$$

The determinant of the matrix Φ_c is one of the mathematical metrics used to assess the system performance. The ZF computation determines a suitable filter matrix \overline{W}^T , which removes interference. In order to prevent interference, this filter is built based on delays and other propagation properties, which are represented by Φ_c . This matrix integrates the delays, ϕ_a and ϕ_b associated with different signal paths, helping to account for signal propagation and multipath

effects. W_1, W_2 and W_3 are filter coefficients associated with different signal paths or channels that are applied at specific frequencies.

Φ_c is defined as

$$\begin{bmatrix} \phi_{c11}(f - \frac{1}{T}) & \phi_{c12}(f - \frac{1}{T}) & \phi_{c13}(f - \frac{1}{T}) & \phi_{c14}(f - \frac{1}{T}) & \phi_{c15}(f - \frac{1}{T}) & \phi_{c16}(f - \frac{1}{T}) \\ \phi_{c21}(f - \frac{1}{T}) & \phi_{c22}(f - \frac{1}{T}) & \phi_{c23}(f - \frac{1}{T}) & \phi_{c24}(f - \frac{1}{T}) & \phi_{c25}(f - \frac{1}{T}) & \phi_{c26}(f - \frac{1}{T}) \\ \phi_{c11}(f) & \phi_{c12}(f) & \phi_{c13}(f) & \phi_{c14}(f) & \phi_{c15}(f) & \phi_{c16}(f) \\ \phi_{c21}(f) & \phi_{c22}(f) & \phi_{c23}(f) & \phi_{c24}(f) & \phi_{c25}(f) & \phi_{c26}(f) \\ \phi_{c11}(f + \frac{1}{T}) & \phi_{c12}(f + \frac{1}{T}) & \phi_{c13}(f + \frac{1}{T}) & \phi_{c14}(f + \frac{1}{T}) & \phi_{c15}(f + \frac{1}{T}) & \phi_{c16}(f + \frac{1}{T}) \\ \phi_{c21}(f + \frac{1}{T}) & \phi_{c22}(f + \frac{1}{T}) & \phi_{c23}(f + \frac{1}{T}) & \phi_{c24}(f + \frac{1}{T}) & \phi_{c25}(f + \frac{1}{T}) & \phi_{c26}(f + \frac{1}{T}) \end{bmatrix} \quad (4)$$

$$\overline{T^T} = \overline{W^T} \Phi_c. \quad (5)$$

Equation 5 has the calculated matrix Φ_c which comes from the convolutions of ϕ_a and ϕ_b that is multiplied by the filter vector $\overline{W^T}$. ϕ_a is the delay matrix of six users and four satellites and ϕ_b is the delay matrix of four satellites to two home antennas for each of the six users. Φ_c referred to as the effective delay matrix or the total delay matrix, as it represents the cumulative delays experienced by signals as they travel from the users to the home antennas via HAPs or satellites. $\overline{W^T}$ is the vector is being obtained, in the context of the ZF method.

Calculations for the methods to use for observation include changing the number of satellites and users, the distance between home antennas at the symbol wavelength, the antenna placements, the number of home antennas, random and deterministic delays, and normalized values. The performance, system capacity, stability, and optimizations of the system are better understood by computations and simulations.

3.1 Variations in Number of Satellites Without Normalization

Consider Fig. 2 which compares the determinant, norm, and condition number across frequencies for $N_s = 4$ satellites and $N_s = 10$ satellites. While the determinant is lower with more zeroes for $N_s = 10$, the determinant for $N_s = 10$ exhibits more peaks and contains more zeros. In contrast, the norm and condition numbers show better performance for $N_s = 10$ in this system. λ_s is the symbol wavelength, defined as the speed of light over the symbol rate.

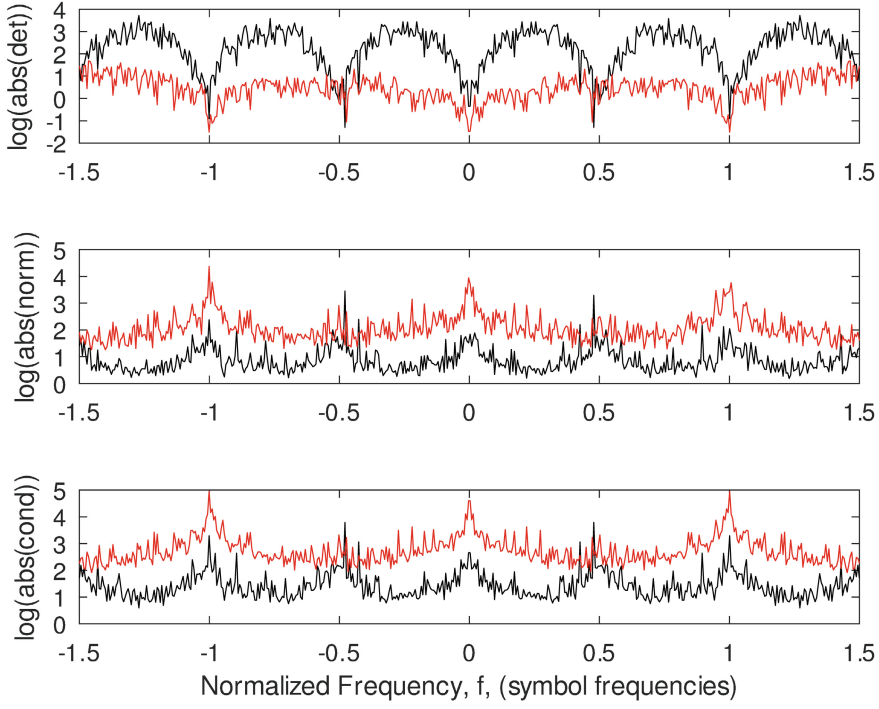


Fig. 2. Comparing unnormalized $N_s = 10$ (Red) and $N_s = 4$ (Black) when $K = 3$, $N_a = 2$, $N_u = 6$, $\Delta g = 1.0 \lambda_s$, ϕ_a random and ϕ_b deterministic. (Color figure online)

3.2 Variations in Delay Matrix from Satellites to Home Antennas

The performance criteria that is illustrating in Fig. 3 for deterministic and random ϕ_b are largely similar, with the exception that the determinant of ϕ_b contains more zeros in the deterministic case, while the norm and condition number show slight improvements in the random ϕ_b .

3.3 Variations in Number of Satellites Normalized

Figure 4 illustrates that when the signal is normalized, the determinant for $N_s = 10$ is higher than that for $N_s = 4$. Additionally, the condition number and norms appear to be nearly identical in the plot. The norm and condition number of $N_s = 10$ have more peaks and higher values.

3.4 Variations in Number of Satellites and Linear Antenna Spacing

Figure 5 shows that the determinant increases with larger Δ_g even if the $N_s = 4$, but the norms and condition numbers are lower. With a smaller Δ_g with higher

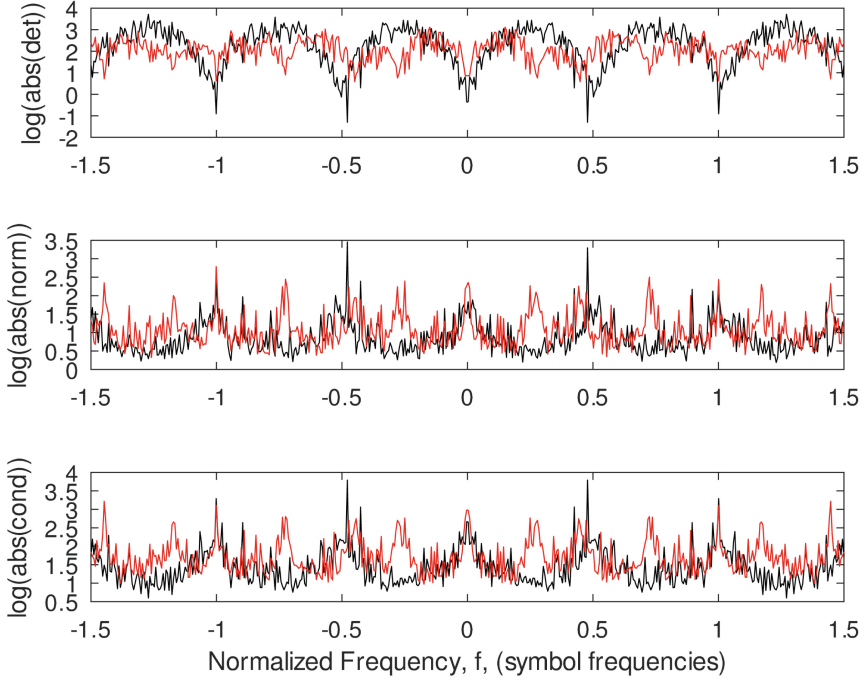


Fig. 3. Comparing unnormalized ϕ_b random (Red) and deterministic (Black) delays when $N_u = 4$, $K = 3$, $N_a = 2$, $N_u = 6$, $\Delta g = 1.0 \lambda_s$, ϕ_a random. (Color figure online)

$N_s = 10$ the determinant decreases significantly, but the norm and condition number are better.

3.5 Variations in Linear Antenna Spacing

In Fig. 6 the determinant value is higher when $\Delta g = 1.0 \lambda_s$ compared to when $\Delta g = 0.01 \lambda_s$, where it reaches its lowest value. At $\Delta g = 0.01 \lambda_s$ the norm and condition numbers exhibit better performance. However, when $\Delta g = 1.0 \lambda_s$, the determinant shows superior performance. Furthermore, the performance metrics for $\Delta g = 0.01 \lambda_s$ and $\Delta g = 0.1 \lambda_s$ demonstrate similar behavior and share notable similarities.

3.6 Variations in Home Antenna Arrangements

Consider Fig. 7, the determinant is higher for tetrahedron home antenna placements; however, the peaks of the norms and condition numbers are significantly lower. In contrast, linear home antenna placements yield better norm and condition number values than tetrahedron placements when $N_u = 12$ and $N_a = 4$.

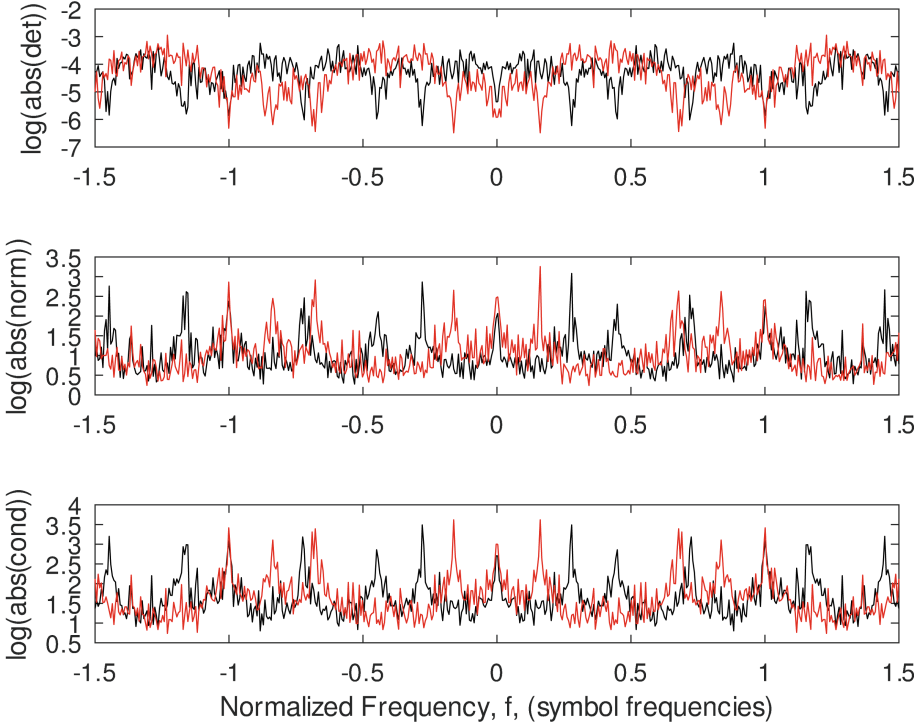


Fig. 4. Comparing normalized $N_s = 10$ (Red) and $N_s = 4$ (Black) when $K = 3$, $N_a = 2$, $N_u = 6$, $\Delta g = 1.0 \lambda_s$, ϕ_a random and ϕ_b deterministic. (Color figure online)

4 Discussion

The analysis highlights a trade-off between the number of determinants, norms, and conditions. The graphs illustrate scenarios with varying numbers of satellites, home antenna configurations, and distances between antennas. A higher number of satellites results in a lower determinant, but improved norm and condition numbers when unnormalized. In contrast, for normalized conditions, a higher number of satellites exhibits characteristics similar to those of a lower number, though with more peaks. When comparing the delay matrix between home antennas and satellites, random and deterministic configurations were evaluated. The deterministic delay matrix shows more pronounced peaks in the norm and condition numbers, while the determinant tends to approach zero more frequently.

The impact of two parameters, the number of satellites and the distance between home antennas, is particularly significant. Larger distances between antennas combined with a greater number of satellites yield better performance metrics. For a fixed number of satellites, increased distances consistently enhance all three performance criteria. In addition, tetrahedron home antenna configura-

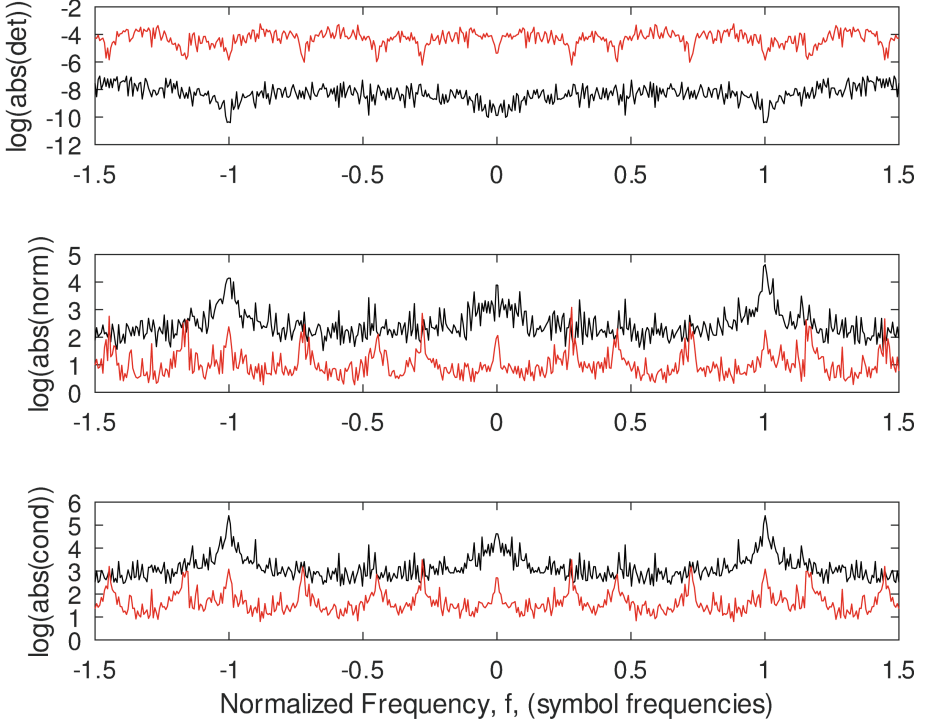


Fig. 5. Comparing normalized $\Delta g = 1.0 \lambda_s$ (Red) for $N_s = 4$ and $\Delta g = 0.01 \lambda_s$ (Black) for $N_s = 10$ when $K = 3$, $N_a = 2$, $N_u = 6$, ϕ_a random and ϕ_b deterministic. (Color figure online)

tions outperform linear placements in determinant, norm, and condition number metrics.

4.1 Limitation of the Proposed Method

Reliance on linear modulation techniques for satellite communication is one of the limitations in proposed research. These methods are limited by their quasi-static character, which means that, in contrast to the high bit rates needed for modern communication, the system's parameters change considerably more slowly. This mismatch reduces the system's adaptability to dynamic situations and impairs its system capacity to respond to quick changes in the communication environment, such as changing user requests or interference levels. As a result, the system can find it difficult to operate at its best in situations when low latency and high data throughput are necessary.

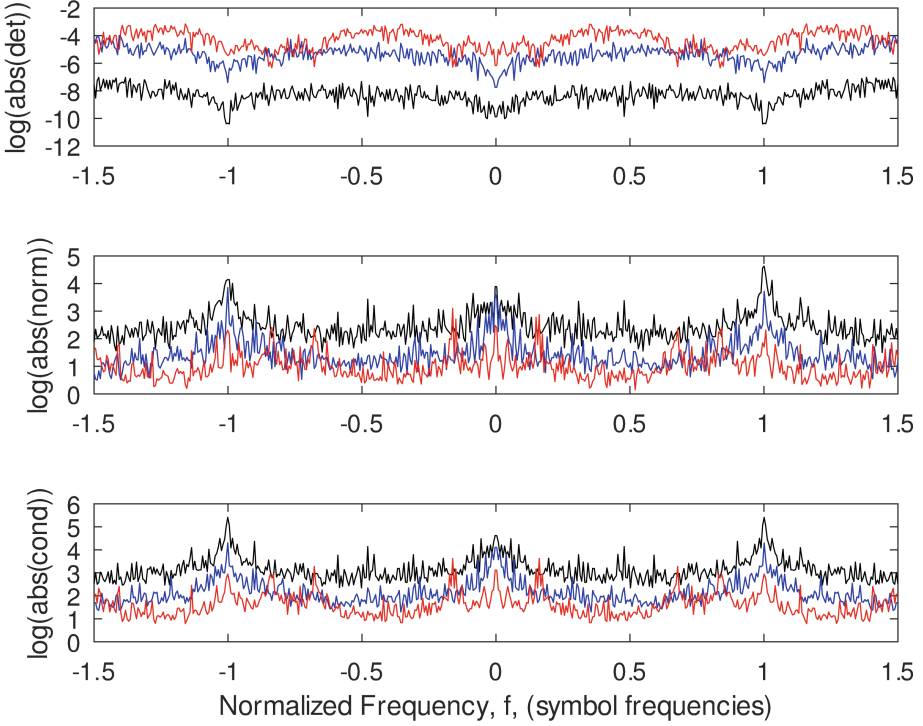


Fig. 6. Comparing normalized $\Delta g = 0.01 \lambda_s$ (Black), $\Delta g = 0.1 \lambda_s$ (Blue), $\Delta g = 1.0 \lambda_s$ (Red), when $N_s = 10$, $K = 3$, $N_a = 2$, $N_u = 6$, ϕ_a random and ϕ_b deterministic. (Color figure online)

4.2 Future Work

Future research may investigate alternative geometric configurations for antennas beyond the tetrahedral design to further improve coverage and performance. The development of algorithms that dynamically adjust antenna spacing, based on real-time traffic and environmental factors, could enhance the efficiency of the system. The integration of emerging technologies such as artificial intelligence and machine learning for real-time parameter optimization, along with compatibility with 6G and future networks, offers promising prospects. Furthermore, advanced techniques for interference mitigation and the establishment of extended performance metrics, including energy efficiency and latency, could yield a more detailed assessment of system performance. It is essential to test multiuser and multi-application scenarios, integrate HAPs with satellite networks for comprehensive global coverage, and prototype the system for validation in real-world conditions. Additionally, the design of effective spectrum sharing mechanisms, evaluation of the environmental impact of HAP deployments, and analysis of the economic feasibility for large-scale implementations—particularly

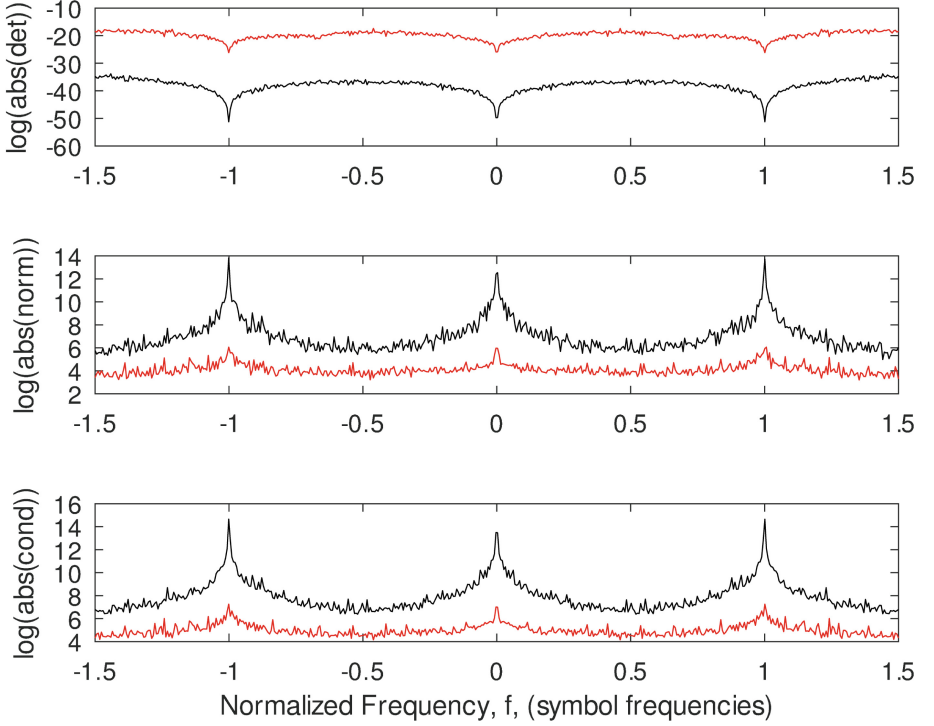


Fig. 7. Comparing normalized linear (Black) and tetrahedron (Red) home antenna arrangements when $\Delta g = 1.0 \lambda_s$, $N_s = 10$, $K = 3$, $N_a = 4$, $N_u = 12$, ϕ_a random and ϕ_b deterministic. (Color figure online)

in rural and underserved regions—will be vital for ensuring the system’s scalability, sustainability, and practicality.

5 Conclusion

By separating antennas based on symbol wavelength, the system can reduce interference and increase signal quality, resulting in greater transmission capacity and efficiency which will enhance the overall performance and reliability of the communication system by allowing improved management of signal delays and minimizing the effects of multipath. Key performance metrics such as determinant, norm, and condition numbers are used in the research to assess the suggested architecture.

The study makes use of analytical computations including the ZF solution approach, to optimize system characteristics including bandwidth and antenna spacing. This offers information on how to increase reliability, data speeds, and SNRs. The best configurations for HAP-Based communication systems are determined by analyzing the effects of varying the distance between home antennas

and their arrangements on performance measures such as the condition number, norm, and determinant.

The study opens the door for future developments in high-capacity communication networks by addressing present issues in HAP networks and with notable improvements. It establishes higher standards for HAP installations and helps in the development of reliable and efficient communication systems for a range of uses.

This research to evaluate the antenna's placement in a tetrahedron arrangement is novel. This specific geometric configuration is expected to offer unique advantages in terms of coverage and signal quality, contributing to the overall effectiveness of the proposed system. It is novel to employ determinant, norm, and condition numbers as important performance metrics for assessing the suggested system. Regarding interference reduction, signal propagation delays, and spectrum resource management, these measures offer a more comprehensive picture of the system's performance.

Another innovative feature in this context is the application of the ZF solution which offers a practical means of optimizing system parameters and achieving targeted performance metrics. The condition number will assist in determining the system's resilience to noise and other disturbances. This will pave the way for improved and reliable high-altitude communication networks.

However, if the determinant has a magnitude close to zero, it suggests that the system is not effectively managing spectrum resources or reducing interference, which limits its ability to handle high-capacity communication. This means that the system is highly sensitive to noise and interference, which can degrade the quality and reliability of the communication links.

The main innovation is the combination of spread spectrum techniques with symbol-wavelength-spaced multiple antennas. This allows for better management of spectrum resources and multipath effects, which in turn improves data transmission and capacity in HAP systems. The goal of the research is to show how this unique combination can improve HAP-Based communication networks considerably and establish new benchmarks for HAP deployments in the future. This work can be used to situations where several users require high-capacity, dependable, and efficient communication, and HAPs or satellite communication systems are required. The provision of broadband services to remote and rural areas with inadequate terrestrial infrastructure, the prompt establishment of communication links in networks for disaster relief and emergency services, the provision of ubiquitous low-latency connections for Internet of Things devices and smart grids—including bidirectional electric vehicles—and the support of the massive connectivity, low latency, and high data rates required by future communication networks are some specific applications.

Acknowledgments. The University of New Brunswick provided funding. ChatGPT assisted with spelling and grammar.

References

1. Haya, I.B., Petersen, B.R., Colpitts, B.G.: Optimum 2-D LOS MIMO performance using omni-directional antennas attained through genetic algorithms. In: Proceedings of the 6th Annual Communications Networks and Services Research Conference (CNSR 2008), vol. 1, pp. 331–338. Halifax, NS, Canada, 5–8 May 2008. <https://doi.org/10.1109/CNSR.2008.56>
2. Polu, V.V.S.N., Colpitts, B.G., Petersen, B.R.: Symbol-wavelength MMSE gain in a multiantenna UWB system. In: 4th Annual Communication Networks and Services Research Conference (CNSR'06), pp. 95–99. Moncton, NB, Canada, 24–25 May 2006. <https://doi.org/10.1109/CNSR.2006.51>
3. Shannon, C.E.: A mathematical theory of communication. *Bell Syst. Tech. J.* **27**, 379–423, 623–656 (1948). <https://doi.org/10.1002/j.1538-7305.1948.tb01338.x>
4. Abbasi, O., Yanikomeroglu, H., Kaddoum, G.: Hemispherical antenna array architecture for high-altitude platform stations (HAPS) for uniform capacity provision, 2024. <https://arxiv.org/abs/2409.03474>
5. Arum, S.C., Grace, D., Mitchell, P.D.: Delivering extended cellular coverage and capacity using high-altitude platforms. *Electronics* **11**(9), 1–27 (2022). <https://doi.org/10.3390/electronics11091508>
6. Yanikomeroglu, H.: Multi-antenna systems and interconnection strategies for CDMA wireless access networks. PhD Thesis, University of Toronto (1998). <https://hdl.handle.net/1807/12703>
7. Palma-Lazgare, I.R., Delgado-Penin, J.A.: Fixed broadband wireless access based on HAPS using COFDM schemes: channel modelling and performance evaluation. In: 2008 Australasian Telecommunication Networks and Applications Conference, pp. 62–66. Adelaide, SA, Australia, 7–10 December 2008. <https://doi.org/10.1109/ATNAC.2008.4783296>
8. Mohammed, A., Mehmood, A., Pavlidou, F.N., Mohorcic, M.: The role of high-altitude platforms (HAPs) in the global wireless connectivity. *Proc. IEEE* **99**(11), 1939–1953 (2011). <https://doi.org/10.1109/JPROC.2011.2159690>
9. Dakkak, M.R., Riviello, D.G., Guidotti, A., Vanelli-Coralli, A.: Evaluation of MU-MIMO digital beamforming algorithms in B5G/6G LEO satellite systems. In: 2022 11th Advanced Satellite Multimedia Systems Conference and the 17th Signal Processing for Space Communications Workshop (ASMS/SPSC), pp. 1–8. Graz, Austria (2022). <https://doi.org/10.1109/ASMS/SPSC55670.2022.9914720>
10. Sudheesh, P.G., Magarini, M., Muthuchidambaramanathan, P.: Multiple-high altitude platforms aided system architecture for achieving maximum last mile capacity in satellite communication. *Telecommun. Syst.* **70**(1), 27–35 (2018). <https://doi.org/10.1007/s11235-018-0466-9>
11. Xing, Y., Hsieh, F., Ghosh, A., Rappaport, T.S.: High altitude platform stations (HAPS): architecture and system performance. In: 2021 IEEE 93rd Vehicular Technology Conference (VTC2021-Spring), pp. 1–6. Helsinki, Finland, 25–28 April 2021. <https://doi.org/10.1109/VTC2021-Spring51267.2021.9448899>



5G NR Waveform Application in Bistatic Inverse Synthetic Aperture Radars

Andon Lazarov^{1,2,3} (✉)

¹ Information Technologies Department, Nikola Vaptsarov Naval Academy, Varna, Bulgaria
a.lazarov@naval-acad.bg

² K.N. Toosi University of Technology, Tehran, Iran

³ Burgas Free University, Burgas, Bulgaria

Abstract. In the present work, Bi-static Inverse Synthetic Aperture Radar (BISAR) concept with a 5G NR waveform is considered. BISAR scenario with uncooperative transmitter and specially designed receiver, and flying target as helicopter is discussed. The positions of the transmitter, receiver and flying target are defined by vector kinematic equations. Mathematical models of 5G NR waveform and BISAR signal reflected from a target with complex geometry are described. Two dimensional (2-D) image reconstruction is realized by applying correlation with an emitted waveform or Fourier transform on a range direction, and Fourier transform on an azimuth direction. Simulation experimental results are provided to illustrate the correctness of mathematical models and imaging algorithms.

Keywords: 5G NR waveform · Bi-static Inverse Synthetic Aperture Radar · BISAR geometry and signal modelling · BISAR image reconstruction

1 Introduction

Bi-static Inverse Synthetic Aperture Radar (BISAR) technology for imaging of a flying object is based on spatial distributed non-cooperative transmitter of opportunity and a specially designed receiver, both placed on fix positions, a moving target, and with application of synthetic aperture radar principal in signal formation and image reconstruction. BISAR is an attractive technology due to its independency of meteorological conditions, day-night optical visibility and illumination. BISAR can be successfully applied in detection and imaging of Unman Air Vehicles (UAV). The waveforms of various broadcast, GPS and communication radio transmitters and base stations are used to illuminate objects such as DVB-T, DVB-S, GNSS, Wi-Fi, TDMA, CDMA and OFDM signal structures.

Recently, fifth generation New Radio (5G NR) communication signals attract attention of radar society. The 5G NR waveform distinguishes with comparably wide bandwidth, which makes it applicable in inverse synthetic aperture radar imaging systems. The idea is to use the 5G NR reference signal [1, 2] for illumination and based on the object movement to form up an inverse synthetic-aperture radar (ISAR) system. Then, a sounding reference signal (SRS) is used for monostatic inverse SAR system in the

uplink communication scenario, while the positioning reference signal (PRS) is used for bi-static-inverse SAR in the downlink communication scenario.

The overview of 5G NR signals is suggested in [1, 2]. The BISAR application of the 5G NR waveform is discussed in [3]. An analytical description of the 5G NR waveform and its BISAR resolution properties is presented in [4]. Sensing and positioning based on 5G NR waveform and network passive radar is discussed in [5]. In [6], a single base station positioning system in 5G networks is proposed. It can jointly estimate the distance (time of arrival) and direction (angle of arrival based on Expectation-Maximization algorithm and a subspace-spaced algorithm by utilizing the wideband 5G OFDM signal and vector antenna and uplink sounding reference signals in a Line-of-Sight scenario). Based on its low power consumption, long detection distance, and good concealment, and strong anti-interference ability, passive OFDM localization technology of 5G OFDM radiation sources using synthetic aperture principle is in the focus of many authors. Space-born passive location of 5G OFDM radiation sources based on Virtual Synthetic Aperture is discussed in [7]. A 5G synchronization signal block's (SSB) periodically transmitted modulated pulses used in 5G-based passive coherent location (PCL) system processing is analysed in [8]. In [9], the impact of the uplink signal on the performance of the 5G-based passive radar is analyzed. It is illustrated that the implications of uplink traffic are insignificant, which is of substantial meaning for 5G passive radar application with significant reduction of computational complexity. Passive radar principles, the theoretical fundamentals of the 5G signal structure, and results of target detection using a fully operational and cooperative 5G network as a source of illumination in a passive radar scenario are presented in [10]. The electromagnetic waveforms generated by the cellular base station allow for remote sensing of a moving object in bistatic geometry. Simulate and real measurements illustrate the feasibility of passive radar based on new generation radio networks used as an illuminator of opportunity.

The aim of the present work is the analytical description of the BISAR geometry, 5G NR waveform, BISAR signal model and imaging algorithm. The problem is solved by following stages. By vector equations, the position of the uncooperative transmitter, target's scattering point and receiver in BISAR scenario are described. A 5G NR waveform and based on it BISAR signal model are defined. BISAR imaging equations are derived.

The paper is structured in six sections including Introduction. Section 2 presents BISAR scenario and positions vector equations. Section 3 describes analytically the 5G NR waveform and BISAR signal model. Section 4 presents the steps of the imaging algorithm. Section 5 provides simulation experimental results. Section 6 summarizes the contributions of the present work.

2 BISAR Scenario and Equations

2.1 BISAR Scenario

The BISAR geometry is depicted in a coordinate system of observation $Oxyz$ (Fig. 1). Assume a 5G NR transmitter T localized by vector \mathbf{R}^s and receiver S localized by vector \mathbf{R}^r , and an UAV as a target. Target's scattering points are defined by vector coordinates \mathbf{G} in coordinates $OXYZ$.

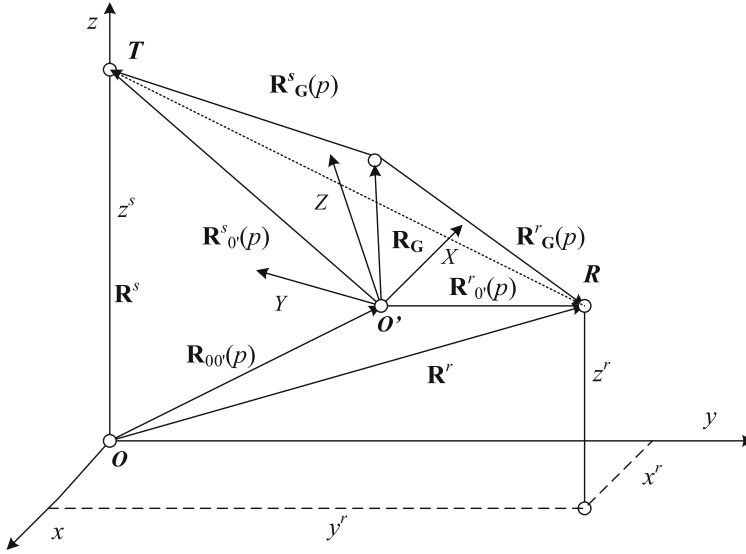


Fig. 1. BISAR Geometry

2.2 BISAR Vector Equations

\mathbf{R}_G is the position vector of G -th scattering point in the coordinate system $OXYZ$ and $\mathbf{R}_{00'}(p)$ is the current position vector of the target mass centre at the moment p . Based on the geometry in Fig. 1, the following kinematical vector equations hold.

Distance vector from the transmitter to the mass centre of the target

$$\mathbf{R}^s(p) = \mathbf{R}^s - \mathbf{R}_{00'}(p) = \mathbf{R}^s - \mathbf{R}_{00'}(0) - V \cdot p T_p, \quad (1)$$

where V is the target's velocity vector, T_p is azimuth samples period, $p = \overline{0, N-1}$ is the azimuth index, N is the full number azimuth samples.

Distance vector from the mass centre of the target to the receiver

$$\mathbf{R}^r(p) = \mathbf{R}^r - \mathbf{R}_{00'}(p) = \mathbf{R}^r - \mathbf{R}_{00'}(0) - V_p T_p. \quad (2)$$

Distance vector from the transmitter to the G -th scattering point of the target

$$R_G^s(p) = R^s(p) + AR_G = R^s - R_{00}(0) - V.pT_p + AR_G, \quad (3)$$

where A is Euler transformation matrix.

Distance vector from the G -th scattering point of the target to the receiver

$$\mathbf{R}_G^r(p) = \mathbf{R}^r(p) - \mathbf{A}\mathbf{R}_G = \mathbf{R}^r - \mathbf{R}_{00}(0) - \mathbf{V}.T_p - \mathbf{A}\mathbf{R}_G. \quad (4)$$

The round trip distance transmitter G -th scattering point of target-receiver is defined as

$$R_G(p) = |R_G^s(p)| - |R_G^r(p)|. \quad (5)$$

Equations from (1) to (5) can be used for three dimensional (3-D) geometry, kinematic, and BISAR signal modelling.

3 Analytical Description of the 5G NR Waveform and BISAR Signal Modelling

3.1 5G NR Waveform

The waveform of 5G NR (5 Generation New Radio) has a structure of Cyclic Prefix – Orthogonal Frequency Division Multiplexing (CP-OFDM) with variable subcarrier spacing termed “numerology”. According to 3GPP, the downlink transmission is organized into radio frames, each with $T_F = 10$ ms duration. One radio frame consists of 10 sub frames, each sub frame is $T_{SF} = 1$ ms long. The two-dimensional (2-D) model of 5G NR waveform used for aperture synthesis can be expressed as

$$S(k, p) = a_{kl}^\mu \text{rect} \frac{t - pT_p}{T_S} \cdot \exp[j2\pi k(f_0 + k\Delta f)(t - pT_p)] \quad (6)$$

where $\text{rect} \frac{t - pT_p}{T_S} = \begin{cases} 1, & \text{if } 0 \leq \frac{t - pT_p}{T_S} \leq 1 \\ 0, & \text{otherwise} \end{cases}$ is the rectangular window function selecting

a particular symbol used for aperture synthesis, T_S is the symbol duration,
 a_{kl}^μ is the value of the resource element (k, l), k denotes a frequency index,
 l denotes a symbol time index,
 (k, l) are coordinates of resource element in the resource grid,
 (k', l) are coordinates of resource element in the resource block,
 l is the time symbol number in one sub frame and accepts values in the interval from
 $l = 0$ to $l = 14 \times 2^\mu - 1$,
 $T_p = r.T_{SF}$, is the azimuth measurement period,
 $r = 1, 2, \dots$ is the sub frame number in one measurement period, p is the azimuth measurement index,

$t = pT_p + k.\Delta T$ is the current discrete time, k denotes the subcarrier's index as well as a time range index and accepts values from $k = 0$ to $K = N_{RB}^\mu \cdot N_{SC}^{RB} - 1$, μ denotes the numerology or subcarrier spacing configuration, which values range from 0 to 4, corresponding to subcarrier spacing of 15, 30, 60, 120, and 240 kHz respectively, defined by [1]

$$\Delta f = 2^\mu \times 15 \text{ kHz}, \quad (7)$$

N_{RB}^μ denotes the number of resource blocks for a particular μ ,

N_{SC}^{RB} denotes the number of subcarriers in one resource block,

$N_{RB}^\mu \cdot N_{SC}^{RB}$ denotes the number of subcarriers in one sub frame (one resource grid),

For $\mu = 0$, from $l = 0$ to 13, one sub frame is 1 ms long ($T_{SF} = 1$ ms), and consists of one slot. There are 14 OFDM symbols in one slot. Thus, there are 140 OFDM symbols in one radio frame. The OFDM symbol time duration T_S with cycle prefix is defined by

$$T_S = \frac{1 \text{ ms}}{14} = 0.07142 \text{ ms} \quad (8)$$

The OFDM symbol time duration T_S without cycle prefix is defined by

$$T_S = \frac{1}{\Delta f} = \frac{1}{15 \text{ kHz}} = 0.06666 \text{ ms} \quad (9)$$

One Physical Resource Block (*PRB*) consists of $N_{SC}^{RB} = 12$ sub carriers with frequency spacing $\Delta f = 15$ kHz. Thus, the *PRB* bandwidth $\Delta F_{PRB} = 180$ kHz.

For $\mu = 1$, from $l = 0$ to 27, one radio frame of 10 ms long consists of 10 sub frames, one sub frame of 1 ms long consists of two slots, each slot of 0.5 ms long, i.e. 10 sub-frames consist of 20 slots. In one slot there are 14 OFDM symbols.

The OFDM symbol time duration T_S with cycle prefix is defined by

$$T_{S_{cp}} = \frac{0.5 \text{ ms}}{14} = 0.0357 \text{ ms} \quad (10)$$

The OFDM symbol duration without cyclic prefix is defined by

$$T_S = \frac{1}{\Delta f} = \frac{1}{30 \text{ kHz}} = 0.0333 \text{ ms} \quad (11)$$

In one sub frame there are 28 OFDM symbols, thus in one radio frame there are 280 OFDM symbols.

One Physical Resource Block consists of $N_{SC}^{RB} = 12$ sub carriers with frequency spacing $\Delta f = 30$ kHz, i.e. the *PRB* bandwidth is calculated as

$$\Delta F_{PRB} = N_{SC}^{RB} \times \Delta f = 12 \times 30 \text{ kHz} = 360 \text{ kHz} \quad (12)$$

For range resolution 1.5 m, the necessary bandwidth is 99 MHz, then the number of resource blocks N_{RB}^μ is defined by

$$N_{RB}^\mu = \frac{\Delta F}{\Delta F_{PRB}} = \frac{99 \times 10^6}{360} = 275. \quad (13)$$

Hence, the maximum bandwidth $\Delta F = 99$ MHz of the emitted 5G waveform is obtained for 275 *PRB*, 12 subcarriers in each *PRB*, and with frequency spacing $\Delta f = 30$ kHz.

The number of frequency samples on range direction is defined by $K = \Delta F / \Delta f = 3300$. Accept $K = 4096$ or 2048. The range resolution is defined by

$$\Delta R = 3 \cdot 10^8 / 2 \Delta F = 1.51 \text{ m}. \quad (14)$$

The time symbol's sample duration.

In case $K = 4096$

$$\Delta T = \frac{1}{K \cdot \Delta f} = \frac{1}{4096 \cdot 30 \text{ kHz}} = 8.138 \times 10^{-9} \text{ s} \quad (15)$$

$$\text{i.e. } K = \frac{T_S}{\Delta T_{4096}} = \frac{33.33 \times 10^{-6}}{8.138 \times 10^{-9}} = 4096. \quad (16)$$

In case $K = 2048$

$$\Delta T = \frac{1}{K \cdot \Delta f} = \frac{1}{2048 \cdot 30 \text{ kHz}} = 16.27 \times 10^{-9} \text{ s} \quad (17)$$

$$\text{i.e. } K = \frac{T_S}{\Delta T_{2048}} = \frac{33.33 \times 10^{-6}}{16.27 \times 10^{-9}} = 2048. \quad (18)$$

In case one symbol in each sub frame is used for target illumination, the symbol repetition period for aperture synthesis is 1 ms or symbol repetition frequency is 1 kHz. In case one symbol in two sub frame is used for target illumination the symbol repetition period for aperture synthesis is 2 ms or symbol repetition frequency is $F_S = 0.5$ kHz. The total number of symbols N_S for aperture synthesis depends on the target velocity and the azimuth resolution that can be achieved. It can varies from 64 to 1024 or 2048.

For $\mu = 4$, $l = 233$, one sub frame consists of 16 slots, one radio frame consists of 10 sub frame, i.e. 160 slots, k varies from $k = 0$ to $k = N_{RB}^\mu \cdot N_{SC}^{RB} - 1$. One sub frame consists of $N_{RB}^\mu \cdot N_{SC}^{RB}$ subcarriers, one resource block consists of $N_{SC}^{RB} = 12$ subcarriers. The number of resource blocks is calculated based on the frequency bandwidth required to realize particular range resolution.

3.2 BISAR Signal Model

The BISAR signal reflected from a particular scattering point with vector coordinates \mathbf{G} is a delayed copy of the CP-OFDM 5G NR waveform, and based on stop and go principal of signal registration the BISAR signal model in a discrete form can be written as

$$S_G(k, p) = a_{\mathbf{G}} \text{rect} \frac{t - pT_p - t_{\mathbf{G}}(p)}{T_S} \cdot \exp[j2\pi k(f_0 + k\Delta f)(t - t_{\mathbf{G}}(p) - p.T_p)], \quad (19)$$

where $a_{\mathbf{G}}$ is the reflectivity coefficients

$$t = pT_p + t_{\mathbf{G}min}(p) + k\Delta T \quad (20)$$

is the current time

where \mathbf{G} is the three-dimensional (3D) vector coordinates.

For particular p it can be written

$$S_G(k, p) = a_{\mathbf{G}} \text{rect} \frac{t_{\mathbf{G}min}(p) + k\Delta T - t_{\mathbf{G}}(p)}{T_S} \cdot \exp[j2\pi k(f_0 + k\Delta f)(t_{\mathbf{G}min}(p) + k\Delta T - t_{\mathbf{G}}(p))] \quad (21)$$

$t_{\mathbf{G}}(p) = \frac{R_{\mathbf{G}}^s(p) + R_{\mathbf{G}}^r(p)}{c}$ denotes a signal time delay from \mathbf{G} -th scattering point, c is the light velocity in vacuum.

Define and arrange $t_{\mathbf{G}}(p)$ in ascending order.

The BISAR signal reflected from all scattering points is an algebraic sum defined as

$$s(k, p) = \sum_{\mathbf{G}} S_G(k, p). \quad (22)$$

4 BISAR Image Reconstruction Algorithm

The image reconstruction procedure includes two steps – range compression and azimuth compression. The range compression is a cross correlation between a received BISAR signal and the emitted waveform, i.e.

$$I(\hat{k}, p) = \sum_k s(k, p) \cdot S(k - \hat{k}, p), \quad (23)$$

or by IFT over a range coordinate of the received BISAR signal

$$I(\hat{k}, p) = \sum_{k=0}^{K-1} s(k, p) \cdot \exp\left(\frac{2\pi k \cdot \hat{k}}{K}\right), \quad (24)$$

where \hat{k} is the range coordinate of the scattering point at the moment of imaging.

The azimuth compression of the range compressed signal, i.e. the final complex BISAR image reconstruction procedure is performed by inverse Fourier transform over an azimuth coordinate of the range compressed signal.

$$I(\hat{k}, \hat{p}) = \frac{1}{N} \sum_p I(\hat{k}, p) \cdot \exp\left(-j \frac{2\pi \cdot p \cdot \hat{p}}{N}\right), \quad (25)$$

where \hat{p} denotes the scattering point's discrete azimuth coordinate in the BISAR image.

5 Simulation Experiment

A simulation experiment is carried out to prove the correctness of geometrical and signal models and imaging algorithms, as well.

a. Parameters of the 5G NR waveform

Numerology (sub carrier spacing) $\mu = 1$ (30 kHz), the number of resource blocks $N_{RB}^\mu = 275$.

The number of sub carriers in the sub-frame $N_{RB}^\mu \cdot N_{SC}^{RB} = 4086$,

Time symbol's sample duration: $\Delta T = 16.27 \text{ ns}$,

For $\mu = 1$, the following parameters can be defined:

Numerology: $\mu = 1$.

Subcarrier spacing: $\Delta f = 30 \text{ kHz}$.

OFDM symbol duration: $33.33 \text{ } \mu\text{s}$.

Cycle prefix duration: $2.34 \text{ } \mu\text{s}$.

OFDM symbol duration including cycle prefix duration $T_{S_{cp}} = 35.68 \text{ } \mu\text{s}$.

Carrier frequency $f_0 = 6 \text{ GHz}$.

Measurement repetition period $T_p = 1 \text{ ms}$.

Azimuth measurement symbol number $N_S = 1024$.

b. BISAR Scenario

Assume flying target in a 3-D Cartesian coordinate space $Oxyz$, target's velocity $V = 10 \text{ m/s}$, velocity guiding angles $\alpha = \pi/4$, $\beta = \pi/4$, $\gamma = \pi/2$, and mass-centre coordinates: $x_{00}(0) = 25 \text{ m}$; $y_{00}(0) = 50 \text{ m}$; $z_{00}(0) = 50 \text{ m}$.

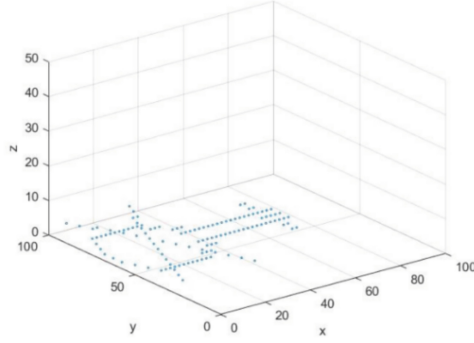


Fig. 2. Target geometry (UAV - helicopter)

5G NR transmitter coordinates: $x_S = -250$ m; $y_S = 510$ m, $z_S = 150$ m.

5G NR receiver: $x_R = 300$ m; $y_R = -510$ m; $z_R = 52$ m.

The geometry of the target, a UAV - helicopter, is described in a 3-D coordinates by scattering points spaced at $\Delta X = \Delta Y = \Delta Z = 0.5$ m (Fig. 2).

c. Experimental results and Discussion

Based on the expression (6), a signal matrix $S(k, p)$ is calculated. The real part of the $S(k, p)$ complex matrix is illustrated in Fig. 3.

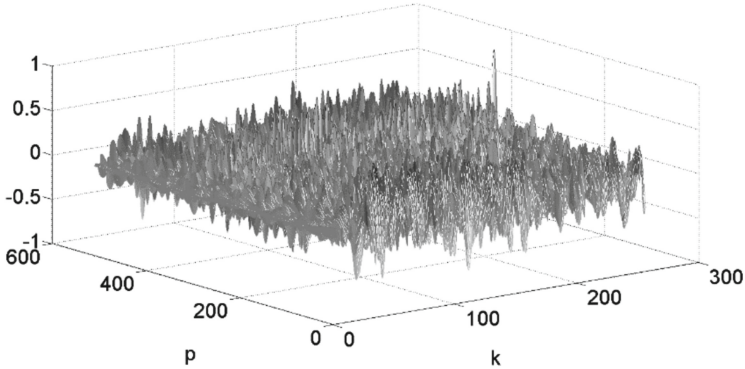


Fig. 3. A real component of $S(k, p)$ signal matrix signal complex matrix in isometric 3-D projection

The imaginary component of the $S(k, p)$ signal complex matrix in isometric 3-D projection is illustrated in Fig. 4.

The real component of the range compressed complex matrix $S(k, p)$ complex signal matrix in an isometric 3-D projection is depicted in Fig. 5.

The imaginary component of the range compressed complex signal matrix $S(k, p)$ in isometric 3-D projection is presented in Fig. 6. The real component of the azimuth compressed complex signal matrix $S(k, p)$ after range compression in isometric 3-D projection is depicted in Fig. 7.

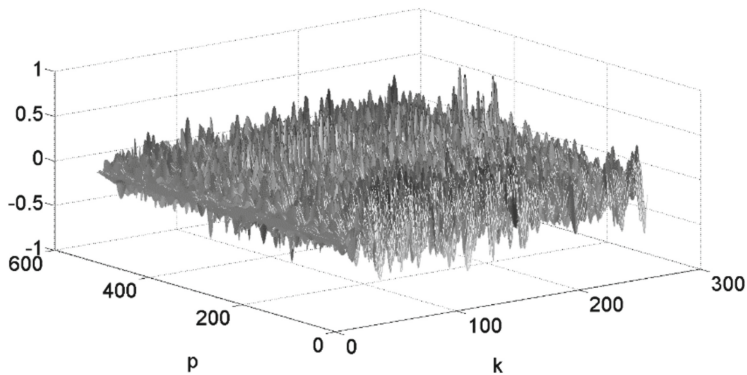


Fig. 4. An imaginary component of $S(k, p)$ complex signal matrix in an isometric 3-D projection

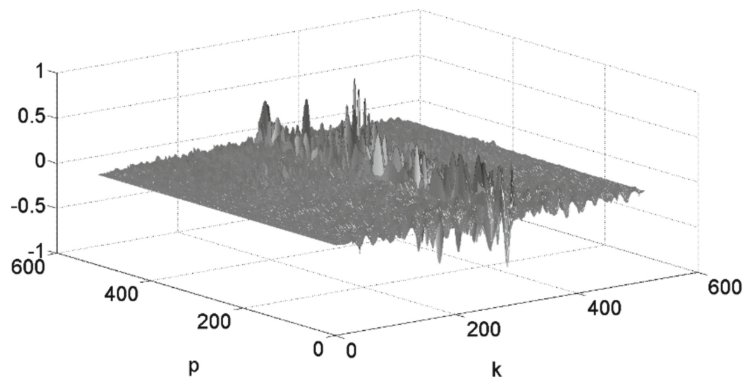


Fig. 5. The real component of the range compressed $S(k, p)$ complex signal matrix in an isometric 3-D projection

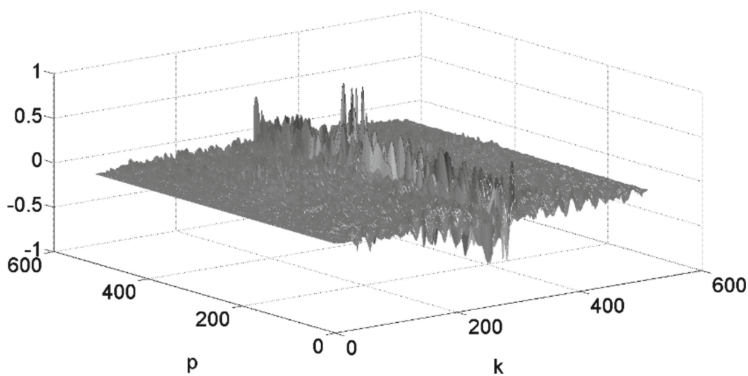


Fig. 6. The imaginary component of the range compressed $S(k, p)$ complex signal matrix in an isometric 3-D projection

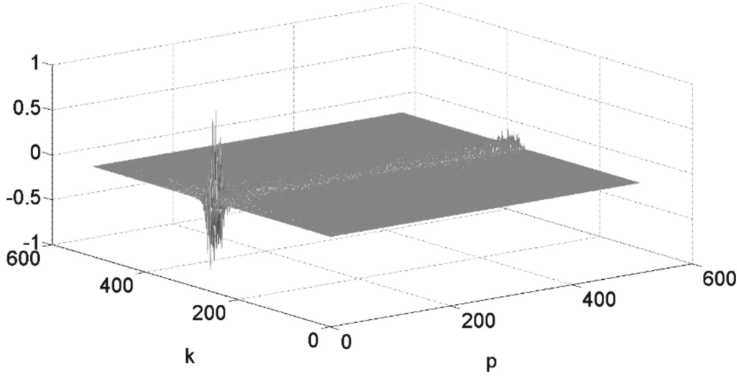


Fig. 7. The real component of azimuth compressed complex signal $S(k, p)$ matrix after range compression

The imaginary component of azimuth compressed complex signal matrix $S(k, p)$ after range compression in isometric 3-D projection is depicted in Fig. 8.

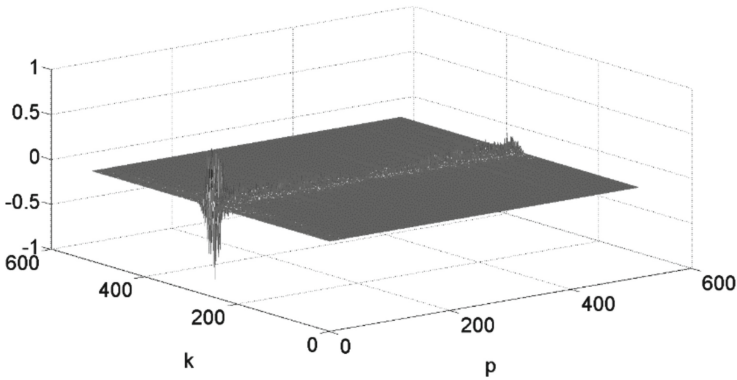


Fig. 8. The imaginary component of azimuth compressed $S(k, p)$ complex signal after range compression

The amplitude value of the final image is presented in Fig. 9. Having in mind that the range resolution is 1.5 m, the obtained BISAR image is satisfactory, the silhouette of the observed object and its scattering point are clearly seen.

The object's image is visualized in a small sized frame with coordinates $k = 0-50$, and $p = 240-300$, marked in Fig. 9. As the image is received by illumination with one symbol of low power, distances to the object is short, which is a serious tactical problem in detection and object imaging.

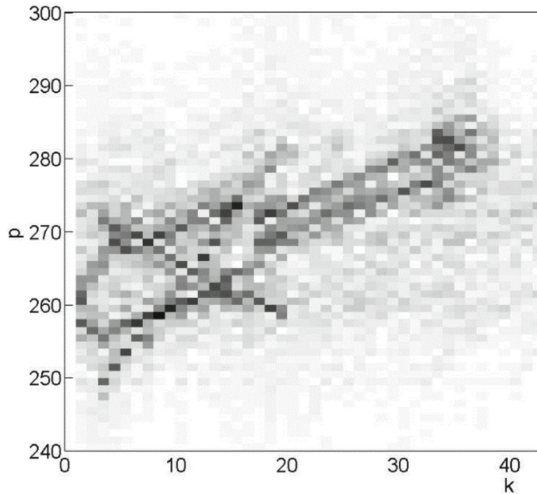


Fig. 9. The final reconstructed BISAR image

6 Conclusion

In the present work distance vector equations of BISAR geometry and kinematics are derived. 5G NR waveform's parameters are thoroughly described from point of view of the BISAR application. It is suggested to be used only one symbol with frequency bandwidth 99 MHz for bi-static inverse aperture synthesis. An image reconstruction algorithm is developed including range compression realized by cross correlation or inverse Fourier transform on range coordinates, and azimuth compression realized by inverse Fourier transform on azimuth coordinates. Results of simulation experiments are provided to verify the correctness of the developed models and imaging algorithm.

Acknowledgment. This study was funded by BNSF, grant number KP-06-N57/6, entitled “Theoretical and experimental research of models and algorithms for formation and control of specific relief textures on different types of functional surfaces”, and supported by NSP – Security and Defence adopted by Decision of the Council of Ministers No. 731, Oct. 21, 2021.

References

1. 211 NR; Physical channels and modulation (Release 15). https://www.sharetechnote.com/html/5G/5G_Waveform.html
2. Erik, D., Stefan, P., Johan, S.: Overview of 5G NR: the next generation wireless access technology, Academic Press, vol. 5, pp. 61–63, 2020
3. Liu, B., Lyu, X., Fan, W.: Analysis of 5G Signal for Radar Application. In: Journal of Physics Conference Series, vol. 2356, no. 1, p. 012027, October 2022. <https://doi.org/10.1088/1742-6596/2356/1/012027>
4. Romesh, S.B.: Executive summary of the thesis synthetic aperture radar imaging using 5G NR Signals, advisors: Stefano Tebaldini, Marco Manzoni, academic year 2022/23, Politecnico, Milano 1863. <https://www.politesi.polimi.it/handle/10589/215084>

5. Tan, B., Lohan, E.S., Sun, B., et al.: Improved sensing and positioning via 5G and mm wave radar for airport surveillance. https://www.sesarju.eu/sites/default/files/documents/sid/2021/papers/SIDs_2021_paper_4.pdf
6. Sun, B., Tan, B., Wang, W., et al.: 5G Positioning Based on the Wideband Electromagnetic Vector Antenna, 2021. <https://ceur-ws.org/Vol-2880/paper3.pdf>
7. Zhang, T., Zhang, X., Yang, Q.: Passive location for 5G OFDM radiation sources based on virtual synthetic aperture. *Remote Sens.* **15**, 1695 (2023). <https://doi.org/10.3390/rs15061695>
8. Abratkiewicz, K., Księżyk, A., Płotka, M., Samczyński, P., Wszolek, J., Zieliński, T.: SSB-based signal processing for passive radar using a 5G network. *IEEE J. Sel. Top. Appl. Earth Obs. Remote Sens.* **16**, 3469–3484 (2023). <https://doi.org/10.1109/JSTARS.2023.3262291>
9. Maksymiuk, R., Samczyński, P., Abratkiewicz, K.: Impact of uplink traffic on 5G-based passive radar. In: 2023 Signal Processing Symposium (SPSymo), pp. 117–122, 2023. <https://doi.org/10.23919/SPSymo57300.2023.10302721>
10. Samczyński, P., Abratkiewicz, K., Płotka, M., et al.: 5G network-based passive radar. *IEEE Trans. Geosci. Remote Sens.* **60**, 1–9 (2022). <https://doi.org/10.1109/TGRS.2021.3137904>
11. Bo, S., Bo, T., Wenbo, W., Mikko, V., Elena, S.L.: Embedding the radio imaging in 5G networks: signal processing and an airport use case. In: 2021 IEEE 94th Vehicular Technology Conference, VTC 2021-Fall – Proceedings, Institute of Electrical and Electronics Engineers Inc., ISBN (Electronic) 9781665413688



Radar Detection in the Presence of Impulse Interference

Ivan Garvanov^(✉) and Magdalena Garvanova

University of Library Studies and Information Technologies, Sofia, Bulgaria

{i.garvanov,m.garvanova}@unibit.bg

Abstract. The detection of moving targets by radar in the presence of impulse interference is highly difficult. There are many papers, in which different Constant False Alarm Rate (CFAR) detectors have been analyzed in the presence of randomly arriving impulse interference. In this research, the randomly arriving impulse interference is mathematically described as Poisson and Binomial pulse sequences. These models of impulse noise are used for numerical analysis of excision (EXC) CFAR and EXC CFAR BI (binary integration) detectors. The analytical expressions for detection probabilities and the average decision threshold (ADT) of EXC CFAR detector in the presence of Poisson and Binomial distributed impulse interference are obtained and compared in the paper. These results can be used in the design of real radar systems.

Keywords: radar signal processing · EXC CFAR processor · randomly arriving impulse interference · average decision threshold · detection probability

1 Introduction

The development of wireless technologies, including satellite and cellular communications, the Internet of Everything, and many other wireless communication systems leads to a continuous increase in electromagnetic interference (EMI) and radio-frequency interference (RFI) [1, 2]. The joint operation of many wireless sensors is a prerequisite for the appearance of electromagnetic interference, also called radio-frequency interference. These interferences can make wireless sensor devices difficult to operate or cause them to shut down. In practice, it is often necessary to operate a radar in a highly noisy environment in the presence of chaotic impulse interference [3].

Conventional Cell-Averaging Constant False Alarm Rate (CA CFAR) detectors are very effective in case of stationary and homogeneous interference. In such noisy environment, the problem of target detection is formulated as detection of a single pulse on the background of Gaussian noise. In a CA CFAR detector, proposed by Finn and Johnson, pulse detection is declared if the signal value exceeds the threshold, which is formed by averaging the samples of the reference window surrounding the test cell [4]. The effectiveness of CA CFAR pulse detectors is very sensitive to non-stationary and non-homogeneous background and extremely degrades in the presence of strong randomly arriving impulse interference in both, the test resolution cell and the reference

window [5]. In the papers [6, 7] different approaches have been proposed to improve the detectability of CFAR detectors operating in random impulse noise. One approach to combating impulse interference was proposed by Rohling [8], where the algorithm uses ordered statistics at the source of the interference level in the reference window of the CFAR detector. This algorithm (OS CFAR detector) is tested in an intensive multipath environment and its performance is evaluated in [9]. In the presence of non-uniform power interference conditions, Hansen and Sawyers propose to use CFAR algorithm with “Greatest-of” selection (GO CFAR) [10]. The assessment of the level of the noise of this algorithm is chosen to be a larger sum of the elements of the two halves of the reference window. In [11, 12], another CFAR detector using “Smallest-of” logic (SO CFAR) was investigated. The noise level estimate of this algorithm is chosen to be equal to the smaller sum of the elements of the two halves of the reference window. This algorithm was first proposed by Trunk [13] under the condition of closely spaced targets, but it is only effective in the case of asymmetric location of the targets about the test item. There are also various modifications of the OS algorithm [14, 15] using half of the reference window, namely OSSO and OSGO algorithms. They are a combination of the already discussed OS, GO, and SO. These algorithms are effective in conditions of non-uniform noise environment and presence of secondary targets or impulse interference in the reference window, the OSGO algorithm being better [14]. Another approach to improve the performance of CFAR detectors in the presence of impulse interference is to excise high-power samples from the reference window before processing by a conventional CFAR pulse detector. This approach was used by Goldman for design of an excision CFAR detector (EXC CFAR) described in [16]. This algorithm is more efficient than the SO CFAR algorithm, especially in cases where interference is present on both sides of the tested element. In the presence of secondary targets or impulse disturbances in the reference window, regardless of their location relative to the test cell, this algorithm is very efficient.

Detecting a package radar signals (impulses) in practice is carried out by means of parallel processing of several cells by azimuth. The detection of the radar target (package pulses), in the CFAR detectors is carried out by means of binary or non-coherent integration of signals [17].

Algorithms for the detection of radar signals with Binary Integration (BI) of an input signal [18–20] present two-stage and two-threshold procedure. In the first stage, adaptive detection is performed of single pulses with adaptation of the first threshold to the level of disturbance (CFAR pulse detection), at the second stage – accumulating the detected pulses and comparing with a constant threshold Single pulse detection is performed by means of one of the above discussed CFAR detector.

In this paper, an attempt to summarize all previous studies of the EXC CFAR detector in the presence of Binomial and Poisson impulse noise and a theoretical calculation of the EXC CFAR and EXC CFAR BI detectors in the conditions of random impulse interferences is made. This detector can be applied in active and passive radar systems using active transmitters or artificial and natural sources of electromagnetic signals.

It is organized as follows: Sect. 2 describes the proposed signal models. Section 3 focuses on the operating principle of the EXC CFAR detector. In Sect. 4, probability characteristics of EXC CFAR and EXC CFAR BI detectors in Poisson and Binominal

pulse interferences are analyzed. Section 5, average detection threshold of EXC CFAR detector in Poisson and Binominal pulse interferences is obtained. Section 6 discussed obtained results. Finally, we conclude our study in Sect. 7.

2 Signal Model

Let us assume that L pulses hit the target, which is modeled according to the Swerling case II. The received signal power is sampled in range by using $(N + 1)$ resolution cells resulting in a data matrix with $(N + 1)$ rows and L columns. Each row of the data matrix is of signal values obtained for L pulse repetition intervals in one range resolution cell. The sampling rate in range is such that the samples in each column are statistically independent. Let us also assume that the first “ $N/2$ ” and the last “ $N/2$ ” rows of the data matrix are used as reference cells to estimate the noise level in the test resolution cells of the data matrix. The test resolution cells are the “ $N/2 + 1$ ” row of the data matrix. The distribution law of samples in the data matrix depends on the impulse noise model [5].

2.1 Binomial Impulse Noise

The Binomial model describes a situation when the impulse noise is derived from two independent and identical impulse-noise sources, each of which generates a random impulse sequence with the same power intensity and the same average repetition frequency [21, 22]. The probability of occurrence (p) of a random pulse generated by each impulse-noise source in each range resolution cell can be expressed as $p = F \cdot t$, where F is the average pulse repetition frequency of and t is the transmitted pulse duration. This means that the elements of the reference window are drawn from three classes. The first class represents the receiver noise only with probability $(1 - p)^2$. The second class represents a situation when the signal samples are corrupted by a random impulse generated by one or the other impulse-noise source. This situation occurs with probability $2p(1 - p)$. The third class represents a situation when the signal samples are corrupted by a total random pulse that is a sum of pulses generated by the two impulse-noise sources. This situation occurs with probability p^2 . According to the theorem of total probability, the elements of the reference window are independent random variables distributed with the following probability density function (PDF):

$$f_B(x_i) = \frac{(1 - p)^2}{\eta} \exp\left(\frac{-x_i}{\eta}\right) + \frac{2p(1 - p)}{\eta(1 + I)} \exp\left(\frac{-x_i}{\eta(1 + I)}\right) + \frac{p^2}{\eta(1 + 2I)} \exp\left(\frac{-x_i}{\eta(1 + 2I)}\right), i = 1, \dots, N \quad (1)$$

where η is the average power of the receiver noise, I is the average per pulse interference-to-noise ratio (INR) at the receiver input, and N is the number of samples in the reference window.

In the presence of a wanted signal in the test resolution cell, the signal samples are independent random variables distributed with the following PDF:

$$f_{SB}(x_{0l}) = \frac{(1-p)^2}{\eta(1+S)} \exp\left(\frac{-x_{0l}}{\eta(1+S)}\right) + \frac{2p(1-p)}{\eta(1+I+S)} \exp\left(\frac{-x_{0l}}{\eta(1+I+S)}\right) + \frac{p^2}{\eta(1+2I+S)} \exp\left(\frac{-x_{0l}}{\eta(1+2I+S)}\right), l = 1, \dots, L \quad (2)$$

where S is the average per pulse signal-to-noise ratio (SNR). When the probability for appearance of impulse interference is small (to 0.1), then $p^2 \cong 0$ and the flow is Poisson distributed [5].

2.2 Poisson Impulse Noise

The Poisson model describes a real radar situation when the impulse noise arrivals from a single impulse-noise source [23, 24]. According to this model, in each range resolution cell the signal sample may be corrupted by impulse noise with constant probability p_0 . Therefore, the elements of the reference window are drawn from two classes. One class represents the interference-plus-noise with probability p_0 . The other class represents the receiver noise only with probability $(1 - p_0)$. According to the theorem of total probability, the elements of the reference window are independent random variables distributed with the following PDF:

$$f_P(x_i) = \frac{(1-p_0)}{\eta} \exp\left(\frac{-x_i}{\eta}\right) + \frac{p_0}{\eta(1+I)} \exp\left(\frac{-x_i}{\eta(1+I)}\right) \quad (3)$$

In the presence of a desired signal in the test resolution cell, the signal samples are independent random variables distributed with the following PDF:

$$f_{SP}(x_{0l}) = \frac{(1-p_0)}{\eta(1+S)} \exp\left(\frac{-x_{0l}}{\eta(1+S)}\right) + \frac{p_0}{\eta(1+I+S)} \exp\left(\frac{-x_{0l}}{\eta(1+I+S)}\right) \quad (4)$$

The probability of occurrence of a random pulse in each range resolution cell can be expressed as $p_0 = F \cdot t$, where F is the average frequency of pulse repetition and t is the transmitted pulse duration. It must be noted that if the probability p_0 is small $p_0 < 0.1$, the size of a reference window N is large, and $Np_0 = \text{const}$, then the model may be approximated with a Poisson model of impulse noise.

3 EXCISION CFAR Detector

In the presence of interfering objects or impulse interference in test cell and the reference window, the CA CFAR detector reduces its performance. To combat the interfering targets, Goldman in [16] proposed an algorithm using censoring (excision) of the cells in the reference window. Signals in cells of the reference window exceeding the censoring threshold are reset. This algorithm is effective in the presence of strong impulse interference in the radar cells. The block scheme of the censoring detector is shown in

Fig. 1. The values of the items of the reference window (x_1, x_2, \dots, x_N) are compared with a censoring threshold B_E . Elements with a greater power exceeding the censoring threshold are reset, and elements with a value less than the B_E threshold retain their magnitude:

$$y_i = \begin{cases} x_i, & \text{if } x_i \leq \text{threshold } B_E \\ 0, & \text{otherwise} \end{cases} \quad (5)$$

The remaining non-zero values after censoring are summed to form the detector noise level estimate:

$$V = 1/k \sum_{i=1}^k y_i \quad (6)$$

where k is the number of non-zero elements at the limiter output.

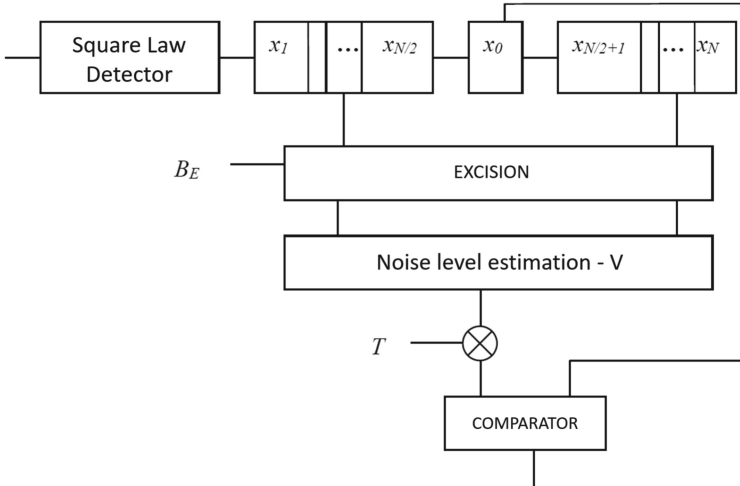


Fig. 1. Block diagram of EXC CFAR detector

The detector threshold H_D is obtained as the product of the noise level estimation V and a scalar factor T , keeping the false alarm probability constant:

$$H_D = VT \quad (7)$$

Detection of the signal reflected from the target in the EXC CFAR detector occurs after comparing the test element x_0 with the detection threshold (Fig. 2). The pulse detection is declared, if the test cell exceeds the pulse detection threshold H_D .

In L channel EXC CFAR BI detector, all samples $\{x_{0l}\}_L$ are compared with the threshold H_{Dl} according to the rule:

$$\Phi_l(x_l) = \begin{cases} 1, & \text{if } x_{0l} \geq H_{Dl} \\ 0, & \text{otherwise} \end{cases} \quad (8)$$

The binary integrator performs a sum of L decisions Φ_l . The target detection is declared if this sum exceeds the second threshold M :

$$\begin{cases} H_1 : (\text{target present}), \text{ if } \sum_{i=1}^L \Phi_i \geq M \\ H_0 : (\text{no target}), \text{ otherwise} \end{cases} \quad (9)$$

where H_1 is the hypothesis that the test resolution cell contains the echoes from the target and H_0 is the hypothesis that the test resolution cell contains the randomly arriving impulse interference only.

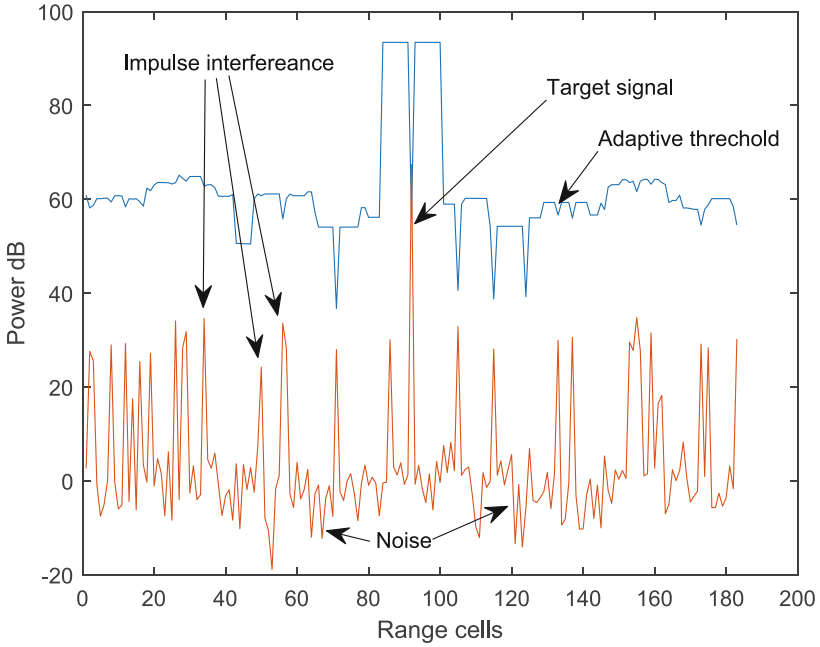


Fig. 2. A model of a radar signal containing: target signal, impulse interference and white Gaussian noise together with the EXC CFAR detector threshold

4 Probability Characteristics of EXC CFAR Detector

The probability density function of the random variable y_i in the presence of chaotic impulse interferences with Binomial distribution has the form:

$$f_B(y_i) = \frac{(1-p)^2 \exp\left(\frac{-y_i}{\eta}\right)}{\eta \left(1 - \exp\left(\frac{-B_E}{\eta}\right)\right)} + \frac{2p(1-p) \exp\left(\frac{-y_i}{\eta(1+I)}\right)}{\eta(1+I) \left(1 - \exp\left(\frac{-B_E}{\eta(1+I)}\right)\right)}$$

$$+ \frac{p^2 \exp\left(\frac{-y_i}{\eta(1+2I)}\right)}{\eta(1+2I)\left(1 - \exp\left(\frac{-B_E}{\eta(1+2I)}\right)\right)} \quad (10)$$

Detection probabilities and false alarm probability of EXC CFAR processor in the conditions of Binomial flow of impulse interferences are obtained in [19]. The probability that a given element x_i of the reference window remains at the output of the censoring device is:

$$P_E = 1 - (1-p)^2 \exp\left(\frac{-B_E}{\eta}\right) - 2p(1-p) \exp\left(\frac{-B_E}{\eta(1+I)}\right) - p^2 \exp\left(\frac{-B_E}{\eta(1+2I)}\right) \quad (11)$$

On the other hand, the probability that k out of N cells from the reference cells remain at the output of the censoring device is:

$$q(k) = C_N^k P_E^k (1 - P_E)^{N-k} \quad (12)$$

The moment generating function (MGF) of the random variable y_i at the output of the excising device may be obtained by means of the Laplace transform of the probability density function (10) and has the form:

$$M_y(U) = \frac{(1-p)^2(1 - \exp(R_{B1} - B_E U))}{(1 - \exp(R_{B1}))(1 + U\eta)} + \frac{2p(1-p)(1 - \exp(R_{B2} - B_E U))}{(1 - \exp(R_{B2}))(1 + U\eta(1+I))} + \frac{p^2(1 - \exp(R_{B3} - B_E U))}{(1 - \exp(R_{B3}))(1 + U\eta(1+2I))} \quad (13)$$

where

$$R_{B1} = \frac{-B_E}{\eta}, R_{B2} = \frac{-B_E}{\eta(1+I)}, R_{B3} = \frac{-B_E}{\eta(1+2I)} \quad (14)$$

Since the random variables x_i ($1 < i \leq k$) are independent, the MGF of the noise level estimate V can be expressed as:

$$M_V(U, k) = \left\{ \frac{(1-p)^2 \left(1 - \exp\left(R_{B1} - \frac{B_E U}{k}\right)\right)}{(1 - \exp(R_{B1})) \left(1 + \frac{U\eta}{k}\right)} \right\}^{k-i-j} \sum_{j=0}^{k-i} C_{k-i}^j \left\{ \frac{2p(1-p) \left(1 - \exp\left(R_{B2} - \frac{B_E U}{k}\right)\right)}{(1 - \exp(R_{B2})) \left(1 + \frac{U\eta(1+I)}{k}\right)} \right\}^j \sum_{i=0}^k C_k^i \left\{ \frac{p^2 \left(1 - \exp\left(R_{B3} - \frac{B_E U}{k}\right)\right)}{(1 - \exp(R_{B3})) \left(1 + \frac{U\eta(1+2I)}{k}\right)} \right\}^i \quad (15)$$

Given the probability that k cells from the reference window are not censored, for the MGF of the estimate V was obtained:

$$M_V(U) = \sum_{k=1}^N C_N^k P_E^k (1 - P_E)^{N-k} M_V(U, k) \quad (16)$$

In case of random Binominal impulse noise, the analytical expression for calculating the detection probability of an EXC CFAR pulse detector is obtained in [19]:

$$\begin{aligned} P_d^B = & (1-p)^2 M_V\left(\frac{T}{\eta(1+S)}\right) + 2p(1-p) M_V\left(\frac{T}{\eta(1+I+S)}\right) \\ & + p^2 M_V\left(\frac{T}{\eta(1+2I+S)}\right) \end{aligned} \quad (17)$$

Substituting (16) in (17) gives the detection probability of the EXC CFAR processor as:

$$\begin{aligned} P_d^B = & \sum_{k=1}^N C_N^k P_E^k (1 - P_E)^{N-k} \left\{ (1-p)^2 M_V\left(\frac{T}{\eta(1+S)}, k\right) \right. \\ & \left. + 2p(1-p) M_V\left(\frac{T}{\eta(1+I+S)}, k\right) + p^2 M_V\left(\frac{T}{\eta(1+2I+S)}, k\right) \right\} \end{aligned} \quad (18)$$

Substituting the signal-to-noise ratio equal to zero ($S = 0$) in (18) yields the false alarm probability of EXC CFAR detector:

$$\begin{aligned} P_{fa}^B = & \sum_{k=1}^N C_N^k P_E^k (1 - P_E)^{N-k} \left\{ (1-p)^2 M_V\left(\frac{T}{\eta}, k\right) \right. \\ & \left. + 2p(1-p) M_V\left(\frac{T}{\eta(1+I)}, k\right) + p^2 M_V\left(\frac{T}{\eta(1+2I)}, k\right) \right\} \end{aligned} \quad (19)$$

The scalar factor T of the EXC CFAR detector is determined by (19) so that $P_{fa}^B = \text{const.}$

The probability of target detection for EXC CFAR BI processor in presence of binominal distribution impulse interference is computed by the following expression:

$$P_D^{BI} = \sum_{l=M}^N C_L^l (P_d^B)^l (1 - P_d^B)^{L-l} \quad (20)$$

The probability P_d^B is probability of pulse detection of the EXC CFAR detector in presence of binominal distribution impulse interference. The probability of false alarm of EXC CFAR and EXC CFAR BI detectors are evaluated by (19) and (20) setting $S = 0$.

When the probability for appearance of impulse interference is small (to 0.1), then the flow is Poisson distributed and the probability characteristics of EXC CFAR processor are obtained as in [25]. The characteristics of research detectors for binominal distribution

impulse interference are more general and include the probability characteristics of these detectors in presence of Poisson distribution impulse interference. If in (19), we accept that $2I = 0$, $p^2 = 0$, $2p(1-p) \rightarrow p_0$ and $(1-p)^2 \rightarrow (1-p_0)$, we obtained the probability of detection P_d^P of EXC CFAR detector in presence of Poisson distribution impulse interference as in [25]:

$$P_d^P = \sum_{k=1}^N C_N^k P_E^k (1 - P_E)^{N-k} \left\{ (1 - p_0) M_V \left(\frac{T}{\eta(1+S)}, k \right) + p_0 M_V \left(\frac{T}{\eta(1+I+S)}, k \right) \right\} \quad (21)$$

where p_0 and $(1 - p_0)$ are probabilities for appearance and no appearance of randomly arriving impulse interference. The probability of false alarm of the EXC CFAR detector in Poisson distribution pulse interference is evaluated by (20) setting $S = 0$.

5 Average Decision Threshold

The average decision threshold (ADT) is defined as a normalized quantity [26]:

$$ADT_{CFAR} = E(TV)/\eta \quad (22)$$

where the random variable V is the result of the estimation method used in the CFAR system, T is the scaling factor for threshold adjustment adapted to the estimation method and required P_{FA} . E stands for the expectation:

$$E(V)/\eta = -\frac{d}{dT} M_V \left(\frac{T}{\eta} \right) \Big|_{T=0} \quad (23)$$

Deviating from the methods usually described in radar literature, are use the ADT for comparison of various CFAR processors. This provides the advantage that the difference, existing between various CFAR systems, is then expressed by a single-valued measure. The difference between two CFAR systems can be expressed by the ratio between the two ADT's measured in dB [26]:

$$\Delta[dB] = \frac{ADT_1}{ADT_2} = 10 \lg \frac{E(T_1 V_1)}{E(T_2 V_2)} \quad (24)$$

for $P_{fa_1} = P_{fa_2}$ and $P_{D_1} = P_{D_2} = 0.5$

5.1 Determination of the Average Decision Threshold of EXC CFAR Detector in Presence of Binomial Distributed Randomly Arriving Impulse Interference

The ADT of EXC CFAR pulse detector in presence of binomial distributed randomly arriving impulse interference is obtained from Eq. (23) and (16):

$$ADT^B = T \sum_{k=1}^N C_N^k P_E^k (1 - P_E)^{N-k} \sum_{i=0}^k C_k^i \left(\frac{p^2}{1 - \exp(R_3)} \right)^i.$$

$$\begin{aligned}
& \sum_{j=0}^{k-i} C_{k-i}^j \left(\frac{2p(1-p)}{1 - \exp(R_2)} \right)^j \left(\frac{(1-p)^2}{1 - \exp(R_1)} \right)^{k-i-j} \\
& \frac{1}{k} (1 - \exp(R_3))^i (1 - \exp(R_2))^j (1 - \exp(R_1))^{k-i-j} \\
& \left(i \left(\frac{B_E \exp(R_3)}{1 - \exp(R_3)} + (1 + 2I) \right) + j \left(\frac{B_E \exp(R_2)}{1 - \exp(R_2)} + (1 + I) \right) \right. \\
& \quad \left. + (k - i - j) \left(\frac{B_E \exp(R_1)}{1 - \exp(R_1)} + 1 \right) \right) \quad (25)
\end{aligned}$$

where T is computed by expression (18) for given probability of false alarm, setting $S = 0$. When the probability for appearance of pulse interference is small or the flow of distribution is Poisson, then the ADT of EXC CFAR processor is obtained in [26]. The new analytical equation for the ADT of research detector is more general and described binominal and Poisson distribution pulse interference. If in (24) replace $i = 0$ and accept that $2I = 0$, $p^2 = 0$, $2p(1-p) \rightarrow p_0$ and $(1-p)^2 \rightarrow (1-p_0)$, we obtained the ADT in Poisson distribution pulse interference as in [19]:

$$\begin{aligned}
ADT^P &= -T \sum_{k=1}^N C_N^k P_E^k (1 - P_E)^{N-k} \\
& \sum_{i=0}^k C_k^i \left(\frac{p_0}{1 - \exp(R_1)} \right)^i \left(\frac{(1-p_0)}{1 - \exp(R_2)} \right)^{k-i} \frac{(1 - \exp(R_1))^i}{(1 - \exp(R_2))^{i+1-k}} \\
& \left(\frac{i}{k} \left(\frac{B_E (\exp(R_1) - \exp(R_2))}{1 - \exp(R_1)} - I(1 - \exp(R_2)) \right) + \exp(R_2)(B_E + 1) - 1 \right) \quad (26)
\end{aligned}$$

where p_0 and $(1 - p_0)$ are probabilities for appearance and no appearance of randomly arriving impulse interference.

6 Results

The ADT of EXC CFAR processor in the conditions of Poisson flow of impulse interference is obtain by using expressions (20) and (21) for $P_d^P = 0.5$ and are shown in Fig. 3. The results were obtained with the following input parameters: $B_E = 2$, $N = 16$, $P_{fa}^P = 10^{-6}$, $\eta = 1$, $I = 30$ dB, $p_0 = 0 \div 0.1$.

The ADT of EXC CFAR processor in the conditions of Binominal flow of impulse interference is obtain by using expressions (25) and (18) for $P_d^B = 0.5$ and are shown in Fig. 4. The results were obtained with the following input parameters: $B_E = 2$, $N = 16$, $P_{fa}^B = 10^{-6}$, $\eta = 1$, $I = 30$ dB, $p = 0.1 \div 0.9$.

The presence of additional excision threshold processing leads to the reset of all impulse interferences in the reference window. Thus, the noise level estimation in the reference window is maintained constant regardless of the increase in the average power or the probability of appearance of impulse interferences. To maintain the false alarm constant as the impulse interference parameters change, the scalar factor increases. This also leads to an increase in the ADT.

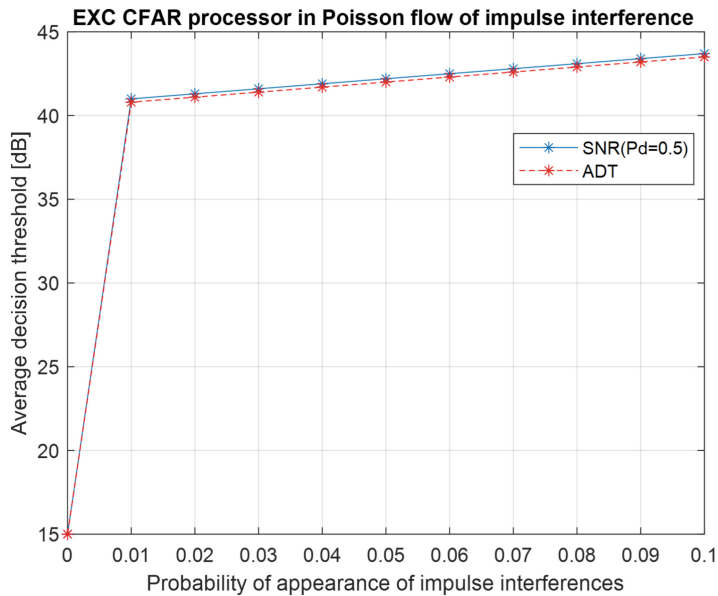


Fig. 3. The average decision threshold of EXC CFAR processor in the conditions of Poisson flow of impulse interference

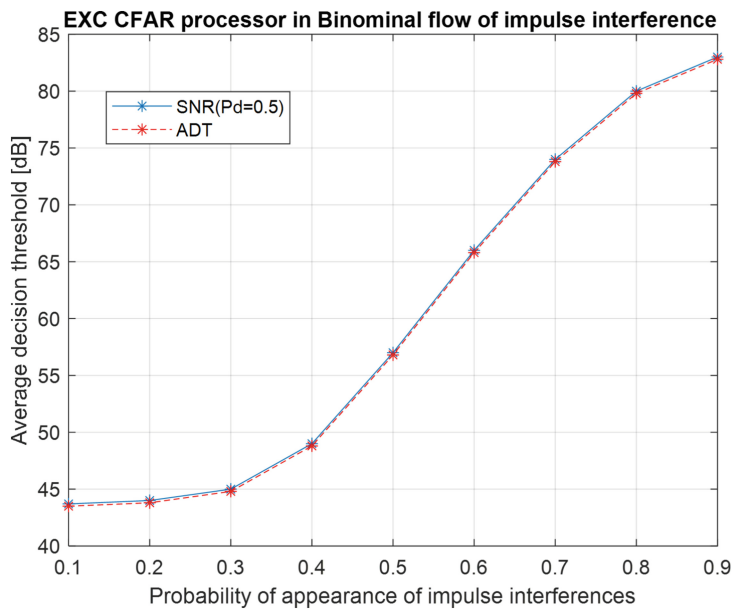


Fig. 4. The average decision threshold of EXC CFAR processor in the conditions of Binominal flow of impulse interference

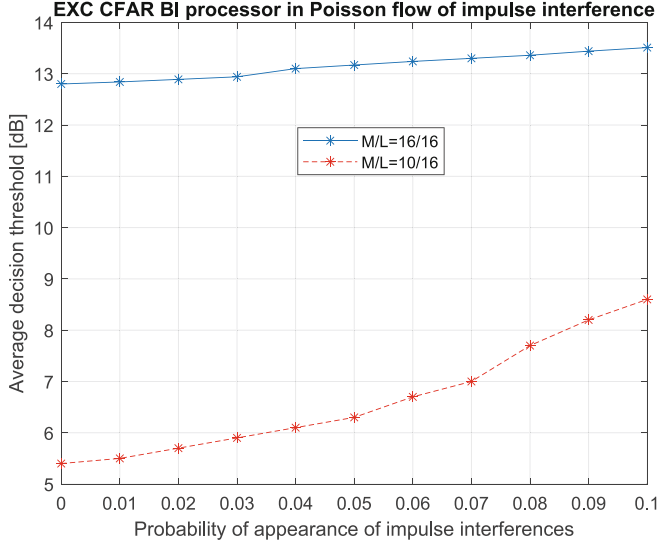


Fig. 5. The average decision threshold of EXC CFAR BI processor in the conditions of Poisson flow of impulse interference

The ADT of EXC CFAR BI processor in the conditions of Poisson flow of impulse interference is obtain by using expressions (20) where P_d^P is (21) and results are shown in Fig. 5. The results were obtained with the following input parameters: $B_E = 2$, $N = 16$, $P_{fa}^P = 10^{-6}$, $\eta = 1$, $I = 30$ dB, $p_0 = 0 \div 0.1$, $M/L = 10/16$ and $M/L = 16/16$.

The ADT of EXC CFAR BI processor in the conditions of Binominal flow of impulse interference is obtain by using expressions (20) where P_d^B is (18) and results are shown in Fig. 6. The results were obtained with the following input parameters: $B_E = 2$, $N = 16$, $P_{fa}^B = 10^{-6}$, $\eta = 1$, $I = 30$ dB, $p = 0.1 \div 0.9$, $M/L = 10/16$ and $M/L = 16/16$.

The results obtained indicate that the appropriate choice of binary threshold can improve the operation of the EXC CFAR BI detector.

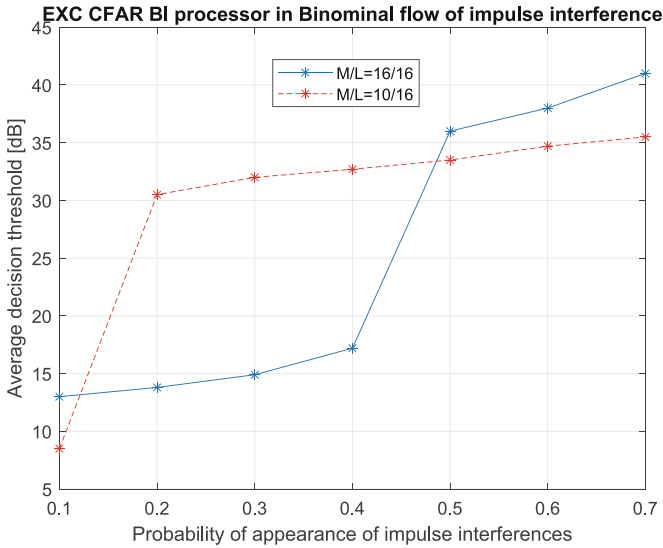


Fig. 6. The average decision threshold of EXC CFAR BI processor in the conditions of Binominal flow of impulse interference

7 Conclusions

In this paper, mathematical equations for estimation of the probability of detection and probability of false alarm of EXC CFAR BI detector in the presence of flow from randomly arriving impulses interference with binomial distribution are suggested. The probability characteristics of the EXC CFAR BI detector are obtained as a result of probability characteristics of the EXC CFAR detector. Therefore, we obtained the probability of detection and the probability of false alarm of one channel EXC CFAR detector in Binominal and Poisson distribution flow from impulse interference as well. The ADT of EXC CFAR detector is also obtained. The analytical results of the research EXC CFAR detector for Binominal distribution impulse interference are more general and include the probability characteristics and average decision threshold of this detector in presence of Poisson distribution impulse interference.

Acknowledgement. This work is supported by the Bulgarian National Science Fund, Project title “Innovative Methods and Algorithms for Detection and Recognition of Moving Objects by Integration of Heterogeneous Data”, KP-06-N 72/4/05.12.2023.

References

1. Natsuaki, R., Prats-Iraola, P.: Radio frequency interference detection for multi-receiver synthetic aperture radar based on interferometric analysis of raw data. In: 2020 International Symposium on Antennas and Propagation (ISAP), Osaka, Japan, pp. 349–350 (2021). <https://doi.org/10.23919/ISAP47053.2021.9391413>

2. Shishkov, B., Garvanova, G.: A review of pilotless vehicles. In: Shishkov, B., Lazarov, A. (eds.) *Telecommunications and Remote Sensing. ICTRS 2023. Communications in Computer and Information Science*, vol. 1990. Springer, Cham (2023). https://doi.org/10.1007/978-3-031-49263-1_11
3. Garvanov, I., Kabakchiev, C.: Sensitivity of CFAR processors towards the change of input distribution of pulse jamming. In: *Proceedings of the International Conference on Radar, RADAR 2003, Adelaide, Australia*, pp. 121–126 (2003). <https://doi.org/10.1109/RADAR.2003.1278722>
4. Finn, H.M., Johnson, R.S.: Adaptive detection mode with threshold control as a function of spatially sampled clutter estimation. *RCA Rev.* **29**(3), 414–464 (1968)
5. Garvanov, I.: Probability characteristics of CFAR processors in presence of randomly arriving impulse interference. In: Shishkov, B., Lazarov, A. (eds.) *Telecommunications and Remote Sensing. ICTRS 2023. Communications in Computer and Information Science*, vol. 1990. Springer, Cham (2023). https://doi.org/10.1007/978-3-031-49263-1_2
6. Garvanov, I., Kabakchiev, C.: Radar detection and track determination with a transform analogous to the hough transform. In: *Proceedings of International Radar Symposium – IRS 2006, Krakow, Poland, 24–26 May 2006*, pp. 121–124 (2006). <https://doi.org/10.1109/IRS.2006.4338015>
7. Garvanov, I., Behar, V., Kabakchiev, C.: CFAR processors in pulse jamming. In: Dimov, I., Lirkov, I., Margenov, S., Zlatev, Z. (eds.) *Numerical Methods and Applications. NMA 2002. Lecture Notes in Computer Science*, vol. 2542. Springer, Heidelberg (2003). https://doi.org/10.1007/3-540-36487-0_32
8. Rohling, H.: Radar CFAR thresholding in clutter and multiple target situations. *IEEE Trans. AES*-**19**(4), 608–621 (1983)
9. Rohling, H.: 25 years Research in Range CFAR Techniques. In: *Proceedings of the IRS-2003, Germany*, pp. 363–368 (2003)
10. Hansen, V., Sawyers, J.: Delectability loss due to “greatest of” selection in a cell – averaging CFAR. *IEEE Trans. AES*-**16**(1), 115–118 (1980)
11. Gandhi, P., Kassam, S.: Analysis of CFAR processors in nonhomogeneous background. *IEEE Trans. AES*-**24**(4), 427–444 (1988)
12. Weiss, M.: Analysis of some modified cell – averaging CFAR processors in multiple target situation. *IEEE Trans. AES*-**18**(1), 102–114 (1982)
13. Trunk, G.: Radar resolution of targets using automatic detection. *IEEE Trans. AES*-**14**(5), 750–755 (1978)
14. Elias-Fuste R., Garsia, M., Elias, M., Davo, R.: Analysis of some modified ordered statistic CFAR: OSGO and OSSO CFAR. *IEEE Trans. AES*-**26**(1), 197–202 (1990)
15. Wilson, S.: Two CFAR algorithms for interfering targets and nonhomogeneous clutter. *IEEE Trans. AES*-**29**(1), 57–72 (1993)
16. Goldman, H.: Performance of the excision CFAR detector in the presence of interferers. *IEE Proc.* **137**(3), 163–171 (1990)
17. Himonas, S., Barkat, M.: Automatic censored CFAR detection for nonhomogeneous environments. *IEEE Trans. AES*-**28**(1), 286–304 (1992)
18. Garvanov, I.: CFAR BI detector in binomial distribution pulse jamming. *Comptes Rendus l’Acad. Bulgare Sci.* **56**(10), 37–44 (2003)
19. Garvanov I., Kabakchiev, C.: Excision CFAR BI detector in randomly arriving impulse interference. In: *International Radar Conference, RADAR 2005, Crystal Gateway Marriott Arlington, USA, 9–12 May 2005*, pp. 950–955 (2005). <https://doi.org/10.1109/RADAR.2005.1435964>
20. Garvanov, I.: EXC CFAR BI processor with polar hough transform in the presence of binominal impulse interference. In: *Proceedings of the Signal Processing Symposium – SPS-2013, 5–7 June 2013, Jachranka, Poland* (2013). <https://doi.org/10.1109/SPS.2013.6623594>

21. Garvanov, I.: CFAR PI detector in the presence of binomial distribution flow from randomly arriving impulse interference. *Compt. Rend. Acad. Bulg. Sci.* **58**(5), 545–552 (2005)
22. Kabakchiev, C., Kyovtorov, V., Garvanov, I.: OS CFAR detector for pn signal processing in multipath interference. In: *Proceedings of IEEE – International Radar Conference “Radar 2004”*, Toulouse, France, CD-6P-SP-121, 6p. (2004)
23. Behar, V.: CA CFAR radar signal detection in pulse jamming. *Compt. Rend. Acad. Bulg. Sci.* **49**(12), 57–60 (1996)
24. Himonas, S.: CFAR integration processors in randomly arriving impulse interference. *IEEE Trans. Aerosp. Electron. Syst.* **30**(3), 809–817 (1994). <https://doi.org/10.1109/7.303750>
25. Behar, V., Kabakchiev, C.: Excision CFAR binary integration processors. *Compt. Rend. Acad. Bulg. Sci.* **49**(11/12), 45–48 (1996)
26. Garvanov I., Kabakchiev, C.: Average decision threshold of CA CFAR and excision CFAR detectors in the presence of strong pulse jamming. In: *Proceedings of the GRS 2002*, pp. 615–620 (2002)



Ionospheric Response to the Most Powerful Storm of Solar Cycle 25 in May 2024

Olga A. Maltseva^(✉) and Tatyana V. Nikitenko

Institute for Physics, Southern Federal University, Rostov-on-Don 344090, Russia
oamaltseva@sfedu.ru

Abstract. The powerful magnetic storm (MS) in May 2024, which occurred almost 20 years after a series of similar events in the early 21st century, has attracted great interest and a number of publications. The objective of the study in this paper was to examine what the powerful magnetic storm revealed in answering the questions: (1) are the ionosonde measurements correct, (2) are the foF2 and TEC parameters interchangeable, (3) does the empirical IRI-Plas model correspond to the experimental data, (4) are there any features in the behavior of the ionospheric parameters in the two hemispheres? The results of using the data from 10 ionosondes and 33 GPS receiver points along the 15° E meridian showed: (1) at many stations there were no measurements from the beginning of the main phase of the MS until the middle of the recovery phase; at those stations where measurements were available, low foF2 and hmF2 values were observed (foF2~2 MHz, hmF2 < 200 km). (2) A very high correlation was observed between the foF2 and TEC parameters both for the entire sufficiently disturbed month in general (0.84–0.9) and during the disturbance period (0.84–0.93 except for the Athens station with 0.715). (3) For the foF2 and TEC parameters, the most accurate was the IRI-Plas model adapted to the experimental TEC values, with average values of MAE(foF2) = 0.77 MHz, RMSE(foF2) = 1.01 km, MAPE(foF2) = 13.88%, MAE(TEC) = 1.42 TECU, RMSE(TEC) = 1.85 TECU, MAPE = 6.95%. For hmF2, the closest to the experimental data were the medians with average values of MAE = 30.13 km, RMSE = 49.27 km, MAPE = 15.1%. (4) A large asymmetry in the response of the ionosphere of the two hemispheres to the MS was observed: in the southern hemisphere, an extremely large positive disturbance was observed in the period close to the minimum of Dst (δ TEC up to ~500%), while in the northern hemisphere, from the very beginning of the MS, there was a negative main phase, which turned into a two-stage negative recovery phase.

Keywords: May 2024 storm · Ionosphere · Vertical Sounding · IRI-Plas Model · Total Electron Content

1 Introduction

As noted in [1], the Space Weather community has been waiting for an event like the 2024 May storm for two decades. The disturbance affected an incredibly large area of the globe. The first results related to the behavior of the ionosphere in local regions: in

[1] this is the Mediterranean sector, in [2] - the Mexican zone with the observation of an aurora in this zone. The paper [3] gives a comprehensive description of the details of the development of this multi-stage disturbance, the duration of the main phase of which is estimated at ~ 9 h, the duration of the recovery phase – at ~ 2.8 days, the observation of auroras across Europe, Asia and America at low geomagnetic latitudes down to $\sim 27.6^\circ$ (Puerto Rico) is noted, as well as the strengthening of the crests of the equatorial anomaly at the beginning of the main phase and confirmation of the existence of a clear anomaly structure with two ionization crests and a trough at $\sim 850\text{--}870$ km using DMSP satellites. The paper [4] presents a map of the reported auroral visibility from 10 May 2024 to 12 May 2024. It is seen that the main cases are related to the region of the southern part of North America up to 30° N. The paper [5] is devoted to a detailed analysis of the response of the equatorial and low-latitude ionosphere in the American-Atlantic longitude sector. The main attention is paid to the equatorial ionization anomaly (EIA). It is shown that the morphology and intensity of EIA crests are subject to the combined effect of electric field perturbations, modified neutral winds, and variations in thermospheric composition. In the paper [6], remarkable effects on composition, temperature, and dynamics in the Earth's thermosphere are studied by means of GOLD observations.

This paper presents the ionospheric response to this disturbance near the 15° N meridian based on ionospheric station data and global UPC GIM maps. Additionally, the performance of the IRI-Plas model under extremely strong disturbance conditions is investigated, including the features of the TEC response in different parts of the N(h) profile (bottomside ECbot, topside ECTop, plasmaspheric ECPI) when adapting the model to experimental values of the total electron content TEC(obs).

2 Experimental Data and Model

On the DIDBase website (<https://giro.uml.edu/ionoweb/>) for the northern hemisphere along a given meridian, data were available for the following stations: Tromsø (69.7° N, 19° E), Juliusruh (54.6° N, 13.4° E), Pruhonice (50° N, 14.6° E), Sopron (37.7° N, 16.6° E), Roquetes (40.8° N, 0.5° E), San Vito (40.6° N, 16.7° E), Gibilmanna (37.9° N, 14.1° E). For the stations Warsaw (52.2° N, 21.1° E), Hermanus (34.4° S, 19.2° E) the data were insufficient for statistics or completely absent. For statistics, the data from the Athens (38.4° N, 23.6° E) and El-Arenosillo (37.1° N, 6.7° S) stations were used. For the southern hemisphere, the data from the Ascension island station (7.9° S, 14.4° S) were taken to take into account possible differences from the behavior of the parameters in the northern hemisphere. The TEC values were calculated based on the IONEX data of the UPC map files for the European-African meridian of 15° E in the latitude range from 80° N to 80° S with a step of 5° in latitude and 2 h in time (<ftp://cddis.gsfc.nasa.gov/pub/gps/products/ionex/>). The values of the geomagnetic activity indices IMF, Bz, Np, Vsw, Kp, Dst, ap were taken from the OMNI website (<http://omniweb.gsfc.nasa.gov/form/dx1.html>).

The values of the parameters foF2, hmF2, TEC according to the IRI-Plas model were calculated online on the website (<http://www.ionolab.org/index.php?language=en>), the model was adapted using the experimental values of TEC(obs). The conformity of the experimental and model values was assessed using the metrics the mean absolute error

MAE, the root-mean-square error RMSE, the mean absolute percentage error MAPE for the period May 9–12, 2024. The behavior of the geomagnetic activity indices on these specific days is shown in Fig. 1.

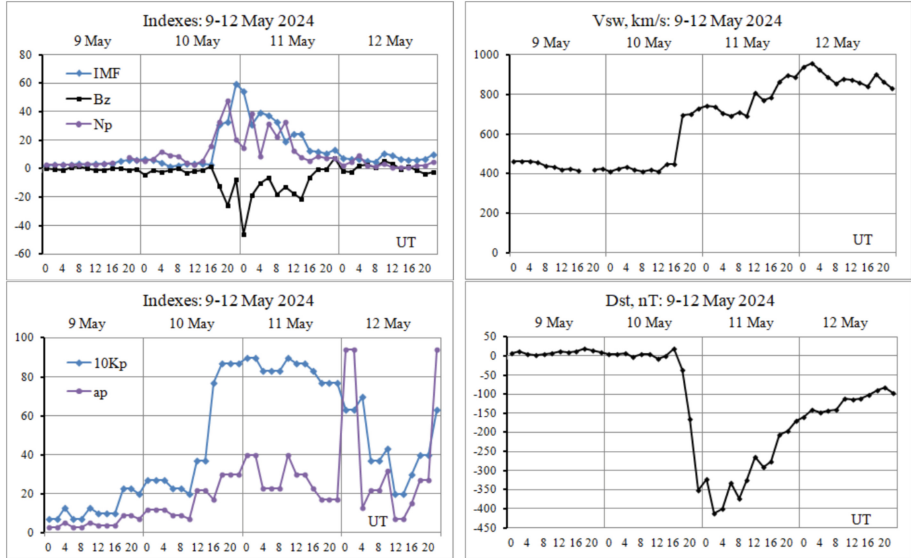


Fig. 1. Behavior of geomagnetic activity indices during the period May 9–12, 2024

It is evident that on May 9 the conditions were close to quiet, the magnetic storm began on May 10 with a jump in the solar wind speed V_{sw} from 449 km/s in UT16 to 697 km/s in UT18. Almost immediately in UT20 the southern component B_z reached the first minimum of -25.9 nT, the proton density reached a maximum of 48.1 cm^{-3} . In UT22 the interplanetary magnetic field IMF reached a maximum of 59.5 nT. On May 11 in UT00 B_z reached the second minimum of -46.5 nT, in UT02 the Dst index reached a minimum of -412 nT and initiated the recovery phase.

Examples of the behavior of the analyzed parameters are given in Fig. 2 for the high-latitude station Tromso and the mid-latitude station Juliusruh in the following order: for foF2, hmF2, TEC, contributions of different parts of the $N(h)$ -profile to TEC (bottomside ECbot, topside ECTop, plasmaspheric ECPI) in absolute value and in % relative to the full value of TEC, correlation coefficients of these contributions with geomagnetic activity indices.

Regarding the contributions of various parts of the $N(h)$ profile to the TEC, it can be noted that the calculation of these contributions is provided only in the IRI-Plas model and has not been sufficiently studied. In this case, it was interesting to see how various parts of the ionosphere react to an extremely strong disturbance. For this purpose, the correlation coefficients of these contributions with geomagnetic activity indices were additionally calculated.

The behavior of the vertical sounding parameters (foF2, hmF2) shows certain differences between the graphs for Tromso and Juliusruh. In addition to the differences in

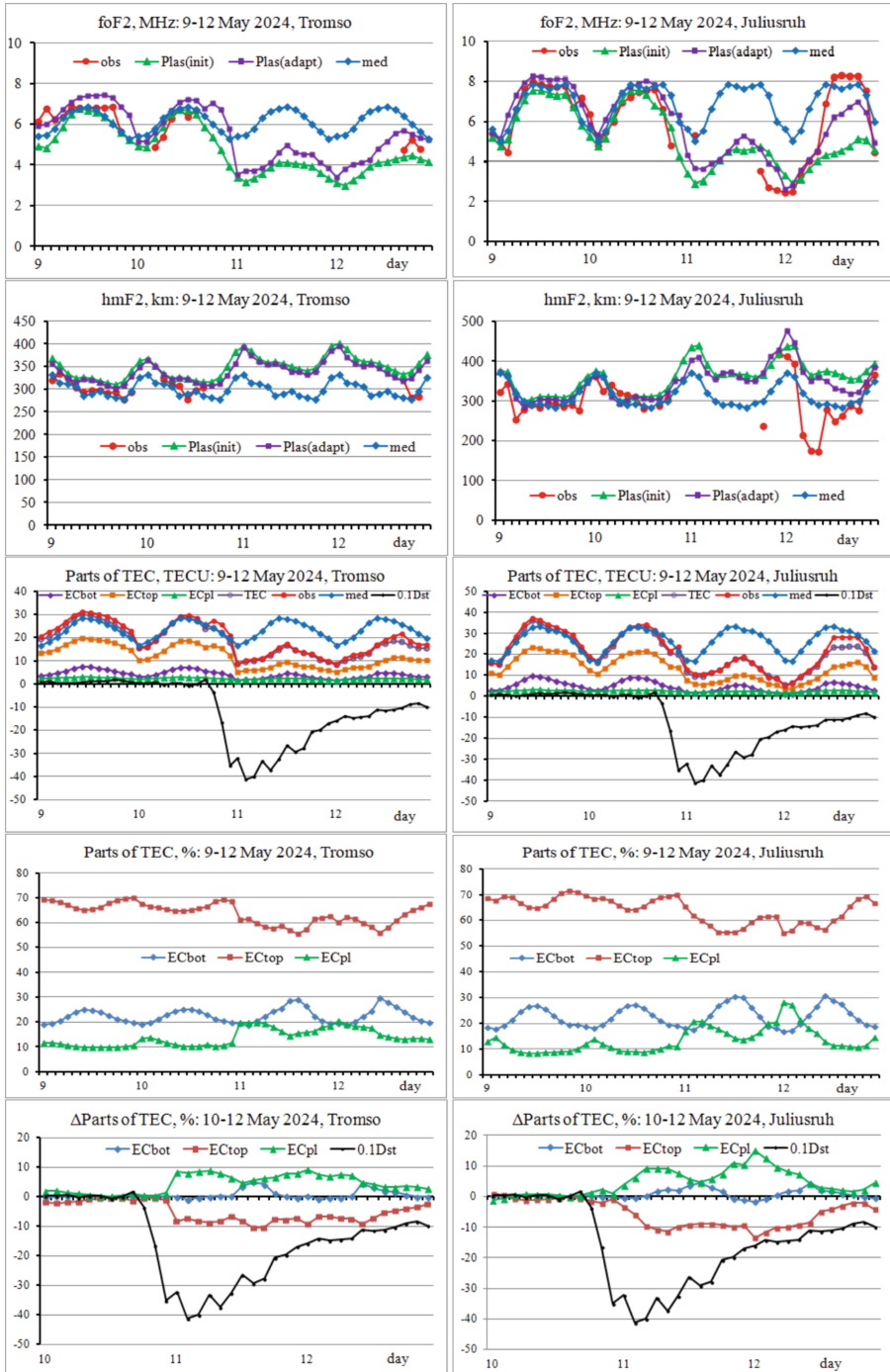


Fig. 2. Examples of the behavior of ionospheric parameters in the period from May 9 to 12 in the northern hemisphere

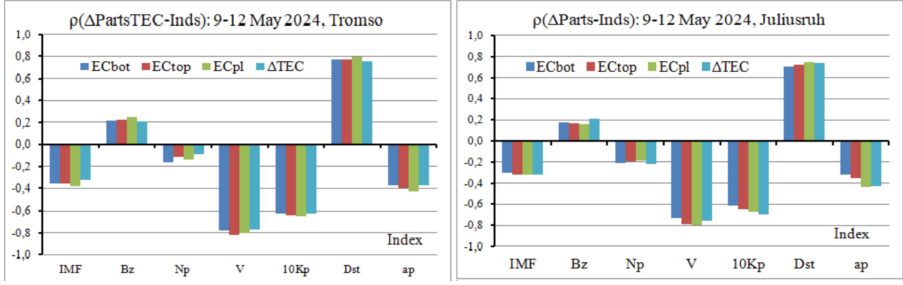


Fig. 2. (continued)

the values themselves, which correspond to the typical latitudinal dependence, it is clear that the magnetic storm had a stronger effect on the high-latitude Tromsø station, which led to the absence of values during the recovery phase on May 11–12, possibly due to the fall of foF2 below the minimum frequency f_{\min} of the ionosonde. The behavior of the parameters for the Juliusruh station shows that during the recovery phase on May 11 there was a strong negative disturbance, which, however, quickly returned to a quiet state on May 12. A distinctive feature is the unusually low values of foF2 and hmF2 (foF2 ~ 2 MHz, hmF2 < 200 km). As for the correspondence between the model and experimental values (a quantitative assessment is given in Tables 1 and 2), it is clear that for the initial (symbol init) and adapted (symbol adapt) models the values are quite close to each other and to the experimental values under quiet conditions, but differ under disturbed ones, and based on the results of these two stations it can be said that the parameters of the adapted model better reflect the nature of the variations during a disturbance.

The third panels show the variations of different parts of the TEC during the disturbance together with the Dst index, the values of which are reduced by a factor of 10. The values for the period of May 10–12 can be compared with the parameters on May 9, which are close to the values for quiet conditions. The percentage of different parts is shown in the fourth panel. It is seen that in quiet conditions the topside part makes the largest contribution and it is from 65% to 70%. The bottomside lies in the range from 20% to 25%, the plasmaspheric part is close to 10%.

The change of these parts during the disturbance period is shown in the fifth panel. It is evident that the behavior of all parameters does not differ much at these two stations and consists in the fact that: (1) the strongest negative disturbance begins during the main phase and is negative on May 11–12, (2) the values of the adapted TEC model (TEC icon on the panels) are very close to the experimental values, which allows reliable detection of TEC contributions, (3) during the disturbance, the contributions of various parts change significantly: the disturbance leads to a decrease in the topside part ECtop and an increase in the plasmaspheric part ECpl.

The value of the correlation coefficients, especially for ΔTEC , with the indices is important for forecasting the TEC parameter, i.e. the overall state of the ionosphere, for example, [7] using neural network methods. In this case, the most significant indices are Dst, Vsw, Kp, which leads to a three-component linear model, but it is clear that

one Dst index, most often used in forecasts, may be sufficient, since these indices are interconnected. Figure 3 shows an example of the behavior of the ionospheric parameters in comparison for stations in the northern and southern hemispheres - for the lowest-latitude El-Arenosillo station in the northern hemisphere and the Ascension island station in the southern hemisphere, both of which are located in the western hemisphere. The results are presented in the same order as in Fig. 2.

These two stations show their differences. For El-Arenosillo, the variation pattern corresponds to the northern hemisphere, but with more data, allowing us to note that the strongest negative disturbance of foF2 occurred in the main phase of the MS; a sharp increase in the hmF2 height was revealed at the beginning of the main phase and its maximum at the moment of the greatest negative Dst value. It is evident that the adapted model reflects foF2 variations quite well, but is unable to describe hmF2 variations. In the equatorial zone of the southern hemisphere, at Ascension island, foF2 variations are not as significant as in the northern hemisphere, except for a burst in foF2 at the beginning of the MS and a strong increase in hmF2 at the beginning of the recovery phase, although not as strong as at El-Arenosillo.

As for the agreement between the model and experimental values, it for foF2 is the best for the adapted model, the hmF2 values for both models are close to the median and do not reflect the disturbed burst. It is interesting to note that this burst is also observed at the southern hemisphere station. Differences between the two stations are also observed in the behavior of parts of TEC: for the Ascension station on May 12, TEC not only does not return to the quiet state, but also exceeds the median, indicating a small positive disturbance in the third panel. In the fourth panel, parts of TEC differ, where for the Ascension station, the ECpl contribution at night exceeds the topside ECTop contribution not only during disturbances, but also in quiet conditions, and in the fifth panel it is clear that during disturbances the change in contributions is not large. A more significant difference is seen for the correlation coefficients, where in the southern hemisphere these coefficients are not significant, indicating only some trends and the role of other factors.

3 Results

The results, examples of which are given in Figs. 2 and 3, were obtained for the remaining stations of vertical sounding VS (parameters foF2, hmF2, TEC) and for the TEC points along the meridian of 15° E. The results for the VS are given in Sect. 3.1 in the form of tables of metrics, the results for the meridian in Sect. 3.2 illustrate the latitudinal dependence of the TEC behavior. In Sect. 3.3, the influence of the magnetic storm on the behavior of the TEC components is given: bottomside, topside, plasmaspheric part.

3.1 Magnetic Storm Influence on Vertical Sounding Parameters

This influence is important both from the point of view of parameter changes and for their evaluation to determine the accuracy of the IRI-Plas model. In total, data were available for 10 stations and the results for other stations except those for which the results are shown in Figs. 2 and 3 are similar to the results of Figs. 2 and 3, i.e. the parameter values

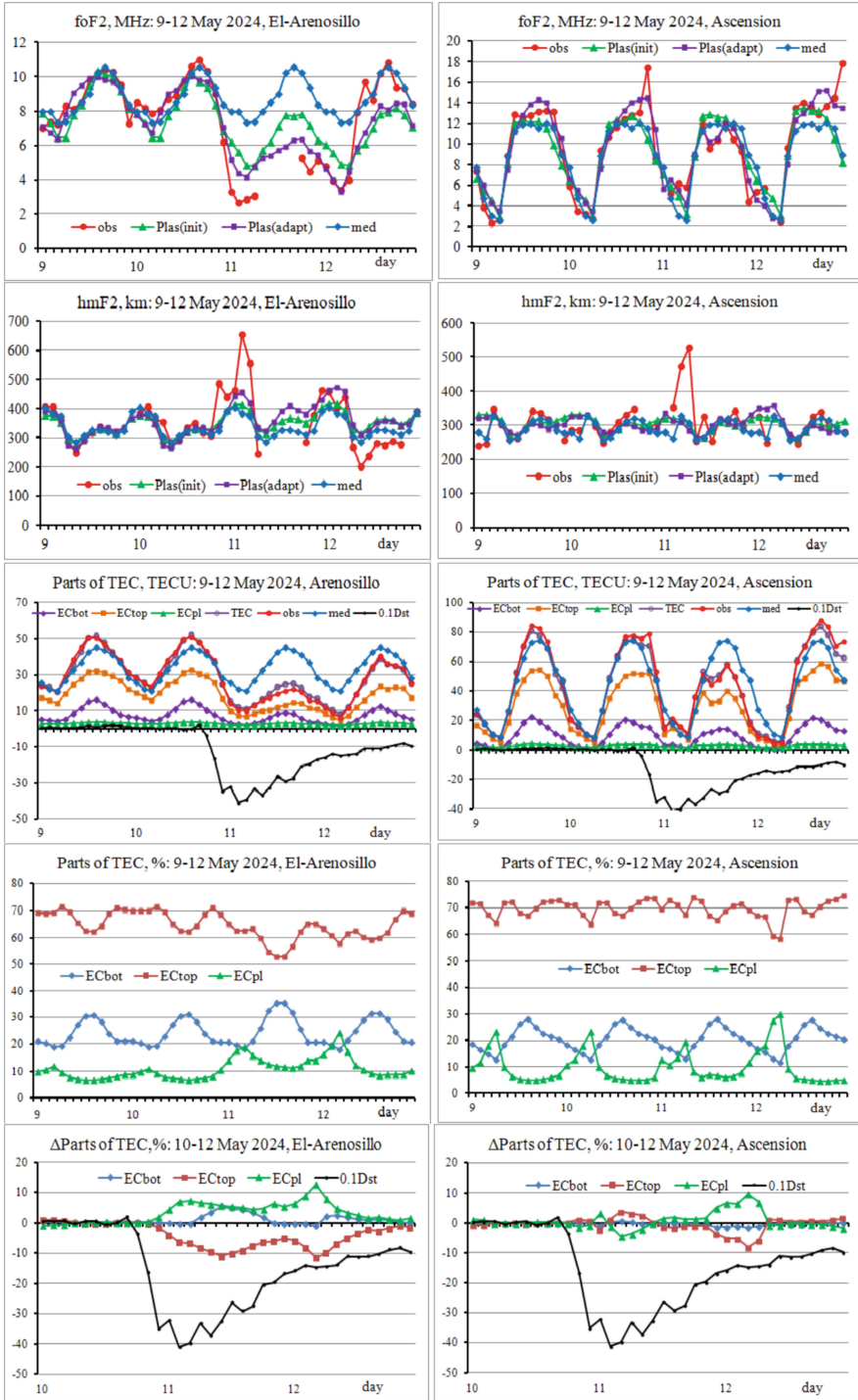


Fig. 3. Comparison of the behavior of ionospheric parameters in the period from May 9 to 12 in the northern and southern hemispheres

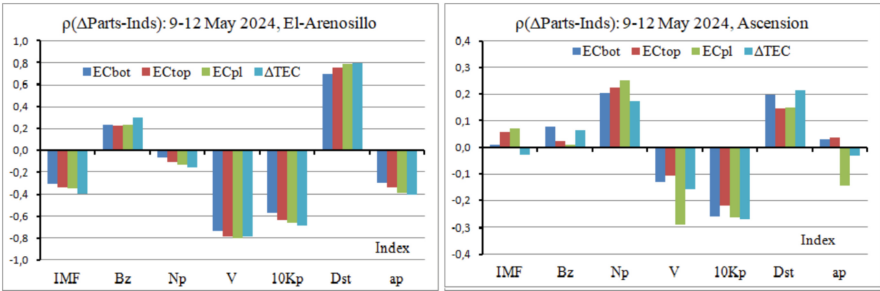


Fig. 3. (continued)

reach their extreme values near the critical moments on May 11 during the period of negative disturbance (UT ~ 2 and UT ~ 20–22). As can be seen from Figs. 2 and 3, the data had large gaps during this period, mainly from UT0 to UT16. For some stations (San Vito, Roquetes) this was the period from UT6 to UT16 and for the El-Arenosillo station from UT8 to UT14. The largest extreme values took place in the region of UT ~0–2 (the end of the main phase of the MS with the maximum negative value of Dst) and were 2.2–2.7 MHz for foF2 except for Ascension island (5.575 MHz) and for hmF2 from 585 km to 654 km. The second burst of extreme values took place in UT ~20–22 after the third negative burst of the Bz component during the recovery phase and was 2.5–4.5 MHz and 366–396 km. Quantitative estimates of the model accuracy are given in Tables 1, 2 and 3 for the parameters foF2, hmF2, TEC.

Table 1. Statistics of correspondence between model foF2 values and experimental data.

foF2	MAE, MHz			RMSE, MHz			MAPE, %		
	Plas	Plas		Plas	Plas		Plas	Plas	
station	init	adapt	med	init	adapt	med	init	adapt	med
Tromso	0.50	0.55	0.51	0.67	0.61	0.69	10.93	9.91	11.25
Juliusru	0.97	0.73	1.07	1.46	0.92	1.64	24.10	15.27	27.16
Dourbes	1.04	0.64	1.00	1.43	0.88	1.70	21.60	13.24	25.62
Pruhoni	1.04	0.62	1.12	1.48	0.96	1.82	22.26	14.42	27.27
Sopron	1.65	0.92	1.26	2.00	1.21	2.01	29.32	17.78	29.48
Roquet	1.17	0.62	1.17	1.42	0.86	1.80	19.00	11.55	24.09
SanVito	1.42	0.76	1.28	1.69	1.10	1.86	22.41	14.57	24.70
Athens	1.26	0.74	1.08	1.56	0.99	1.47	19.33	12.26	18.21
Arenosi	1.26	0.87	1.43	1.54	1.11	2.24	20.21	14.49	29.27
Ascens	1.43	1.20	1.50	2.27	1.46	2.21	23.69	15.30	23.10
mean	1.17	0.77	1.14	1.55	1.01	1.74	21.29	13.88	24.01

Each table indicates the parameter and gives the name of the stations (the stations are arranged in descending order of latitude) and the values of the MAE, RMSE, MAPE metrics for the initial IRI-Plas model, the adapted IRI-Plas model and the median. A row of average values is also given, in which the most accurate values are highlighted. For foF2, the most accurate was the adapted model with average values of MAE = 0.77 MHz, RMSE = 1.01 MHz, MAPE = 13.88%. It can be noted that these values are, for example, at the level of the global neural network forecast for much less disturbed conditions [8]. Moreover, RMSE and MAPE for the initial model provided a result better than the median.

Table 2. Statistics of correspondence between model hmF2 values and experimental data.

hmF2	MAE, MHz			RMSE, MHz			MAPE, %		
	Plas	Plas		Plas	Plas		Plas	Plas	
station	init	adapt	med	init	adapt	med	init	adapt	med
Tromso	27.87	21.21	11.10	32.83	26.13	14.54	10.89	8.67	4.82
Juliusru	52.76	43.93	31.06	74.10	65.22	44.29	24.73	21.76	14.78
Dourbes	48.09	43.47	24.12	64.05	61.19	40.82	20.33	19.43	12.96
Pruhoni	45.71	39.95	31.61	65.38	58.89	47.63	20.24	18.23	14.75
Sopron	63.31	60.26	26.43	71.12	68.97	36.10	22.87	22.18	11.61
Roquet	47.40	48.15	39.15	74.82	72.58	76.40	20.95	20.32	21.39
SanVito	52.00	51.92	40.32	72.46	72.70	67.51	21.50	21.57	20.03
Athens	47.97	42.75	28.04	64.26	61.71	48.64	20.51	19.69	15.52
Arenosi	46.73	43.74	43.16	68.21	63.53	68.10	19.22	17.90	19.19
Ascens	34.84	36.50	26.35	54.85	58.03	48.67	17.94	18.98	15.92
mean	46.67	43.19	30.13	64.21	60.89	49.27	19.92	18.87	15.10

For the hmF2 parameter, the situation differs: the highest accuracy is provided by using medians. The values of both models are close to each other and provide lower accuracy than the medians, due to the fact that the IRI-Plas model does not reflect a significant increase in hmF2 during disturbances. At the same time, the relative error in determining hmF2 for medians is close to the relative error of foF2 for the adapted model. This indicates the direction of modification, especially since the author of the model paid serious attention to this problem and very good agreement with experimental data is seen outside of a very strong disturbance [9]. As for the TEC values, the adapted model showed the best results, and even the initial model provided better results than the median.

Table 3. Statistics of correspondence between model values of TEC and experimental data.

TEC	MAE, TECU			RMSE, TECU			MAPE, %		
	Plas	Plas		Plas	Plas		Plas	Plas	
station	init	adapt	med	init	adapt	med	init	adapt	med
Tromso	5.58	1.46	2.90	6.01	1.62	3.26	30.5	8.25	16.6
Juliusr	5.01	1.39	6.40	6.19	1.82	8.65	28.8	8.47	40.3
Dourbe	3.85	1.06	6.79	5.05	1.54	9.18	22.6	6.91	41.1
Pruhon	4.14	1.14	6.90	5.34	1.62	9.32	23.1	7.03	40.4
Sopron	3.99	1.08	7.26	5.03	1.54	9.50	20.9	6.40	39.4
Roquet	5.10	1.36	8.18	5.95	1.65	10.31	21.7	6.04	37.6
SanVit	5.46	1.48	8.25	6.39	1.79	10.26	22.6	6.36	36.4
Athens	6.73	1.80	8.85	7.83	2.16	11.05	25.5	7.04	36.0
Arenos	5.01	1.27	8.49	6.17	1.61	10.77	21.7	5.67	37.9
Ascens	11.12	2.20	8.32	15.2	3.18	11.49	34.9	7.29	26.3
mean	5.60	1.42	7.23	6.92	1.85	9.38	25.2	6.95	35.2

To illustrate the latitudinal dependence, Fig. 4 shows the RMSE metrics for all parameters that detail the derivation of average values.

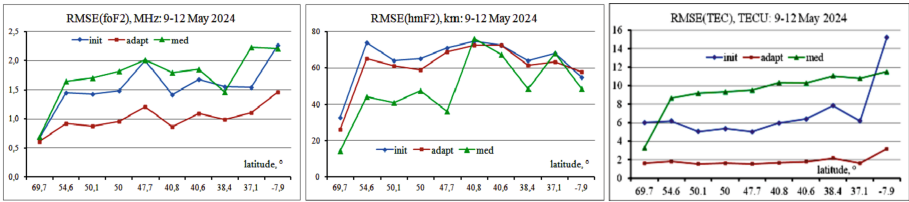


Fig. 4. Comparison of the accuracy of parameter determination during a disturbance using RMSE as an example

Since RMSE depends on the absolute value of the parameter, and the foF2 and TEC values can increase with latitude, a certain trend of increasing these values is visible.

In conclusion of this subsection, Fig. 5 presents the latitudinal dependence of the correlation coefficients between the TEC and foF2 parameters calculated for the periods of a month (icon month) and May 9–12, 2024 (icon dist).

With the exception of the ρ value for the Athens station during the disturbance period (it is also significant), all coefficients have very high values in the range of 0.84–0.9 for the month and 0.84–0.93 for the disturbed period, indicating the interchangeability of the parameters and the possibility of using TEC to study the state of the ionosphere during this disturbance.

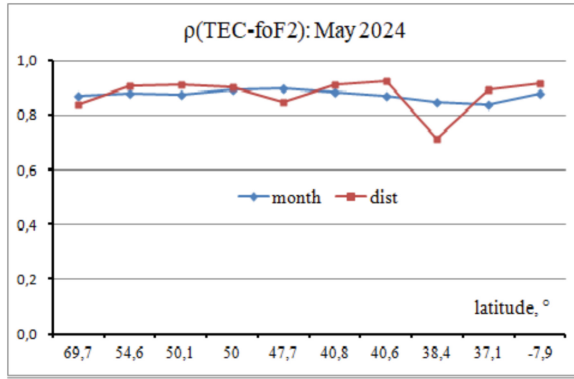


Fig. 5. Correlation of the TEC and foF2 parameters during the full month and the disturbance period of May 9–12, 2024

3.2 Latitudinal Variations Features of the TEC Parameter Along the 15° E Meridian

Already the incomplete data set in Sect. 3.1 shows that some latitudinal dependence may exist and the behavior in the southern hemisphere may differ from the situation in the northern hemisphere. A preliminary idea can be obtained from Fig. 6, which shows the curves for the experimental values of TEC(obs), medians TEC(med) and relative deviations δTEC for the meridian 15° E in the latitude range 50°–60° in each hemisphere, where the motion of such structures as the oval, the trough and others occurs.

In the upper panel, the curves are given for four days. Additionally, there is the day of May 9, used as a reference one. Differences in absolute values, as well as in the nature of variations, are visible. In the southern hemisphere, a stronger reaction to the sudden onset of the MS is visible. The behavior of the medians in the southern hemisphere has a larger spread between the minimum and maximum values and a longer period of low TEC values, which leads to an extremely large positive disturbance in the third panel in the period close to the minimum Dst, while in the northern hemisphere, from the very beginning of the MS, a negative main phase was observed, which passed into a two-stage negative recovery phase.

Examples of latitudinal distributions for several important moments are given in Fig. 7. These moments are: May 10, 2024, UT20, the beginning of the ionospheric reaction after SSC in the region of UT17, May 11, 2024, UT02, the moment of the minimum value of the Dst index and the end of the main phase, May 11, 2024, UT20, the moment of negative disturbance in the recovery phase, May 12, 2024, UT08, the moment of the deep recovery phase. The left panel shows the behavior of TEC together with the medians, the right panel shows the corresponding deviations of δTEC .

For all cases, a significant asymmetry in the TEC behavior is visible in the two hemispheres. In the first panel, in the northern hemisphere, a shift of the trough to the latitude of 50° N, a decrease in the crest of the northern part of the equatorial anomaly, and a shift in the southern crest to a greater negative latitude are visible. In the region of 35° S–40° S, a shift in the trough is visible, which may be responsible for the auroral glow

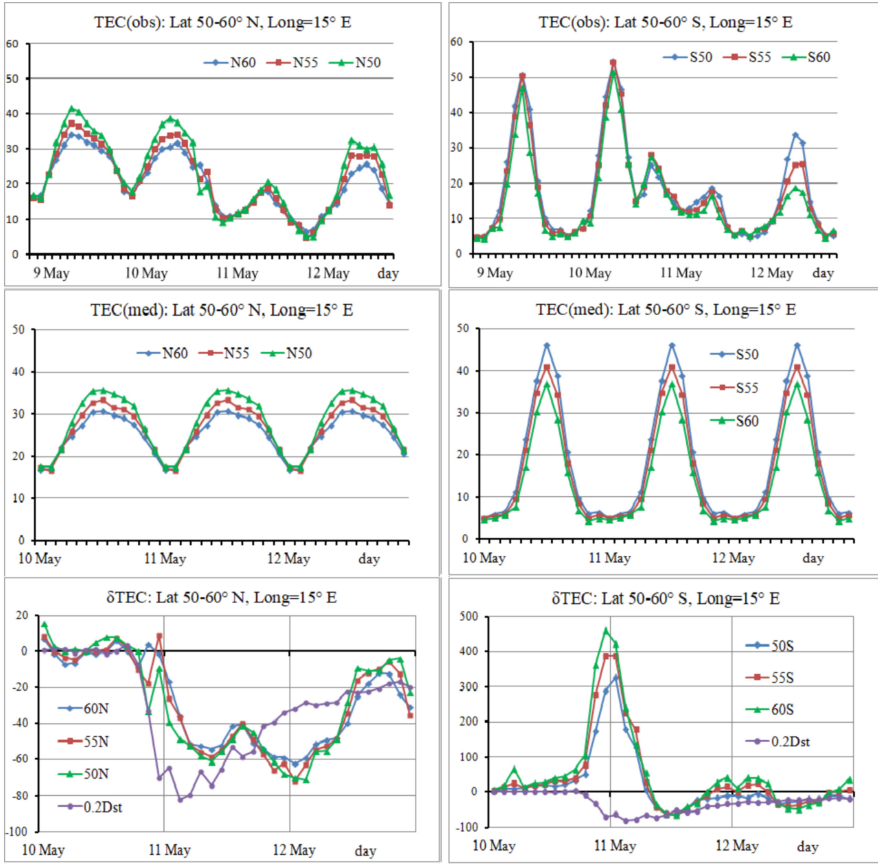


Fig. 6. Behavior of the parameters related to TEC during the disturbance

in this zone, as follows from the map of the paper [4]. In the southern hemisphere, the largest values of the δTEC deviation are observed. At UT02 on May 11 (the second panel), a strong negative disturbance is obvious ($\delta\text{TEC} \leq 50\%$), in the southern hemisphere a positive disturbance is observed, the troughs retained their positions. At UT20 on May 11 (the third panel), the trough in the northern hemisphere shifted to 55°N , and the negative disturbance captured a part of the southern hemisphere. In the last panel, the situation is close to symmetrical with negative disturbance everywhere except the equatorial zone. Figure 8 shows the metrics of the correspondence between the model and experimental TEC values for the initial and adapted IRI-Plas models, as well as for the medians.

The most noticeable feature is the reflection of the presence of the equatorial anomaly in the TEC data, with different values of the crests in the hemispheres. It should be noted that if the median values are taken for a month (and not for the disturbed period, as in Fig. 8), they will be smaller, as well as the crests, the difference in the crest values will decrease, but the presence of the equatorial anomaly will remain. As for the comparison of metrics, the most accurate are the values of the adapted model, for which the average

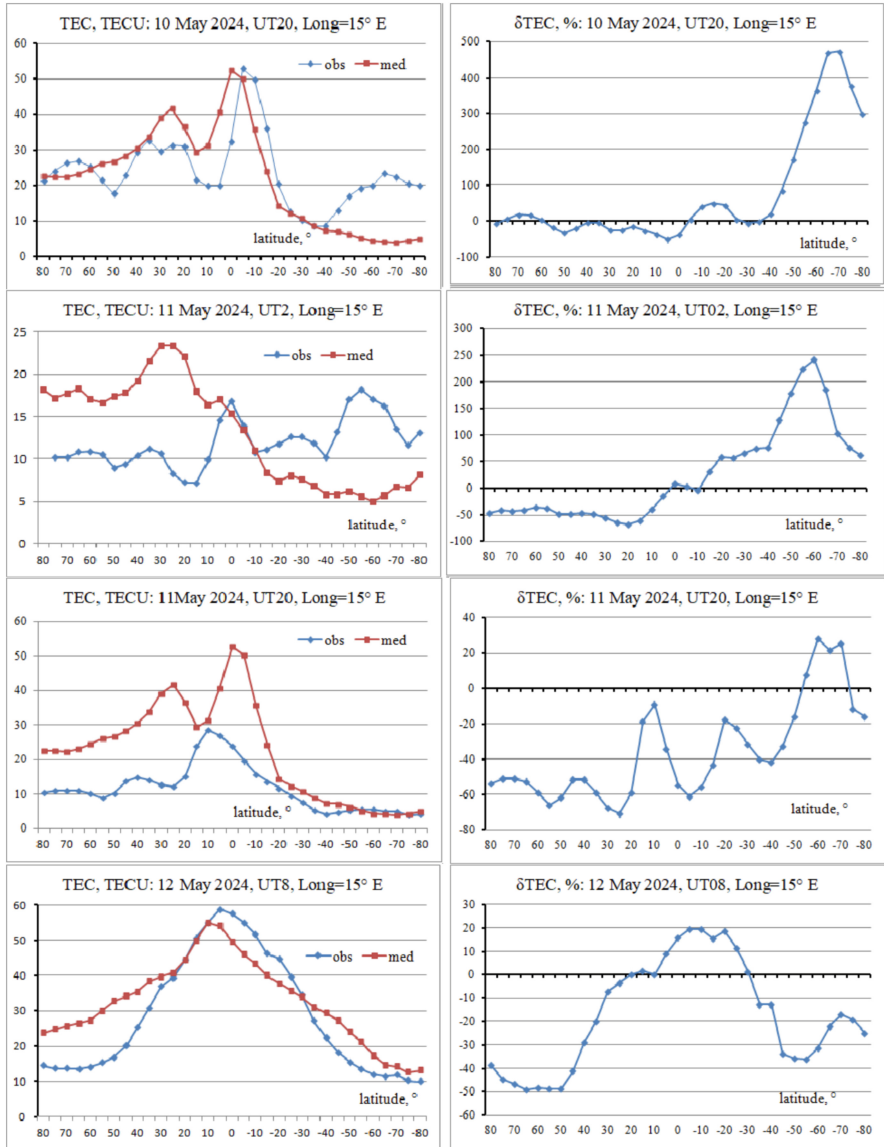


Fig. 7. Examples of asymmetry of the latitudinal distribution of TEC along the 15° E meridian

values are: $\text{MAE} = 1.56 \text{ TECU}$, $\text{RMSE} = 2.08 \text{ TECU}$, $\text{MAPE} = 8.88\%$. This shows that the adapted model can be used to estimate the components of TEC, which is carried out in the next section.

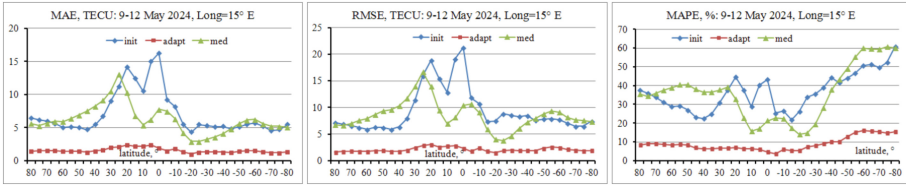


Fig. 8. Comparison of TEC metrics using the IRI-Plas model and the median

3.3 Response of TEC Components to the Disturbance of May 9–12, 2024

Figure 9 shows the latitudinal dependences of the contributions of various parts of the $N(h)$ -profiles Parts of TEC (left graphs) and changes in these contributions Δ Parts of TEC during the development of the MS (right graphs) for the same moments as in Fig. 7.

Here we can also see the difference between the two hemispheres, related to the redistribution of the TEC contributions depending on the latitude and the phase of the MS. In the quiet state, the contributions change little and are approximately from 70% to 60% for the topside EC_{top} , from 20% to 30% for the bottomside and $\sim 10\%$ for the plasmaspheric part EC_{pl} (the fourth panel of Fig. 3) with some diurnal variation. In each panel, there is a redistribution of contributions mainly between EC_{top} and EC_{pl} . The first moment is related to the onset of the MS. In the southern hemisphere in Fig. 7, we saw a large positive disturbance, which apparently occurred due to an increase in ionization in the topside and its decrease in the plasmasphere, as shown by the right graph of the first panel of Fig. 8. At the time of the Dst minimum (the left panel) in Fig. 7, there was a negative disturbance in the northern hemisphere and a positive disturbance in the southern hemisphere. It is evident that in the northern hemisphere there was a redistribution of ionization between EC_{top} and EC_{pl} , in the southern hemisphere this redistribution changed sign, while the contributions of EC_{bot} and EC_{pl} remained at the same level. At the moment of May 11 UT20, when the negative disturbance continued to exist in the northern hemisphere, it affected the southern hemisphere, in the high-latitude zone of which the contribution of EC_{top} decreased and EC_{pl} increased. In the fourth panel in the high-latitude zone the share of topside decreased due to some increase in bottomside and in the equatorial zone of the southern hemisphere the contributions returned to the initial state with a small positive deviation of δTEC and a negative disturbance due to topside variations. It is evident that everywhere the contributions lie in the range $(-15\% \div 15\%)$ and there is a constant redistribution of ionization between the upper ionosphere and the plasmasphere, however, to confirm this picture it is necessary to compare the $N(h)$ profiles and preferably with the profiles of satellites such as COSMIC.

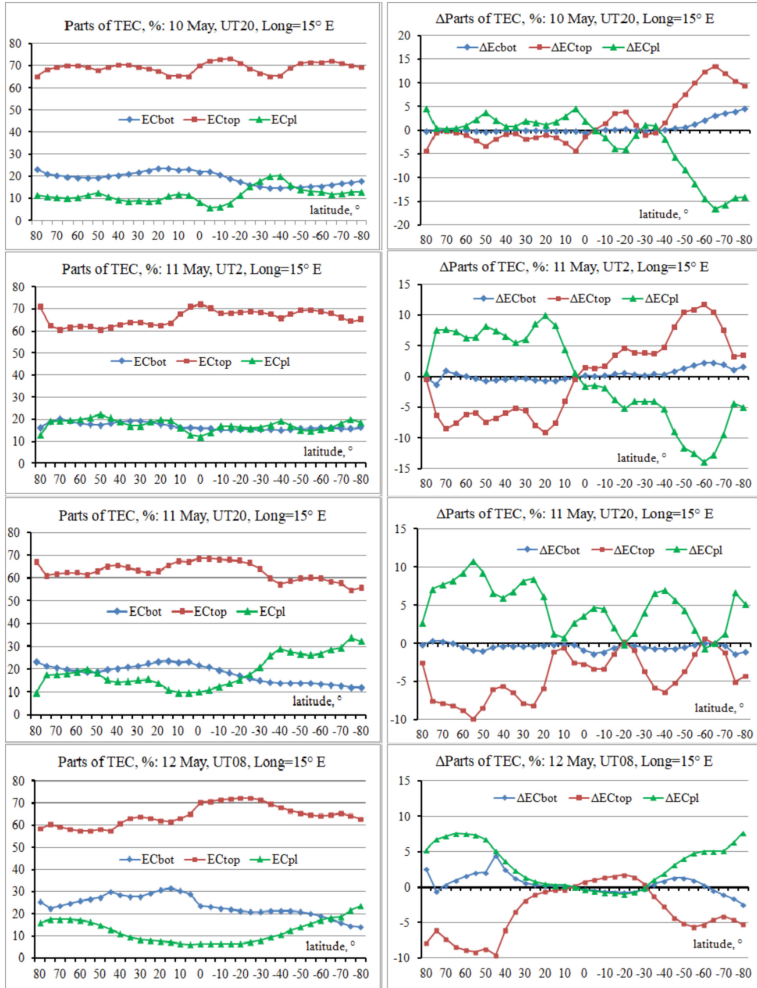


Fig. 9. Latitude dependence of the redistribution of TEC contributions in the process of MS development

4 Conclusion

Before drawing a conclusion on the specific results of this paper, we would like to note some fact regarding the historical aspect of this work. As is known, with the organization of the 1st International Conference on Telecommunications and Remote Sensing August 29–30, Sofia, Bulgaria by IICREST in 2012, a platform appeared on which it was possible to present the results of ionospheric research in support of telecommunication and navigation systems. It was at this time that the intensive use of total electron content (TEC) began. Employees of the Research Institute of Physics SFU took an active part in these conferences. Efforts were aimed at obtaining results that would enable the use of TEC to determine the conditions of radio wave propagation in the ionosphere, including

the determination of the critical frequency f_oF2 . A large role in this was given to the empirical IRI-Plas model due to its specific properties [10]. The studies were carried out for various space weather conditions, including during several geomagnetic disturbances. The model was tested, among other things, using data from satellites such as COSMIC and Swarm. However, the entire period of the conferences, which lasted more than one solar cycle, was relatively quiet in terms of space weather, despite the fact that the year 2014 was the year of the maximum of the 24th cycle, and the year 2015 was one of the most disturbed during this period. And in May 2024 there was a powerful magnetic storm (superstorm). This event allowed us to pose the following questions: (1) whether the ionosonde measurements are correct, (2) whether the f_oF2 and TEC parameters are interchangeable, (3) whether the IRI-Plas empirical model corresponds to the experimental data, (4) are there any features in the behavior of the ionospheric parameters in the two hemispheres? The results of using data from 10 ionosondes and 33 GPS receiver points along the 15° E meridian showed that this powerful disturbance did not allow measurements of the f_oF2 , h_mF2 parameters at certain moments.

Quantitative assessments of the IRI-Plas model accuracy for an extremely strong disturbance and a whole month showed that (1) for f_oF2 , the adaptation of the model to the experimental $TEC(obs)$ values improves the accuracy compared to the initial model, (2) when determining h_mF2 , both versions of the model do not provide sufficient accuracy and do not reflect the nature of the change in this parameter, which showed a huge positive splash. Good agreement between the TEC values for the adapted model and the experimental data made it possible to distinguish the contributions of different parts of the $N(h)$ profile to TEC and to show that during disturbances there is a constant redistribution of ionization between the upper ionosphere and the plasmasphere within $\pm 15\%$. That points to the important role of the plasmasphere and the need for a detailed study of its behavior during disturbances.

There are many aspects of the influence of magnetic disturbances on various areas of science, technology and these aspects will be the subject of many next papers. It is also possible to intersect and supplement different papers, use the same data. For example, in the paper [5] also used data from the Ascension island ionospheric station and gave an explanation of extraordinary postsunset rise of h_mF2 around 300 km to more than 500 km, while the ionospheric electron density profiles showed a notable depletion during this period: this drastic enhancement in h_mF2 and coinciding substantial reduction in electron density have been caused by the deep equatorial trough associated with the super-fountain effect. The results of using TEC also coincided: the paper [5] showed that a significant negative phase on May 11 was also observed on a global scale.

Due to the complexity of the events that occurred, the results of the paper have certain limitations. First of all, this is limited to the European region (meridian 15° E), however, due to the huge longitudinal dependence of the properties of the ionosphere, the features of its behavior on other meridians will be different. Moreover, a detailed interpretation of many aspects of the results obtained is necessary, which can be helped by the paper [11], representing a description of many physical processes that take place specifically during the period of the storm under study.

Acknowledgments. The TEC samples data was obtained from <https://cddis.nasa.gov/archive/gnss/products/ionex/>, foF2 data downloaded on the website <https://giro.uml.edu/didbase/>. Data on solar and geomagnetic activity was taken from SPDF OMNI-Web Service <http://omniweb.gsfc.nasa.gov/form/dx1.html>. Calculations using the IRI-Plas model were performed online on the website (<http://www.ionolab.org/index.php?language=en>). The research was financially supported by Ministry of Science and Higher Education of the Russian Federation (State contract GZ0110/23-10-IF).

References

1. Spogli, L., Alberti, T., Bagiacchi, P., Cafarella, L., Cesaroni, C., et al.: The effects of the May 2024 mother's day superstorm over the Mediterranean sector: from data to public communication. *Ann. Geophys.* **67**(2), PA218 (2024). <https://doi.org/10.4401/ag-9117>
2. Gonzalez-Esparza, J.A., Sanchez-Garcia, E., Sergeeva, M., Corona-Romero, P., Gonzalez-Mendez, L.X., et al.: The Mother's Day geomagnetic storm on May 10, 2024: aurora observations and low latitude space weather effects in Mexico. *Space Weather* **22**, e2024SW004111 (2024). <https://doi.org/10.1029/2024SW004111>
3. Hajra, R., Tsurutani, B.T., Lakhina, G.S., Lu, Q., Du A.: Interplanetary causes and impacts of the 2024 may superstorm on the geosphere: an overview. *Astrophys. J.* (2024). <https://arxiv.org/abs/2408.14799>
4. Hayakawa, H., Ebihara, Y., Mishev, A., et al.: The solar and geomagnetic storms in May 2024: a flash data report preprint (2024). <https://doi.org/10.48550/arXiv.2407.07665>
5. Aa, E., Chen, Y., Luo, B.: Dynamic expansion and merging of the equatorial ionization anomaly during the 10–11 May 2024 super geomagnetic storm. *Remote Sens.* **16**, 4290 (2024). <https://doi.org/10.3390/rs16224290>
6. Evans, J.S., et al.: GOLD observations of the thermospheric response to the 10–12 May 2024 Gannon superstorm. *Geophys. Res. Lett.* **51**, e2024GL110506 (2024). <https://doi.org/10.1029/2024GL110506>
7. Radicella, S.M.: New ways to modelling and predicting ionosphere variables. *Atmosphere* **14**, 1788 (2023). <https://doi.org/10.3390/atmos14121788>
8. Otugo, V., Okoh, D., Okujagu, C., Onwuneme, S., Rabiou, B., Uwamahoro, J., et al.: Estimation of ionospheric critical plasma frequencies from GNSS - TEC measurements using artificial neural networks. *Space Weather* **17**, 1329–1340 (2019). <https://doi.org/10.1029/2019SW002257>
9. Gulyaeva, T.L.: Empirical model of ionospheric storm effects on the F2 layer peak height associated with changes of peak electron density. *J. Geophys. Res.* **117**, A02302 (2012). <https://doi.org/10.1029/2011JA017158>
10. Maltseva, O.A., Mozhaeva, N.S., Zhabankov, G.A.: Advantages of the new model of IRI (IRI-Plas) to simulate the ionospheric electron density: case of the European area. *Adv. Radio Sci.* **11**, 307–311 (2013). <https://doi.org/10.5194/ars-11-307-2013>
11. Astafyeva, E., Maletkii, B., Förster, M., et al.: Extreme ionospheric uplift and a remarkable negative storm phase during the 10–11 May 2024 geomagnetic superstorm. *ESS Open Archive* (2024). <https://doi.org/10.22541/essoar.173325230.07581097/v1>



UAV Detection and Recognition Technologies

Magdalena Garvanova¹, Ivan Garvanov¹(✉), Daniela Borissova^{1,2},
Nurassyl Kerimbayev³, and Zhanbota Menlibay³

¹ University of Library Studies and Information Technologies, Sofia, Bulgaria
{m.garvanova,i.garvanov}@unibit.bg,
daniela.borissova@iict.bas.bg

² Institute of Information and Communication Technologies, Bulgarian Academy of Sciences,
Sofia, Bulgaria

³ Al-Farabi Kazakh National University, Almaty, Kazakhstan

Abstract. The use of drones for both military and civilian purposes has significantly increased in recent years. Their affordability and extensive capabilities for solving a wide range of tasks, including entertainment, make them very attractive to a broad audience. Unfortunately, incidents involving drones are constantly increasing, necessitating the introduction of regulatory requirements for their use in conjunction with the use of technologies for their detection, recognition, classification, tracking, and eventual interception. This paper attempts to classify existing unmanned aerial vehicles based on their parameters and purposes. The research analyses technologies for the detection and recognition of unmanned aerial vehicles (UAVs) based on radar, radio frequency, optics and acoustics.

Keywords: Drone detection and recognition · optoelectronic · thermal imaging · acoustic · radio frequency · radar systems

1 Introduction

Unmanned aerial vehicles (UAVs), also known as drones, are manned aircraft without a pilot [1]. They may be remotely controlled or have autonomous control systems. The idea of creating radio-controlled devices arose as early as 1898 by the world-famous scientist Nikola Tesla, who first used a radio signal to control boats [2]. Recent years have seen an increase in the application of UAVs for both military and civilian purposes [3]. This is due both to the developed constructive solutions and night vision technologies [4]. Unfortunately, there are also incidents with drones, as the damage they cause is significant [5, 6]. These incidents can be both accidental and intentional, necessitating the development of systems for detection, recognition, and, if necessary, the blocking of drones. Detection technologies are also diverse, possessing various technological characteristics that make them effective under certain conditions and ineffective under others. The most common drone detection technologies utilize radar, video cameras, thermal cameras, radio receivers to detect drone communication, microphones, and combinations thereof [7].

The current paper proposes a classification of unmanned aerial vehicles according to their technical characteristics and their application in practice. The research analyses technologies for the detection and recognition of unmanned aerial vehicles (UAVs) based on radar, radio frequency, optics and acoustics.

It is organized as follows: Sect. 2 focuses on the types of drones according to their technical characteristics and their application. Section 3 analyses the main technologies for UAV detection and recognition. Finally, we conclude our study in Sect. 4.

2 UAV Classification

Unmanned aerial vehicles have different technical characteristics, are equipped with various sensors and devices and are widely used in the world around us. According to the type of control, UAVs are either manual-remote control or automatic control through sensors, microprocessors and other electronic devices [8]. Drones communicate over short and long distances using wireless technology. Depending on how they fly, drones are classified as rotary, fixed wing and hybrid. Drones that are powered by motors (rotors) and do not have fixed wings are called rotorcraft. These drones are the most common category of drones. The advantage of these drones is that they can take off and land vertically. They can also remain in the air relatively still (hang) for a long period of time. As a disadvantage of these drones is the limited duration of the flight, which depends on the durability of their battery. They also have a severe limitation in movement speed. Depending on the number of rotors, these drones have specific characteristics on which their application in practice depends. Fixed-wing drones are similar to airplanes. They move only forward, use the lift of their wings, can develop higher speeds and cover longer distances. Taking them off requires a special setup, and landing requires a runway. Their main disadvantage is that they cannot take off and land vertically, and they cannot stay in one place in the air. They are driven by an engine, which is usually a rotor, but gas engines can also be used. Hybrid drones are less common in practice, but they combine the above technologies using the advantages of a wing and multiple rotors. They combine the advantages of both types of drones. Drones with alternative power sources, such as gasoline-electric, etc., are also hybrid. However, they are currently more expensive and more difficult to manage. Military drones are categorized based on their weight, flight range, speed, as well as their specific capabilities. NATO uses a classification according to the US Department of Defence and divides drones into three classes as shown in Table 1 [9].

Class I UAVs, being smaller in size, are usually portable, manually launched, and controlled by a separate controller. They typically have a range of less than 20 miles and an endurance of up to two hours. They are sub-categorized as micro, mini and small ones.

Class II UAVs are medium-sized tactical systems that can fly up to 10,000 feet above ground level (AGL) with a mission radius of 200 km (line of sight).

On the other hand, Class III fixed-wing UAVs, unlike Class I, require take off and recovery runways and additional logistical support and infrastructure. They also have more airspace management considerations comparable to manned aircraft. Class III UAVs include medium-altitude long-endurance aircraft and high-altitude long-endurance aircraft.

Table 1. NATO Unmanned Aircraft Systems (UAS) classification [9]

NATO UAS CLASSIFICATION						
Class	Category	Normal Employment	Normal Operating Altitude	Normal Mission Radius	Primary Supported Commander	Example Platform
Class III (>600 kg)	Strike or Combat	Strategic/National	Up to 65,000'	Unlimited (BLOS)	Theater	MQ9 Reaper
	HALE	Strategic/National	Up to 65,000'	Unlimited (BLOS)	Theater	Global Hawk
	MALE	Operational/Theater	Up to 45,000' MSL	Unlimited (BLOS)	JTF	Heron
Class II (150 kg – 600 kg)	Tactical	Tactical Formation	Up to 10,000' AGL	200 km (LOS)	Brigade	Hermes 450
Class I (<150 kg)	Small (>15 kg)	Tactical Unit	Up to 5,000' AGL	50 km (LOS)	Battalion, Regiment	Scan Eagle
	Mini (<15 kg)	Tactical Sub-Unit	Up to 3,000' AGL	Up to 25 km (LOS)	Company, Platoon, Squad	DJI Mavic 3
	Micro (<66 J)	Tactical Sub-Unit	Up to 200' AGL	Up to 5 km (LOS)	Platoon, Squad	Black Hornet

Civilian drones can be classified according to their technical characteristics and their purpose. The classification of unmanned aerial vehicles based on flight height, flight duration, flight range, payload is shown in Table 2.

Table 2. UAV categorization on altitude [1]

Category	Endurance (h)	Flight alt. (m)	Range (km)	Mass (kg)
Low altitude deep penetration (LADP)	0.5–1	50–9000	>250	250–2500
Low altitude long endurance (LALE)	>24	3000	>500	15–25
Medium altitude long endurance (MALE)	24–48	3000	>500	1000–1500
High altitude long endurance (HALE)	24–48	20,000	>2000	2500–5000

Civilian UAVs are used to obtain high-resolution images of remote areas, islands, mountain peaks and coastlines, etc. [10–12]. Thanks to UAVs, remote sensing data is greatly improved for comparison with space and ground data obtained from satellites. The low cost and suitable characteristics of UAVs offer quality surveillance with high

temporal and spatial resolution. Remote sensing capabilities from unmanned aerial vehicles support water quality monitoring, land monitoring, oil and gas, yield assessments, hydrologic modelling, biodiversity conservation, geological surveys, disasters, terrain monitoring, forest mapping, and forest monitoring. cultures. This technology is also used for mapping and creating 3D maps, as well as mapping archaeological sites. The use of UAV in remote sensing with different application is shown in Fig. 1.

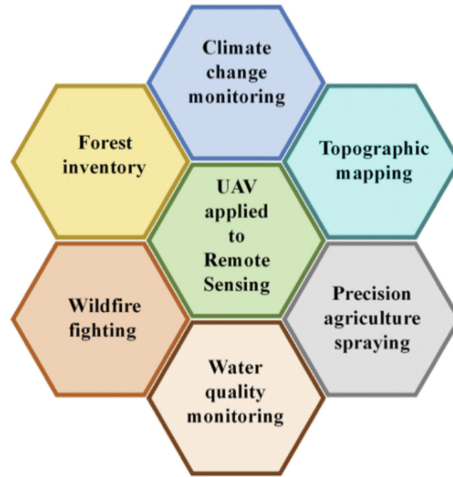


Fig. 1. UAV and remote sensing applications [11]

3 UAV Detection and Recognition Technologies

Drone detection technologies use: radar, radio frequency detection, acoustics and optoelectronic detection [13–18] are shown in Fig. 2.

Radar detection is the predominant method for detecting and tracking large UAVs by processing radar signals [13]. The effectiveness of these systems depends on the size of the UAV, the flying height, the specific characteristics of the radar, radio interference, etc. RF (radio frequency) detection analyses the electromagnetic signals emitted by the UAV [14]. This method requires sophisticated equipment and is susceptible to interference. A major drawback is its limited ability to determine the location of the drone. Optoelectronic detection and recognition uses cameras [15]. This method allows accurate determination of coordinates but depends on lighting and weather conditions. This technology has a shorter UAV detection range than radars but provides very good target recognition. During the dark part of the day, it is possible to use thermal cameras which can similarly detect the target [16]. Acoustic recognition systems analyse the sound signals generated by the UAV [17]. They can detect targets at close range and are very sensitive to noise. The accuracy of determining the location of the sound source is low. To achieve higher efficiency in the detection and classification of UAVs, it is proposed to use Sensor Fusion systems that integrate the considered technologies [18].

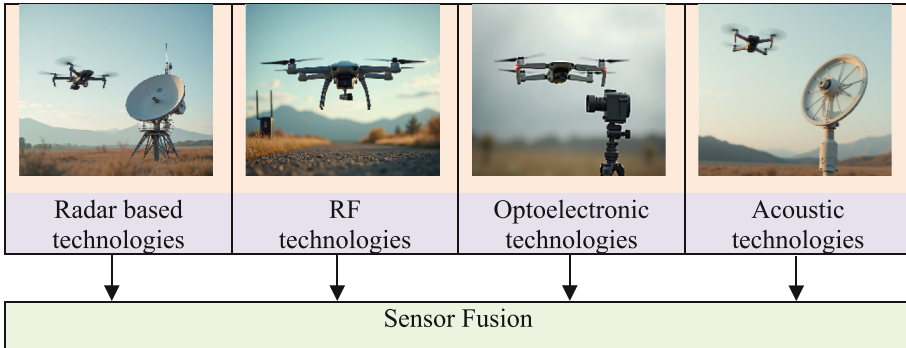


Fig. 2. Diagram of modern UAV detection and recognition systems

3.1 UAV Detection and Recognition Technologies Based on Radar Systems

The radar systems are intended for detecting various moving objects and establishing their current position, as well as determining velocities and trajectories for moving objects. This is achieved by transmitting an electromagnetic (EM) wave from the transmitting antenna. If the target is present within the radar coverage area, the wave will be reflected back to the receiving antenna, and all the information collected at the receiver will then be analysed to determine the above parameters.

In the practice, there are different types of radar systems, based on the transmitter-receiver topology as in the monostatic radar, the transmitter and the receiver are spatially combined. Bistatic radar consists of a single transmitter and single receiver which are separated specially by a distance, which is comparable to that of the maximum range of target. Forward scattering radar (FSR) is a special case of bistatic radar, where it is designed to detect and track targets moving in the narrow region along the base line. The FSR offers some peculiarities which make the radar interesting. The most attractive features include: the essential increase in the power budget, in the directions close to the base line, results in a significant increase in the target radar cross section, and it is stated that the RCS, at the forward scattering, is bigger than in the monostatic case by 30–40 dB, which further improves the radar system sensitivity depending on the frequency band [19].

Radar detection is a method for detecting, recognition and tracking large UAVs by processing radar signals [13]. In UAV radar recognition systems, some technologies can be distinguished that are combined with each other for the purpose of detection and classification [20–22]:

1. Radar Cross Section (RCS) analysis;
2. Machine learning and Deep learning;
3. Micro-Doppler signature analysis;
4. Statistical recognition;
5. Use of radar spectrograms;
6. Use of multi-frequency radars.

In this paper, a test for detecting a low-flying aircraft using a forward scattering (FS) radar system using a GPS receiver of a GPS signal from a satellite is made. The moving target is detected at the moment of crossing the radio barrier between the receiver and the transmitter. The topology of the experiment is shown in Fig. 3, while in Fig. 4 is demonstrated a photo of the plane flying over. As the airplane crossed the radio barrier between the satellite and the receiver (Fig. 3), it briefly blocked the GPS signal (Fig. 5).



Fig. 3. Forward Scattering Radar System



Fig. 4. Aircraft crossing the radio barrier GPS receiver – GPS transmitter

After integrating the GPS navigation message with a sliding window duration of 300 ms in MATLAB environment, the result shown in Fig. 6 presented the moment of crossing the radio barrier.

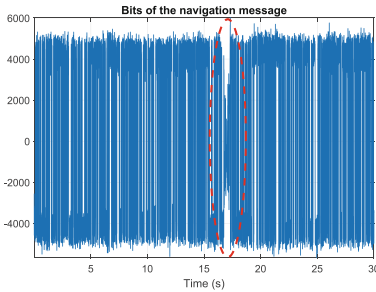


Fig. 5. GPS signal at the moment of passing aircraft

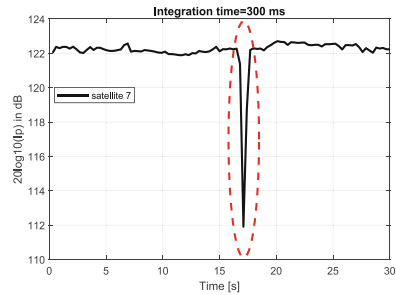


Fig. 6. GPS signal after integrating the signal with a sliding window

If appropriate signal processing is applied, it is possible to obtain characteristics by which to identify, classify and recognize the detected object.

3.2 UAV Detection and Recognition Technologies Based on RF

The RF approach to detecting and classifying drones is applicable to radio-controlled drones or drones that support radio communication with the control centre [23]. The range of detection depends on factors such as the RF amplification chain, hardware components, and software processes involved in the system. Wi-Fi signals can be strongly attenuated with distance and the presence of obstacles. To ensure drone detection from significant distances, the detection system should detect weak Wi-Fi signals. An RF

amplification chain is then required. By utilizing the radio frequency characteristics of drones, they can be detected, identified, and categorized. The drones can use the Wi-Fi standard or enhanced Wi-Fi for communication, as well as drones equipped with Wi-Fi Remote ID or enhanced Wi-Fi DJI Drone ID signals. This means that radio-controlled drones can be divided into:

- Drones that communicate using the Wi-Fi standard protocol within the ISM band.
- Drones that transmit a Wi-Fi RDID beacon on channel 6 (at 2437 MHz) within the 2.4 GHz Wi-Fi band.
- DJI drones that transmit the enhanced Wi-Fi DJI Drone ID signal. The specific channel used by these drones is pseudo-random and can be within either the 2.4 GHz or 5.8 GHz ISM band.

In this paper, an attempt has been made to detect a drone using Software Defined Radio (SDR). This technology for processing radio signals from drones is a relatively inexpensive and convenient way to detect and recognize them. By receiving signals from the drone's radio controller through high-gain signal reception antennas combined with highly sensitive receiving systems, drone detection at long distances is achieved (Fig. 7). In the presence of suitable equipment for recognizing the radio-controlled signals of the drone, they can be jammed to block the drone's control or more powerful control radio signals can be transmitted, allowing the drone's control to be taken over by an anti-drone system.

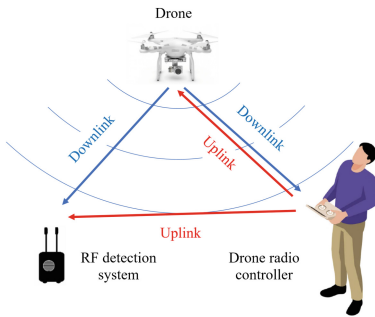


Fig. 7. Experimental topology

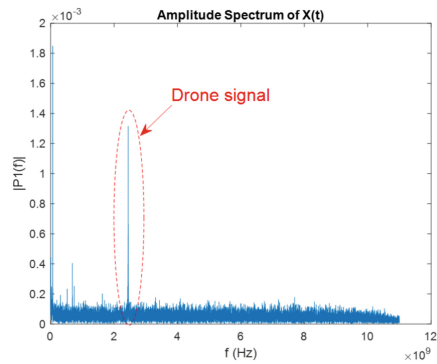


Fig. 8. Signal spectrum in the presence of a drone

Through software-defined radio PlutoSDR, a recording of the control radio signal for the PHANTOM 3 ADVANCED drone was made, and with the help of an algorithm implemented in MATLAB, this radio signal was detected. The spectrum of the signal in the presence of the drone, obtained with FFT, is depicted in Fig. 8, where the signal from the drone exhibits a clearly pronounced peak. Automatic detection of this frequency component can be achieved using the automatic detector.

3.3 UAV Detection and Recognition Technologies Based on Optoelectronic System

Optical-electronic systems for the detection and recognition of drones are used for relatively short distances. These systems can be classified according to technical means and classification technologies.

The classification by technical means shall be:

- Systems based on optical surveillance cameras, applicable to the light part of the day (video camera) [24, 25];
- Systems based on thermal imaging infrared sensors, applicable in poor visibility in fog, rain or the dark part of the day (thermal camera) [24];
- Systems based on laser-optical sensors (LiDAR) [26].

The classification-by-classification technologies shall be:

- Deep learning [25];
- Machine learning [25].

Various algorithms exist for processing video recordings to detect and recognize drones, but one of the most effective ones at present is the YOLO (You Only Look Once) software, which utilizes machine learning algorithms and artificial intelligence to make decisions regarding the presence or absence of drones. For this software to work well, the video needs to be of high quality. The advantage of the algorithm over others is that it allows for simultaneous detection and recognition of the drone. Example results from the operation of the YOLO software are shown in Figs. 9 and 10, where flying objects are detected and recognized. For the experiment, the drone DJI Matrice 350 RTK Combo with dimensions of $81 \times 67 \times 43$ cm was used.

The obtained results indicate that the algorithm detects and recognizes the drone, with a higher probability of recognition when the drone is closer to the camera and the image quality is higher. The same algorithm can be applied for detecting drones through processing thermal images obtained from a thermal camera, with successful recognition requiring the use of a specially trained model for this purpose.

The drawback of detecting unmanned aerial vehicles during poor visibility in fog, rain or at the dark part of the day can be compensated for by using thermal cameras, which are not affected by illumination but rely solely on the infrared emission of heated objects [26].

By utilizing thermal images captured by a drone XMART OPTICAL FLOW SG900 drone with dimensions of $29 \times 29 \times 4$ cm during flight and applying a video processing algorithm [25], it is possible to detect the drone, as shown in Figs. 11 and 12. The distance between the camera and the drone is 3 and 9 m.

This technology is convenient for use during the dark part of the day, but it also has its drawbacks such as: a small usage perimeter, difficulty in drone recognition, and issues with detection in the presence of multiple heated objects. The technology is suitable for use in combination with another technology.

The algorithm presented in [16, 27] is based on the integration of several key elements to improve the quality of drone detection and classification through thermal image analysis. It is initially calculated on a highlight map that helps highlight areas where drones



Fig. 9. Detecting a drone at a distance of 30 m from the video camera

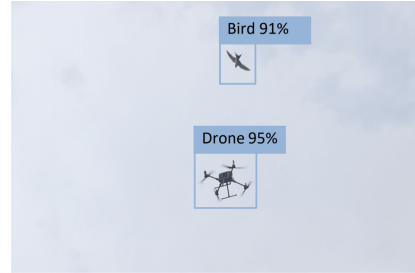


Fig. 10. Detecting a drone at a distance of 50 m from the video camera

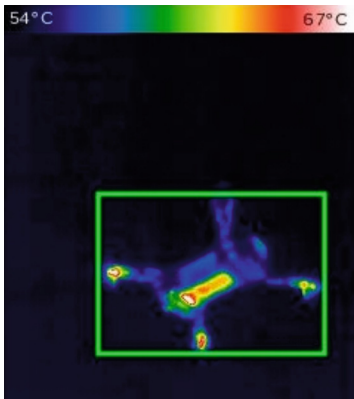


Fig. 11. Detecting a drone at a distance of 3 m from the thermal camera

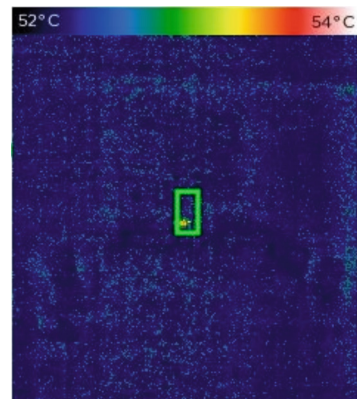


Fig. 12. Detection of a drone at a distance of 9 m from the thermal camera

are likely to be located in thermal images. This extraction map is combined with the Faster-RCNN neural network feature map to improve feature extraction and model training. A special ESO (enlarged small objects) module has been created which allows to magnify small drones in the input image, which helps the neural network detect them better. A data augmentation technique is proposed that enables the creation of new drone thermal images from different sources for training a neural network. The above components work together to provide more accurate and reliable UAV detection in a variety of scenarios and lighting conditions.

Drone species recognition and classification can be improved if additional colour feature processing is used as in [28, 29].

3.4 UAV Detection and Recognition Technologies Based on Acoustic System

Acoustic sensors represent another technology for drone detection and can be implemented using inexpensive microphones capable of capturing and identifying the distinct sound characteristics of different drone rotors [30]. These systems are effective both during daylight hours and in conditions of poor visibility. However, a significant drawback of acoustic systems is the relatively short detection range of drones due to the rapid

attenuation of sound signals in space. Acoustic systems are well-suited for monitoring small areas, such as inter-block spaces in urban environments. Expanding the operational range of an acoustic system is achieved by deploying multiple sensors distributed over a large area.

Acoustic systems for detecting and classifying drones are divided according to the principle of operation into active, passive and combined ones. Active acoustic systems work on the principle of radar, using transmitters to emit sound waves that bounce off the drone and return back. These systems can detect and recognize the type and model of the drone but have limited range. Passive acoustic systems use microphones to detect the sound produced by the drone's engine. These systems can be useful for detecting drones over long distances, but they cannot identify the type or model of the drone. Combining active and passive acoustic systems increases the probability of drone detection and recognition. Combination systems usually have a long range and can identify the type and model of the drone. The effectiveness of these systems depends on environmental noise, weather conditions, and the characteristics of the drone itself.

The algorithms for detecting and classifying drones based on acoustic sensors used technologies as: Machine Learning [31], Deep Learning [17] and Noise direction finding [32].

An algorithm has been developed in the MATLAB environment to explore the capabilities of this technology, processing audio signals from UAVs. To test the developed algorithm, audio signals obtained from a parabolic microphone (Fig. 13) during the flight of the XMART OPTICAL FLOW SG900 drone were used. A portion of the audio signal is shown in Fig. 14.

For the processing and subsequent recognition of the drone, signal processing needs to be performed in both the time and frequency domains of the signal. The spectrum of the signal, as well as its spectral characteristics, are shown in Figs. 15 and 16. To detect and recognize the drone, it is necessary to evaluate some of the characteristics of the audio signal.



Fig. 13. Parabolic microphone

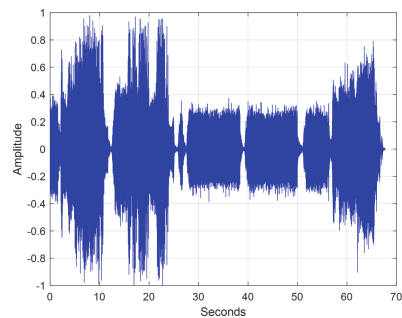


Fig. 14. Audio signal from drone

Figures 17 and 18 present the Mel Frequency Cepstral Coefficients and the Gamma Tone Cepstral Coefficients of the signal for time from 40.8 to 45.3 s.

Detection of drones through analysis of their audio signals can be effectively achieved by using spectral diagrams and Mel Frequency Cepstral Coefficients (MFCCs) as forms

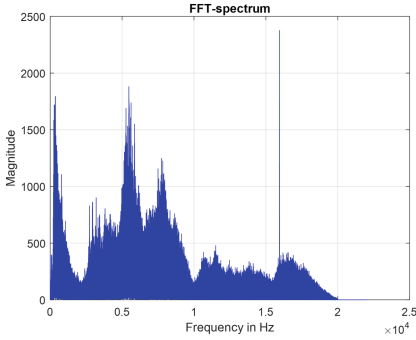


Fig. 15. Signal Spectrum by FFT

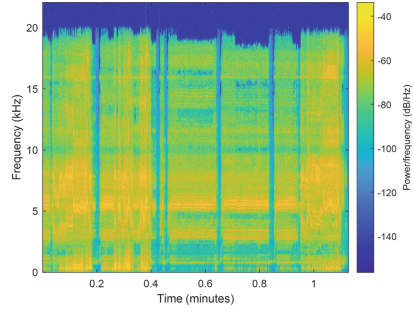


Fig. 16. Spectral Characteristic

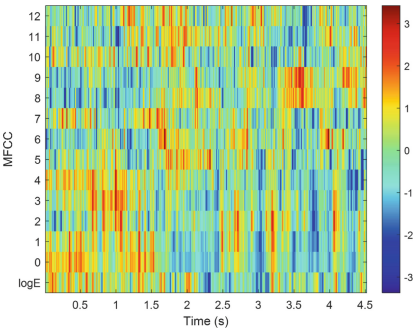


Fig. 17. Mel Frequency Cepstral Coefficients

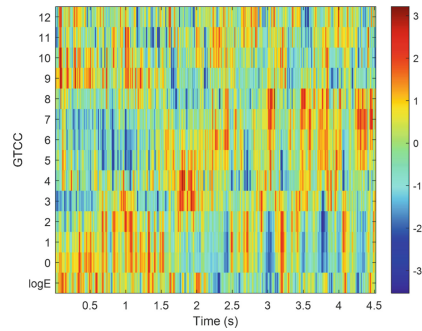


Fig. 18. Gamma Tone Cepstral Coefficients

of visual representations. These visual representations serve as the basis for training models of the YOLO algorithm, which is designed for object recognition in images. Once trained with drone-specific audio-visual data, YOLO neural networks become capable of identifying audio signals from drones. This approach requires converting the audio information into spectral diagrams or images of MFCCs, which can then be analysed by YOLO for efficient and rapid drone recognition based on their audio characteristics.

3.5 UAV Detection and Recognition Technologies Based on Sensor Fusion

Multi-sensor data fusion is the processing of data, and the synergistic combination of information collected from a variety of sensors to provide a better understanding of the process under consideration [33]. The purpose of multi-sensor data fusion is to obtain high-quality detection and recognition of drones in space. The advantage of multi-sensor data processing over single-sensor one is the integration of functionality of different types of sensors in order to improve the performance of the system in terms of precision, range and probability of false alarms. Thanks to the existing methods and algorithms for merging multi-sensor data, as well as the rapid development of digital technologies, many of the drone detection algorithms have been accelerated, and recently artificial intelligence has also been used in the processing processes. Based on data

analysis, Sensor Fusion systems can identify drones in relation to objects of another class (in particular birds), determine the type, its unique characteristics, current dynamic parameters (range, direction, speed, etc.).

A multi-sensor drone detection system combines data from different sensors for detection and classification (discussed earlier in the paper). The algorithm for processing signals and data, as well as their analysis, includes the following stages:

1. Collection of signals and data. Various sensors such as video cameras, infrared cameras, audio sensors, RF sensors and radars collect information about the environment.
2. Signal and data processing. The received signals and data are processed and object characteristics suitable for machine learning are extracted.
3. Data fusion. Data from various sensors are combined to create a comprehensive overview of the surrounding environment and detect potential drones.
4. Classification. Based on the extracted features and data from various sensors, the detected objects are classified as drones or other objects as birds or airplanes.
5. Recognizing the type of drone by its characteristics.
6. Trajectory tracking of the detected objects.

4 Conclusions

The investigated technologies for drone detection possess various advantages and disadvantages, making them applicable for detecting drones with different technical parameters and characteristics. The discussed technologies can find applications in the design and construction of counter-drone systems. Combining these technologies would significantly enhance the process of detecting and recognizing drones. The incorporation of machine learning and artificial intelligence plays a pivotal role in refining these technologies, enabling more accurate and reliable systems. Improving the sensitivity and specificity of detection methods as well as using the power of artificial intelligence to analyse the received data in real time and make an adequate and timely decision will allow the safe integration of drones in urban environments. Continued innovation in the field of drone detection and classification is essential to address the rapidly evolving drone technology as well as the increasing use of drones in practice, assuming the incorporation of context awareness and compliance with regard to relevant public values [34–36], along the lines of applications that are of high societal importance, such as ones supporting resilience against disruptive events [37, 38], for example.

Acknowledgement. This work is supported by the Bulgarian National Science Fund, Project title “Innovative Methods and Algorithms for Detection and Recognition of Moving Objects by Integration of Heterogeneous Data”, KP-06-N 72/4/05.12.2023.

References

1. Hempe, D.: Unmanned aircraft systems in the United States. In: Proceedings of the US/Europe International Safety Conference, Washington, DC, USA, 6–8 June 2006 (2006)

2. Petrescu, R.V.V.: Some aspects of modern drones. *J. Aircraft Spacecraft Technol.* **5**(1), 21–40 (2021). <https://doi.org/10.3844/jastsp.2021.21.40>
3. Commercial UAV market to reach USD15.62 Billion by 2026 – Polaris Market Research (2022)
4. Different types of drones. <https://dronepedia.xyz/5-different-types-of-drones/>
5. Susini, A.: A Technocritical review of drones crash risk probabilistic consequences and its societal acceptance. *Lecture Notes in Information Sciences, LNIS, RIMMA Risk Information Management, Risk Models, and Applications*, vol. 7, pp. 27–38 (2015)
6. Drone Crash Database. <https://dronewars.net/drone-crash>
7. Garvanov, I., Garvanova, M., Tsonkov, G.: Drone detection technologies. *Probl. Eng. Cybern. Robot.* **81**, 29–42 (2024). <https://doi.org/10.7546/PECR.81.24.04>
8. Sawalmeh, A., Othman, N.S., Shakhathreh, H.: Efficient deployment of multi-UAVs in massively crowded events. *Sensors* **18**(11), 3640 (2018). <https://doi.org/10.3390/s18113640>
9. Unmanned Aircraft Systems. <https://www.globalsecurity.org/military/world/uav.htm>
10. Shakhathreh, H., et al.: Unmanned Aerial Vehicles (UAVs): a survey on civil applications and key research challenges. *IEEE Access* **7**, 48572–48634 (2019). <https://doi.org/10.1109/ACCESS.2019.2909530>
11. Mohsan, S.A.H., Khan, M.A., Noor, F., Ullah, I., Alsharif, M.H.: Towards the Unmanned Aerial Vehicles (UAVs): a comprehensive review. *Drones* **6**(6), 147 (2022). <https://doi.org/10.3390/drones6060147>
12. Shishkov, B., Garvanova, G.: A review of pilotless vehicles. In: Shishkov, B., Lazarov, A. (eds.) *Telecommunications and Remote Sensing, ICTRS 2023. Communications in Computer and Information Science*, vol. 1990. Springer, Cham (2023). https://doi.org/10.1007/978-3-031-49263-1_11
13. Riabukha, V.P.: Radar surveillance of unmanned aerial vehicles (review). *Radioelectron. Commun. Syst.* **63**(1), 561–573 (2020). <https://doi.org/10.3103/S0735272720110011>
14. Yang, S., Luo, Y., Miao, W., Ge, C., Sun, W., Luo, C.: RF signal-based UAV detection and mode classification: a joint feature engineering generator and multi-channel deep neural network approach. *Entropy* **23**, 1678 (2021). <https://doi.org/10.3390/e23121678>
15. Hamadi, R., Ghazzai, H., Massoud, Y.: Image-based automated framework for detecting and classifying unmanned aerial vehicles. In: 2023 IEEE International Conference on Smart Mobility, SM 2023, pp. 149–153 (2023). <https://doi.org/10.1109/SM57895.2023.10112531>
16. Mebtouche, N.E.-D., Baha, N.: Robust UAV detection based on saliency cues and magnified features on thermal images. *Multimed. Tools Appl.* **82**(13), 20039–20058 (2022). <https://doi.org/10.1007/s11042-022-14271-3>
17. Tejera-Berengue, D., Zhu-Zhou, F., Utrilla-Manso, M., Gil-Pita, R., Rosa-Zurera, M.: Analysis of distance and environmental impact on UAV acoustic detection. *Electronics (Switzerland)* **13**(3), 643 (2024). <https://doi.org/10.3390/electronics13030643>
18. Lee, H., et al.: CNN-based UAV detection and classification using sensor fusion. *IEEE Access* **11**, 68791–68808 (2023). <https://doi.org/10.1109/ACCESS.2023.3293124>
19. Chesnokov, Y.S., Krutikov, M.V.: Bistatic RCS of aircrafts at the forward scattering. In: *Proceedings of International Radar Conference, Beijing, China*, pp. 156–159 (1996). <https://doi.org/10.1109/ICR.1996.573795>
20. Ezuma, M., Anjinappa, C.K., Funderburk, M., Guvenc, I.: Radar cross section based statistical recognition of UAVs at microwave frequencies. *IEEE Trans. Aerosp. Electron. Syst.* **58**(1), 27–46 (2022). <https://doi.org/10.1109/TAES.2021.3096875>
21. Dhulashia, D., Peters, N., Horne, C., Beasley, P., Ritchie, M.: Multi-frequency radar micro-Doppler based classification of micro-drone payload weigh. *Front. Signal Process.* 22 December 2021, Sec. Radar Signal Processing, vol. 1 (2021). <https://doi.org/10.3389/frsip.2021.781777>

22. Park, D., Lee, S., Park, S., Kwak, N.: Radar-spectrogram-based UAV classification using convolutional neural networks. *Sensors* **21**, 210 (2021). <https://doi.org/10.3390/s21010210>
23. Garvanov, I., Kanev, D., Garvanova, M., Ivanov, V.: Drone detection approach based on radio frequency detector. In: 2023 International Conference Automatics and Informatics (ICAI), Varna, Bulgaria, pp. 230–234 (2023). <https://doi.org/10.1109/ICA158806.2023.10339072>
24. Garvanov, I., Garvanova, M., Ivanov, V., Lazarov, A., Borissova, D., Kostadinov, T.: Detection of unmanned aerial vehicles based on image processing. In: Shishkov, B., Lazarov, A. (eds.) *Telecommunications and Remote Sensing, ICTRS 2022. Communications in Computer and Information Science*, vol. 1730. Springer, Cham (2022). https://doi.org/10.1007/978-3-031-23226-8_3
25. Mahdavi, F., Rajabi, R.: Drone detection using convolutional neural networks. In: 2020 6th Iranian Conference on Signal Processing and Intelligent Systems (ICSPIS), Mashhad, Iran, pp. 1–5 (2020). <https://doi.org/10.1109/ICSPIS51611.2020.9349620>
26. Hammer, M., Borgmann, B., Hebel, M., Arens, M.: Image-based classification of small flying objects detected in LiDAR point clouds. In: *Proceedings of SPIE - The International Society for Optical Engineering*, vol. 11410, p. 1141002 (2020). <https://doi.org/10.1117/12.2557246>
27. Tsonkov, G., Garvanova, G., Borissova, D.: A study on thermal influence on adolescents due to long-term mobile phone exposure. In: Shishkov, B., Lazarov, A. (eds.) *Telecommunications and Remote Sensing, ICTRS 2023. Communications in Computer and Information Science*, vol. 1990. Springer, Cham (2023). https://doi.org/10.1007/978-3-031-49263-1_9
28. Tsonkov, G., Garvanova, M.: Objects detection in an image by color features. In: Shishkov, B., Lazarov, A. (eds.) *Telecommunications and Remote Sensing, ICTRS 2023. Communications in Computer and Information Science*, vol. 1990. Springer, Cham (2023). https://doi.org/10.1007/978-3-031-49263-1_5
29. Garvanov, I., Garvanova, M., Ivanov, V., Chikurtev, D., Chikurteva, A.: Drone detection based on image processing. In: 23rd International Symposium on Electrical Apparatus and Technologies (SIELA), Bourgas, Bulgaria, pp. 1–5 (2024). <https://doi.org/10.1109/SIELA61056.2024.10637850>
30. Garvanov, I., Pergelova, P., Nurdaulet, N.: Acoustic system for the detection and recognition of drones. In: *Telecommunications and Remote Sensing, ICTRS 2023. Communications in Computer and Information Science*, vol. 1990. Springer, Cham (2023). https://doi.org/10.1007/978-3-031-49263-1_8
31. Tejera-Berengue, D., Zhu-Zhou, F., Utrilla-Manso, M., Gil-Pita, R., Rosa-Zurera, M.: Acoustic-based detection of uavs using machine learning: analysis of distance and environmental effects. In: *Proceedings of the 2023 IEEE Sensors Applications Symposium (SAS)*. IEEE, Ottawa, ON, Canada, 18–20 July 2023, pp. 1–6 (2023). <https://doi.org/10.1109/SAS58821.2023.10254127>
32. Kozak, A.V.: Improved unmanned aerial vehicle noise direction finding system. *Electron. Acoust. Eng.* **4**(1), 228902–1 (2021). <https://doi.org/10.20535/2617-0965.eac.228902>
33. Garvanov, I., Garvanova, M., Borissova, D., Vasovic, B., Kanev, D.: Towards IoT-based transport development in smart cities: safety and security aspects. In: Shishkov, B. (ed.) *Business Modeling and Software Design, BMSD 2021. Lecture Notes in Business Information Processing*, vol. 422, pp. 392–398. Springer, Cham (2021). https://doi.org/10.1007/978-3-030-79976-2_27
34. Shishkov, B., van Sinderen, M.: Towards well-founded and richer context-awareness conceptual models. In: Shishkov, B. (ed.) *BMSD 2021. LNBIP*, vol. 422, pp. 118–132. Springer, Cham (2021)
35. Shishkov, B.: Context awareness and external factors. In: Shishkov, B. (eds.) *Business Modeling and Software Design, BMSD 2024. Lecture Notes in Business Information Processing*, vol. 523. Springer, Cham (2024)

36. Shishkov, B., Hristozov, S., Janssen, M., Van den Hoven, J.: Drones in land border missions: benefits and accountability concerns. In: Proceedings of the 6th International Conference on Telecommunications and Remote Sensing (ICTRS 2017). ACM, New York (2017)
37. Shishkov, B., Hristozov, S., Verbraeck, A.: Improving resilience using drones for effective monitoring after disruptive events. In: Proceedings of the 9th International Conference on Telecommunications and Remote Sensing (ICTRS 2020). Association for Computing Machinery, New York (2020)
38. Shishkov, B., Verbraeck, A.: Making enterprise information systems resilient against disruptive events: a conceptual view. In: Shishkov, B. (eds.) Business Modeling and Software Design, BMSD 2020. Lecture Notes in Business Information Processing, vol. 391. Springer, Cham (2020)



Digital System for Registering Emergency Events in Electric Vehicles

Radoslav Simionov^(✉), Kristian Lodkadhiev, Radostin Dolchinkov,
Kamen Seymenliyski, and Silvia Letskovska

Faculty of Computer Science and Engineering, Burgas Free University, Burgas, Bulgaria
radoslav.simionov@gmail.com, {rado,kdimitrov,silvia}@bfu.bg

Abstract. In the context of the rapidly developing electric vehicle market, the integration of telematics monitoring systems represents an important engineering approach to increase the efficiency and safety of these means of transport. The present study analyzes the impact of these systems, which are key to optimizing the performance and sustainability of electric vehicles. Telematics systems, built on the basis of advanced sensor technologies and modern communication solutions, allow detailed collection and analysis of operational data in real time, including parameters such as battery status, energy consumption and the general technical condition of the vehicle.

By using these systems, engineers and operators can perform timely diagnostics and maintenance, which contributes to improving the reliability and long-term operation of electric vehicles. In addition, these systems provide valuable information about driving patterns, leading to optimized mileage use and increased energy efficiency. Last but not least, telematics systems play a significant role in increasing driving safety by offering means of remote monitoring and signaling of potential problems. Within this engineering perspective, the present study highlights the importance of telematics systems as fundamental components for modern electric vehicles, which are essential for manufacturers and operators in their pursuit of functionality optimization and environmental sustainability.

Keywords: Telematics · Electric Vehicles · Energy Efficiency · Operational Data Analysis · Vehicle Safety

1 Introduction

As the automotive industry transitions toward sustainable mobility solutions, the widespread adoption of electric vehicles (EVs) brings about new challenges and opportunities. Ensuring the safety of occupants and responding effectively to accidents remains paramount. The analyzed scientific publications do not present comprehensive concepts for the monitoring and safety of electric vehicles, similar to other transport systems applied in air and maritime transport [1–3]. In light of this, the purpose of this report is to comprehensively introduce and analyze the Digital Accident Recording System (DARS) implemented in electric vehicles.

2 Background

Electric vehicles have gained substantial popularity due to their eco-friendly nature, reduced emissions, and advancements in battery technology. However, with the increasing presence of EVs on the roads, addressing safety concerns becomes imperative. Accidents involving electric vehicles demand innovative solutions for accident recording and post-incident analysis. The Digital Accident Recording System serves as a critical component in enhancing the safety landscape of electric mobility.

3 Target of the Report

This report aims to shed light on the functionalities, capabilities and safety impact of a digital EV accident recording system in the context of electric vehicles. Also, to present his own concept of such a system. As the automotive industry embraces digitization and connectivity, the integration of advanced safety systems becomes essential [4]. DARS not only records important data during incidents, but also facilitates a more holistic understanding of incidents, contributing to ongoing efforts to improve vehicle safety standards.

4 Scope and Objectives

The scope of this report encompasses a detailed examination of the components, features, and operational aspects of the Digital Accident Recording System. Key objectives include:

- Presenting an overview of the DARS and its role in recording accident-related data;
- Exploring the integration of the system with various vehicle components and sensors;
- Analyzing the communication mechanisms employed for transmitting accident information;
- Examining the benefits and potential impact of the DARS on post-accident analysis and overall vehicle safety;
- Addressing challenges and considerations associated with the implementation of DARS in electric vehicles;
- Discussing future developments and innovations in accident recording systems for EVs.

Through this report, we aim to provide stakeholders, including automotive manufacturers, regulatory bodies, and the general public, with a comprehensive understanding of the Digital Accident Recording System and its significance in promoting safety within the evolving landscape of electric mobility [5].

5 Presenting an Overview of the DARS and Its Role in Recording Accident-Related Data

DARS serves as a critical safety feature by recording and analyzing data during accidents, enabling a better understanding of the event's dynamics.

The system captures detailed information about the accident, aiding in post-accident investigations, insurance claims, and legal proceedings.

Data collected by DARS contributes to the enhancement of vehicle design, making electric vehicles safer through continuous improvement based on real-world incidents.

A. Components of Digital Accident Recording System:

- Collision Detection Sensors - Utilizes advanced sensors such as radar, lidar, and cameras to detect and analyze collisions with precision;
- Vehicle Control Unit (VCU) - The VCU plays a crucial role in integrating real-time vehicle data with the DARS, ensuring accurate recording during accidents;
- GPS and Location Sensors - Provides geospatial information, aiding in accurate accident location tracking and analysis;
- In-Vehicle Cameras - Captures visual data before, during, and after an accident, offering valuable insights into the sequence of events;
- Energy Management System (EMS) - Integrates EMS data to understand the impact of accidents on the electric vehicle's energy system, optimizing safety measures.

DARS has an outstanding role in recording accident data. DARS works in real time, inputting important data about the time of the accident, including the force of the impact, the location and the condition of the vehicle. Accurately timing events helps reconstruct the sequence of the incident, helping investigators understand the dynamics leading up to the incident. DARS preserves secure accident-related data, facilitating easy retrieval for post-accident analysis, insurance claims and legal proceedings. Some DARS systems are equipped to communicate with emergency services, providing an immediate assistance basis for recording incident data.

B. Benefits of DARS for Electric Vehicles:

- Improved Safety Standards - DARS contributes to raising safety standards in the electric vehicle industry, promoting a safer driving experience;
- Enhanced Post-Accident Analysis - Enables more accurate and efficient post-accident analysis, benefiting insurance companies, law enforcement, and vehicle manufacturers;
- Continuous Improvement - Data collected by DARS supports continuous improvement in vehicle design and safety features, contributing to the overall advancement of electric vehicles.

6 Analyzing the Communication Mechanisms Employed for Transmitting Accident Information

The effective transmission of accident information is crucial for the successful functioning of Digital Accident Recording Systems (DARS) in Electric Vehicles (EVs). This report provides a comprehensive analysis of the communication mechanisms employed for transmitting accident information from DARS in EVs, exploring the technologies, protocols, and challenges associated with ensuring timely and accurate data transfer.

There are several important points that the system needs to ensure in a reliable way:

A. *Communication Technologies:*

- Cellular Networks - Examination of DARS integration with cellular networks for real-time data transmission. Evaluation of 4G and 5G technologies and their impact on data transfer speed and reliability;
- V2X Communication - Exploration of Vehicle-to-Everything (V2X) communication for peer-to-peer data exchange. Benefits and challenges associated with V2X communication in the context of DARS;
- Dedicated Short-Range Communication (DSRC) - Analysis of DSRC as a dedicated communication channel for DARS in EVs. Consideration of interoperability and spectrum allocation issues.

B. *Communication Protocols:*

- Standardization Efforts - Overview of existing communication protocols relevant to DARS in EVs. Discussion on standardization efforts to ensure compatibility across different manufacturers;
- Data Encryption and Security - Examination of encryption protocols employed to secure accident information during transmission. Addressing cybersecurity concerns and ensuring the integrity of transmitted data.

C. *Real-time Data Transmission Challenges:*

- Bandwidth Limitations - Analysis of bandwidth challenges and their impact on real-time data transmission. Strategies to optimize data size without compromising critical information;
- Latency Issues - Discussion on the importance of low latency in transmitting accident information. Technological advancements and protocols to minimize communication delays.

D. *Cloud Integration:*

- Cloud-Based Data Storage - Exploration of cloud integration for storing and retrieving accident information. Consideration of data privacy, accessibility, and scalability;
- Over-the-Air (OTA) Updates- Analysis of Over-the-Air updates for communication protocols and DARS software. Balancing the need for continuous improvement with potential security risks.

7 Similar Systems, that Has Already Been Realized

• Tesla Autopilot:

Tesla's Autopilot is an advanced driver assistance system that includes features such as adaptive cruise control, lane-keeping assistance, and automatic emergency braking. While not explicitly marketed as a DARS, Tesla vehicles are equipped with a comprehensive suite of sensors and cameras that record data before, during, and after accidents. This data can be used for post-accident analysis.

• GM OnStar:

General Motors' OnStar system provides a range of services, including automatic crash response. In the event of an accident, OnStar can automatically connect with emergency services and provide them with critical information such as the vehicle's location and severity of the impact.

- **BMW ConnectedDrive:**

BMW's ConnectedDrive system offers various driver assistance features and services. In the event of an accident, the system can automatically initiate an emergency call to the BMW call center, providing details about the vehicle's location and the severity of the collision.

- **Volvo On Call:**

Volvo's On Call system includes features such as automatic collision notification and emergency assistance. In the event of a crash, the system can automatically call for help and provide the emergency services with crucial information, including the vehicle's location.

- **Audi Pre Sense:**

Audi's Pre Sense is a safety system that can help mitigate the consequences of an accident. It can initiate preventive measures, such as tensioning seatbelts and closing windows, in anticipation of a collision. Post-collision, the system can automatically contact emergency services.

- **Subaru Eye Sight:**

Subaru's Eye Sight is an ADAS that includes features like pre-collision braking and adaptive cruise control. While not explicitly marketed as a DARS, it can contribute to accident prevention and provide data for post-accident analysis.

- **Toyota Safety Sense:**

Toyota's Safety Sense suite includes various safety features like pre-collision systems and lane departure alert. In the event of a collision, the system can provide data for post-accident analysis.

8 Structure of the Digital Accident Recording System (DARS) for Evs

A Digital Accident Recording System (DARS) for electric vehicles involves various hardware and software components that work together to capture, process, and store data related to accidents [6].

Here are the main constituent components of such a system:

A. Onboard Cameras and Sensors:

Description: Cameras and sensors mounted on the electric vehicle to capture visual and environmental data.

Functions:

- Recording images and videos of the surroundings.;
- Collecting data on speed, acceleration, and environmental conditions.

B. Telematics Unit:

Description: In-vehicle device that collects and transmits real-time data about the vehicle's performance.

Functions:

- Monitoring battery status.
- Transmitting data related to vehicle speed, location, and system status.

C. *GPS Module:*

Description: Global Positioning System module that determines the vehicle's precise location.

Functions:

- Providing accurate location data for accident recording and analysis.

D. *Accelerometers and Gyroscopes:*

Description: Motion sensors that measure acceleration and rotation.

Functions:

- Capturing data on the vehicle's movement during an accident.

E. *Collision Detection Sensors:*

Description: Sensors designed to detect and measure the impact forces during a collision.

Functions:

- Providing crucial data for understanding the severity of accidents.

F. *Communication Module:*

Description: Enables communication between the vehicle and external systems, such as emergency services or the DARS server.

Functions:

- Facilitating real-time communication for emergency notifications;
- Transmitting accident data to the DARS server.

G. *Control Unit:*

Description: Central processing unit responsible for managing and coordinating the various hardware components.

Functions:

- Processing data from sensors and cameras;
- Controlling the overall functionality of the DARS.

H. *Storage Devices:*

Description: Devices for storing data captured during accidents and related information.

Functions:

- Storing images, videos, and sensor data for post-accident analysis;
- Managing databases of accident records.

I. *Display Unit:*

Description: Interface for providing information to the driver or occupants.

Functions:

- Displaying relevant accident information;
- Communicating emergency instructions.

J. Power Supply System:

Description: Ensures continuous power to the DARS components.

Functions:

- Providing power to sensors, telematics, and other electronic components.

K. Authentication and Security Hardware:

Description: Hardware components dedicated to ensuring the security and integrity of the system.

Functions:

- Implementing secure access controls;
- Authenticating users and external systems.

These hardware components collectively form the infrastructure of a digital accident recording system for electric vehicles. The integration and coordination of these components enable the system to capture and manage data effectively for accident recording and analysis [7] (Fig. 1).

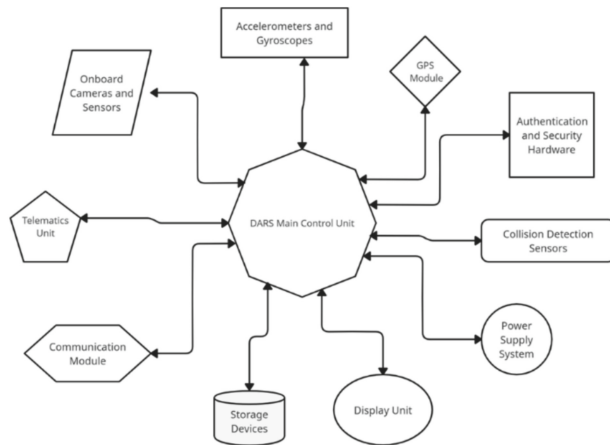


Fig. 1. Structural UML Diagram of DARS System for EV's

The typology of the system is Star type.

The normal operation of the DARS EV's is ensured through the main module.

It communicates with the entire periphery of the DARS EV's, processes the information and according to certain set algorithms, performs the controlling of the system.

Certain information is sent to the Communication Module, which communicates with the Server.

When receiving controlling information from the Server, the main module receives these commands from the Communication module and performs the corresponding function.

9 Structure of the Cloud Platform for Digital Accident Recording System (DARS) for Evs

A. *DARS System:*

Description: All entire DARS System's components.

Functions:

- Processing, segmentation, analysis of information, given of it's components;
- Feed this information to the communication module.

B. *EV's DARS Communications Module:*

Description: A hardware module that provides the interconnection between the EV's DARS System and the entire Cloud infrastructure.

Functions:

- Getting processed information from the system;
- Establishing a communication channel with the Cloud system;
- Exchange of information with the Cloud system.

C. *EV DARS Server (REST API)*

Description: This is the main server that receives, analyzes, segments and stores the information received from the EV's DARS System.

Functions:

- Processing, segmentation, analysis of information, received from EV's DARS Communication Module;
- Interaction with the database;
- Two-way connection with the communication module of the EV's DARS System, which allows control of certain processes in the system, as well as OTA (Over-The-Air Update);
- It provides the connection to monitoring and control panels integrated into Web and mobile applications.

D. *EV DARS Server Database*

Description: Database, SQL type, which stores the information received from the DARS system.

Functions:

- Data analysis;
- Data segmentation;
- Data storage.

E. *EV DARS Web and Mobile Dashboard Applications*

Description: These are control panels integrated as web and mobile applications that allow remote monitoring and control of the entire EV's DARS system.

Functions:

- Providing the final analyzed data;
- Control of actions and processes integrated into the system;
- Process monitoring;

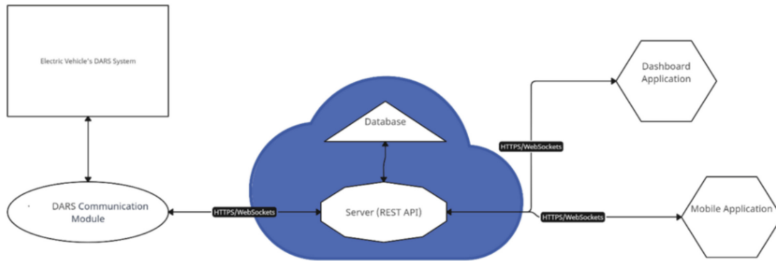


Fig. 2. Structural UML diagram of the Cloud Platform for Digital Accident Recording System (DARS) for EVs

- Notification to users and system operators (Fig. 2).

The way the cloud infrastructure works is as follows:

The Server communicates bi-directionally with the communication module, via Web Sockets.

The server receives the data sent by the communication module. Then, analyze and process the data. Part of them is stored in the Database.

The Web and mobile applications, on the other hand, communicate bi-directionally with the Server, again over Web Sockets. They receive data, notifications and other necessary information from the Server [8, 9].

In case the user activates controlling from the Web or Mobile applications, the Server processes these requests and transmits the necessary commands to the DARS Communication module.

10 Recommendations

In light of the analysis and findings presented in this report on Digital Accident Recording Systems (DARS) for Electric Vehicles, several key recommendations emerge, aimed at optimizing the implementation and impact of these systems:

A. Continuous Technological Advancements:

Encourage ongoing research and development to stay abreast of emerging technologies. Regular updates to DARS components and software will ensure compatibility with the latest advancements in electric vehicle systems, sensors, and communication technologies.

B. Standardization and Interoperability:

Advocate for industry-wide standards to ensure interoperability between different manufacturers' DARS and vehicle systems. This will enhance data consistency, simplify integration, and facilitate a more comprehensive approach to post-accident analysis.

C. Enhanced User Education and Training:

Develop comprehensive training programs for electric vehicle users to familiarize them with the functionalities of the DARS. Educating drivers on the importance of DARS, emergency notification procedures, and the overall safety benefits will maximize the system's effectiveness.

D. *Privacy and Data Security Measures:*

Prioritize the implementation of robust privacy and data security measures to safeguard sensitive information captured by DARS. Ensuring compliance with data protection regulations will foster user trust and confidence in the system.

E. *Collaboration with Emergency Services:*

Establish collaborative partnerships with emergency services to streamline the integration of DARS with existing emergency response systems. This collaboration can lead to quicker response times, enhanced situational awareness, and improved outcomes in post-accident scenarios.

F. *Adaptive Driver Assistance Features:*

Explore opportunities to enhance DARS by integrating adaptive driver assistance features. This includes real-time feedback to drivers on their driving behavior, promoting safer practices and potentially preventing accidents.

G. *Global Regulatory Frameworks:*

Advocate for the development of global or standardized regulatory frameworks governing the implementation of DARS in electric vehicles. This will create a consistent regulatory landscape, facilitating widespread adoption and ensuring a uniform approach to safety standards.

H. *Incorporate AI and Machine Learning:*

Investigate the integration of artificial intelligence (AI) and machine learning algorithms into DARS. These technologies can contribute to more sophisticated accident analysis, predictive modeling, and continuous improvement of the system's capabilities.

I. *Public Awareness Campaigns:*

Launch targeted public awareness campaigns to inform the general public about the presence and benefits of DARS in electric vehicles. Increased awareness can lead to greater acceptance, usage, and adherence to safety protocols associated with these systems.

J. *Long-Term Maintenance and Support:*

Develop long-term maintenance and support strategies for DARS components. Regular software updates, maintenance checks, and user support will extend the lifespan of the system and ensure its continued effectiveness.

Implementing these recommendations will contribute to the successful integration and sustained impact of Digital Accident Recording Systems for Electric Vehicles, fostering safer road environments and advancing the evolution of electric mobility [10].

11 Conclusions

In conclusion, the development and implementation of a Digital Accident Recording System (DARS) for Electric Vehicles represent a significant stride towards enhancing vehicle safety, post-accident analysis, and overall user experience. This advanced system leverages a combination of hardware components, such as onboard cameras, telematics units, and sensors, along with sophisticated software modules like accident management and reporting systems.

The integration of DARS in electric vehicles not only facilitates the recording and documentation of accidents but also plays a pivotal role in proactive safety measures. The system's ability to capture real-time data, including vehicle speed, location, and impact forces, provides a valuable resource for post-accident analysis, aiding in understanding the sequence of events and identifying contributing factors.

Moreover, the telematics unit's continuous monitoring of battery status and system health contributes to the overall reliability and performance of electric vehicles. The seamless integration of DARS with other vehicle systems, such as GPS modules and collision detection sensors, further enhances the system's accuracy and effectiveness in recording and analyzing accidents.

As we navigate the transition to electric mobility, the implementation of a robust DARS not only aligns with the evolving safety standards but also addresses the unique considerations of electric vehicles. The availability of comprehensive accident data, coupled with immediate notifications to emergency services, underscores the potential lifesaving impact of this technology.

In conclusion, the Digital Accident Recording System for Electric Vehicles stands as a testament to the continual advancements in automotive safety technology. By providing a thorough and integrated approach to accident recording and analysis, this system contributes to the broader goals of improving road safety, mitigating accident severity, and fostering public confidence in the adoption of electric vehicles. As technology continues to evolve, DARS remains at the forefront of innovations aimed at creating safer, more efficient, and sustainable transportation ecosystems.

References

1. Bauder, M., Kubjatko, T., Schweiger, H.-G.: Development of an Accident Reconstruction Method Using Cooperative Awareness Message Data (2024)
2. Harris, L.: Telematics and Big Data: Revolutionizing Fleet Management in the Automotive Industry (2024)
3. Sahoo, P., Singh, S., Prasad, K.: Big Data Analytics (Telematics) for Real-Time Testing Improvements and Integration Back to the Development of Future Models/EVs (2024). <https://doi.org/10.4271/2024-26-0352>
4. Dolchinkov, R., Seimenliyski, K., Popov, I.: Electric vehicle safety. In: Collection of reports from the International Scientific Conference "Black Sea - Doors and Many Bridges", Burgas, ed. BFU, pp. 533–540 (2022). ISBN 978-619-253-017-4
5. Dolchinkov, R., Seimenliyski, K., Popov, I.: Incidents with electric vehicles on ignition in a road transport accident. In: Collection of reports from the International Scientific Conference "Black Sea - Doors and Many Bridges", Burgas, ed. BFU, pp. 541–548 (2022). ISBN 978-619-253-017-4
6. Dolchinkov, R., Seimenliyski, K., Popov, I.: Methodology for the actions of the fire department in the event of an electric vehicle incident. In: Collection of reports from the International Scientific Conference "Black Sea - Doors and Many Bridges", Burgas, ed. BFU, pp. 604–610 (2022). ISBN 978-619-253-017-4
7. Ventsislavov, K., Seimenliyski, K., Letskovska, S., Mollova, S.: Algorithm for electric vehicle telematic monitoring. In: Collection of reports from the International Scientific Conference "Black Sea - Doors and Many Bridges", Burgas, ed. BFU, pp. 633–637 (2022). ISBN 978-619-253-017-4

8. Sandaka, B.P., Kumar, J.: Alternative vehicular fuels for environmental decarbonization: a critical review of challenges in using electricity, hydrogen, and biofuels as a sustainable vehicular fuel. *Chem. Eng. J. Adv.* **14**, 100442 (2023). <https://doi.org/10.1016/j.cej.2022.100442>. ISSN 2666-8211
9. Đorđević, B., Mitić, S.: The possibility of traffic accident reconstruction using event data Recorders: a review. *Industrija* **49**, 99–115 (2021). <https://doi.org/10.5937/industrija49-35974>
10. Matsankov, M., Ivanova, M.: Selection of optimal variant of hybrid system under conditions of uncertainty. In: *The 2nd International Conference on Electrical Engineering and Green Energy* Roma, Italy, 28–30 June (2019)



Modern Technological Solutions for Passive Buildings and Buildings with Zero Energy Consumption

Kamen Seymenliyski^(✉), Atanas Yovkov, Eldar Zaerov, Velizar Todorov, Radoslav Simionov, and Hristo Mihaylov

Faculty of Computer Science and Engineering, Burgas Free University, Burgas, Bulgaria
kdimitrov@bfu.bg

Abstract. In the developed world, global warming represents a significant challenge, confronting humanity with the need for urgent and effective measures to reduce carbon emissions and sustainable use of resources.

In the existing scientific articles on the issue, there is a lack of data from specific studies on the possible technological solutions in various climatic and geographical regions. It is necessary to specify the technical parameters and the corresponding engineering solutions to improve energy efficiency and reduce carbon emissions.

It is particularly important to pay attention to the building sector, which currently consumes more energy than any other area. In order to mitigate climate change and achieve sustainability in the urban environment, it is essential to reduce the energy consumption of buildings. In the context of mass urbanization, especially in developing countries, where rapid urban growth exacerbates energy challenges, there is a growing need to develop effective strategies.

This report proposes a solution to reduce energy consumption in residential buildings, leading to their designation as near-zero consumption buildings.

Given the global scale of climate change and resource scarcity, improving global energy efficiency is becoming increasingly important.

The European Union (EU) directive on the energy performance of buildings requires the renovation of at least 3% of the total built-up area of buildings and near-zero energy buildings. (nZEB) in all EU Member States by 2027.

Some of the problems caused by these transformations are analyzed in this report.

Keywords: Near-Zero Energy Buildings (nZEB) · Building Sector Energy Consumption · Transformation Challenges in Building Sector · Energy Efficiency in Buildings · digital technologies · passive buildings

1 Introduction

Among the many standards for energy efficient buildings in Europe, the most common are Effinergie, Minergie and Passivhaus.

The construction of houses according to these standards costs 5–15% more than the construction of conventional buildings, but they are preferred because they allow the owners to significantly save electricity [1–3].

- Effinergie is a standard for energy efficient homes created in France. The Effinergie association was established in 2006. This standard includes three main labels:
- BBC-Effinergie: construction of low-energy houses (Bâtiments Basse Consommation, BBC); energy consumption - no more than 50 kWh/m² per year;
- Effinergie Rénovation: reconstruction of buildings; energy consumption - up to 80 kWh/m² per year;
- Effinergie+: the improved airtightness of the building reduces consumption by up to 40 kWh/m² per year.

In November 2013, the first house according to the Bepos-Effinergie standard was built in Western France. The house does not consume energy, but produces it (consumption is 122 kWh/m² per year). For this reason, such buildings are called “active”.

1.1 The Passive House

A building designed according to strict energy efficiency criteria aimed at minimizing energy needs for heating and cooling. The basic concept behind the passive house involves optimization of heat gains and minimization of heat losses, which is achieved through highly efficient thermal insulation, passive solar accumulation and strategic planning of ventilation systems. Thus, traditional heating and cooling systems become redundant or are used to a very limited extent. Designing a passive house involves careful consideration of location, orientation, local climate conditions and available energy resources to ensure optimal use of passive energy sources.

1.2 The Zero-Energy Home

Evolution of the passive house, achieving a balance between energy consumption and production on an annual basis. Such homes are characterized by extremely low energy demand and high comfort, realized through the integration of passive and active energy strategies. Key aspects in the construction of zero-energy homes include:

- Optimized thermal insulation: Special attention is paid to the insulation of the roof and facade, and in cold climates the thickness of the insulation can reach up to 30 cm.
- Ventilation system with heat recovery: The warm air from the interior rooms passes through a heat exchanger, where it transfers its energy to the incoming fresh air.
- Energy-efficient appliances: The use of low-energy appliances is a standard for reducing overall energy consumption.
- Integration of renewable energy sources: Solar panels and heat pumps are most often used, striving for maximum efficient use of energy generated on site.

These elements combine to create homes that not only minimize their energy needs, but also actively produce energy, contributing to the concept of sustainable housing.

The heating system works on renewable energy sources (solar and wind energy). The coefficient of thermal conductivity of walls, roofs and floors should not be less than 0.2 W/m² K, of windows - 1.3 W/m² K. Energy consumption for new houses should not exceed 38 kWh/m² annually, for reconstructed homes - 60 kWh/m².

The passive house standard (Passivhaus) was developed in the early 1990s in the German city of Darmstadt [4, 5].

The Passive House Institute (PHI) was founded in 1996 by the creator of the concept, Professor Wolfgang Feist. Based in Darmstadt, Germany, the institute has developed the passive house standard based on extensive research and monitoring of thousands of passive house projects.

European projects such as CEPHEUS (Cost Efficient Passive Houses as European Standards) and PEP (Promotion of European Passive Houses) were launched to assess the potential of the passive house standard in terms of ensuring of affordable low-energy homes, as a standard applicable across Europe. These projects were very successful and played a big role in the development of the passive house [7, 8].

- Criteria and main features for a passive house

A building designed to the Passive House standard must provide excellent indoor air quality with reduced indoor pollutants and a constant flow of fresh air, reduced maintenance and operating costs, as well as drastically reduced energy consumption and CO₂ emissions.

Data on CO₂ emissions and energy use per year for the different house types are shown in Fig. 1.

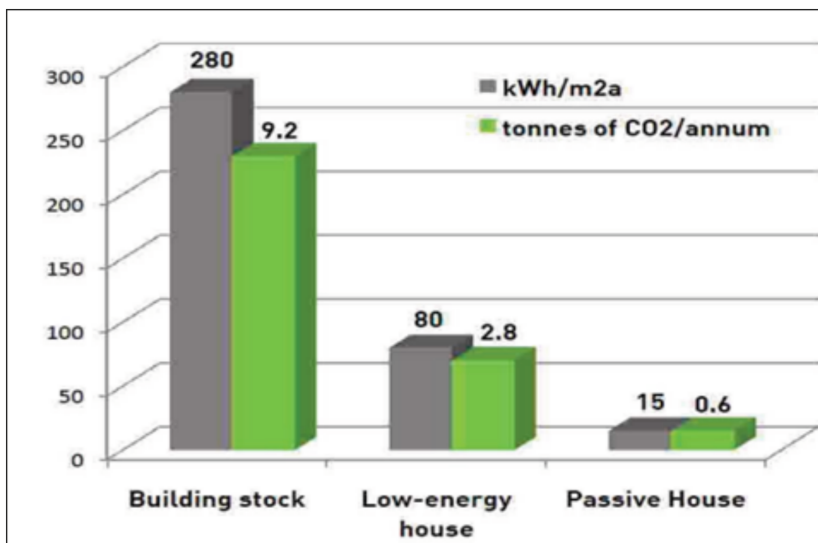


Fig. 1. CO₂ emissions and energy used/year for different types of houses. SOURCE: <https://www.passivehouse-international.org>

An A-rated house is a low-energy house (BER methodology). A “passive” house is a house designed to have a heat consumption that is as low as is practically achievable; A Low Carbon or Zero Carbon House is a house that is responsible for little or no carbon emissions [10, 11].

The main criteria for building a passive house are:

- Space heating requirement $\leq 15 \text{ kWh}/(\text{m}^2)$;
- Heating load of the building $\leq 10 \text{ W}/\text{m}^2$;
- Useful cooling demand $\leq 15 \text{ kWh}/(\text{m}^2)$;
- Primary energy consumption $\leq 120 \text{ kWh}/(\text{m}^2)$;
- Hermeticity of the building $\leq 0.6 \text{ ac}/\text{h}^{-1}$;
- Frequency of overheating $\leq 10\%$.

In the construction of passive houses, five basic principles are applied (Fig. 2), which guarantee high energy efficiency and living comfort. These principles are:

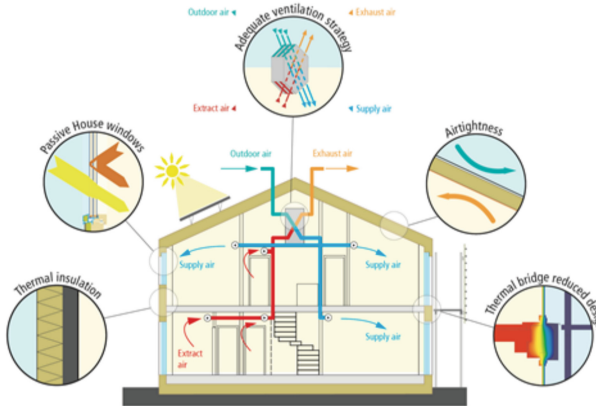


Fig. 2. Five basic requirements in the construction of passive houses. SOURCE: <https://www.chaertertonhomes.co.nz>

- **Thermal insulation:** All non-transparent components of the outer shell of the house are extremely well insulated. This is achieved by using materials with a low heat transfer coefficient (U-value), with a maximum of $0.15 \text{ W}/(\text{m}^2\text{K})$ recommended for cool and temperate climates.
- **Passive house windows:** Windows are equipped with well-insulated frames and low-emissivity glasses filled with argon or krypton to minimize heat loss. The recommended U-value for windows is $0.80 \text{ W}/(\text{m}^2\text{K})$ or less, with g-values around 50%.
- **Heat recovery ventilation:** Heat recovery ventilation systems are key to maintaining good air quality and energy efficiency. In passive houses, at least 75% of the heat from the exhaust air is required to be transferred back to the fresh air through a heat exchanger.
- **Airtightness of the building:** To avoid uncontrolled air leakage, the building must be hermetically sealed. Requirements include air leakage that is less than 0.6 of the building's total volume per hour under a 50 Pa pressure test.
- **Absence of thermal bridges:** In design and construction, it is important to avoid thermal bridges, which can lead to heat loss. This is achieved by using special insulation materials and techniques that interrupt heat conduction paths and provide continuous thermal insulation.

These principles are fundamental to the design and construction of passive houses and contribute to their high energy efficiency and comfort [12, 13].

Since 2019, strict standards have been imposed on the construction of buildings in Europe, requiring them to meet the criteria for passive houses or even have higher indicators - houses with zero or plus energy. These buildings do not differ significantly from passive ones in terms of architecture and construction principles, but have an increased volume and power of engineering equipment based on alternative energy sources.

The Passive House Planning Tool (PHPP) developed by the Passive House Institute (PHI) is used to verify compliance with Passive House standards. PHPP allows accurate planning and calculation of energy performance of buildings, while offering sub-criteria to facilitate the certification process [14, 15].

According to the 2010 Energy Performance of Buildings Directive (EPBD), from the end of 2020 all new buildings in the EU must be constructed as nearly zero-energy buildings (nZEBs), and all new public buildings must meet of the nZEB standard from the end of 2018.

Various technologies and materials are used to achieve near-zero or zero energy consumption, including photovoltaic cells, heat pumps, ventilation systems with heat recovery, advanced insulation materials, triple-glazed windows and home engineering automation systems.

In December 2021, the Commission proposed a revision of the EPBD, taking a step forward from nZEB to zero-emission buildings (ZEB), with the aim of achieving the long-term goal of climate neutrality and implementing the energy efficiency first principle. The proposal includes a requirement to calculate and disclose the life cycle Global Warming Potential (GWP) of buildings.

By 2050, it is expected that the entire building stock in Europe will be reduced to near-zero energy efficiency standards, which requires accelerating the pace of energy renovation of buildings. The European Commission monitors member states' progress and requires them to draw up road maps for the decarbonization of the real estate sector, setting interim targets for 2030 and long-term strategies to renew the building stock until 2050.

2 Types of Ecological Materials for Building Passive and Energy-Efficient Houses

For the autonomous functioning of individual residential buildings, the use of energy-saving technologies in combination with ecological building materials is essential. The choice of suitable materials and technologies depends on the specifics of the construction site and the climatic conditions of the area. Some of the most effective materials and technologies include:

2.1 For Load-Bearing Structures

- Bricks and ceramic tiles: Traditional and widely used building materials;

- Wooden constructions: They provide good ventilation and have a low coefficient of thermal conductivity;
- Autoclaved aerated concrete: Light and insulating material suitable for energy efficient construction.

2.2 For Insulation

- Eco-friendly: Ecologically clean material without volatile substances;
- Foam glass: Waterproof, moisture-resistant, fire-resistant and non-flammable material with high strength and durability;
- Insulating boards of wood origin: They allow the material to “breathe”, suitable for insulating roofs and walls;
- Ballast insulation: Provides good sound insulation and meets fire safety requirements.

2.3 For Roofing Materials

- Ceramic tiles: They offer high noise insulation, frost resistance and low thermal conductivity.
- Metal roof tiles: Environmentally friendly, wear-resistant, do not melt or burn at high temperatures.
- Flexible bitumen roof tiles: Environmentally friendly, made of fiberglass impregnated with modified bitumen.

2.4 For Floor Coverings

- Parquet and parquet boards: Natural and sustainable materials.
- Cork cover: Eco-friendly and comfortable for the feet.
- Carpets: Warm and comfortable, they can be made from environmentally friendly materials.
- Ceramic tiles: Durable and easy to maintain.

2.5 Additional Technologies

- Wastewater heat recovery systems: Enable the re-use of waste water heat.
- Water purification and reuse systems: Reduce the need for water resources.
- Use of renewable energy sources: Photovoltaic cells, heat pumps, wind turbines and other technologies for the production of energy from renewable sources.

Integrating these materials and technologies into the construction process can significantly improve the energy efficiency of residential buildings and reduce their operating costs while reducing environmental impact [16, 17].

The study of the single-family residential building in Smolyan, Bulgaria presents an interesting case for analyzing energy efficiency and potential improvements in the context of the specific climate of the region. The following aspects are key:

Climatic conditions: Smolyan is located in a climate zone characterized by cold winters and cool summers. This imposes high requirements on the energy efficiency of buildings, especially in terms of heating during the winter months.

Building construction: The building is monolithic, with solid brick walls, which however do not offer optimal energy efficiency. The lack of external thermal insulation significantly increases the risk of heat loss, especially in the context of the region's cold climate.

Thermal insulation and joinery: Thermal insulation has been laid on the top floor, which is a positive step towards improving energy efficiency. Replaced windows with good insulating qualities also contribute to reducing heat losses [18, 19].

Heating system: The use of solid fuel water boilers and a combined coil boiler to heat domestic hot water is typical for the region, but may not be the most efficient solution in terms of energy efficiency and environmental friendliness.

2.6 Potential for Improvements

- **Thermal insulation:** Improving the thermal insulation of external walls would lead to a significant reduction in heat loss and lower heating costs.
- **Energy-efficient heating systems:** Switching to more efficient heating systems, such as heat pumps or solar systems, can reduce dependence on solid fuel and improve the overall energy efficiency of the building.
- **Ventilation systems with heat recovery:** The installation of such systems would improve indoor air quality and reduce energy losses related to ventilation.

Class	EPmin, kWh/m ²	EPmax, kWh/m ²	RESIDENTIAL BUILDINGS
A+	-	48	A+
A	48	95	A
B	96	190	B
C	191	240	C
D	241	290	D
E	291	363	E
F	364	435	F
G	-	435	G

Fig. 3. Energy efficiency classes

As of 01.11.2018, the energy costs for one calendar year are as follows: for heating - 13800 kWh; for DHW - 3240 kWh; for household needs - 11376 kWh.

Energy consumption for one year 186.21 kWh/m².

With these data, the home falls into energy class "B" according to energy efficiency criteria (Fig. 3).

To reduce the consumption of electrical energy, at the end of 2018, a solar installation for domestic hot water (DHW) was installed on the roof of the building (Fig. 4).

This leads to a drop in electricity consumption by 1150 kW per year, the effect being mainly in the summer months. The disadvantages of the solar installation are high operating costs and complex maintenance.



Fig. 4. Photovoltaic power plant (PEC).

The next step to achieve higher energy efficiency is the construction of a 2.2 kW photovoltaic power plant.

The studied energy system includes the following components): 1 - photovoltaic panels; 2 - hybrid inverter; 3 - intelligent controller for managing energy flows; 4 - operating panel; 5 - heating radiator; 6 - household energy consumers; 7 - pellet boiler; 8 – heat exchanger.

The following conclusions can be drawn from the measurements and research of the home:

- After installation of the solar domestic hot water system in 2018, there was a drop in energy consumption by almost 50% - 1080 kWh per year.
- After the shutdown of the solar system for domestic hot water and the installation of the FEP at the beginning of 2021, there is a preservation of the consumed electric energy (1080 kWh per year), but also a sharp drop in the consumption of solid fuel from the heating water heating installation.

One ton of wood pellets produces 4600 kW. The research and measurements made in this direction show that for 2021, nearly 700 kg of pellets or about 3266 kWh have been saved (Fig. 7).

The energy consumption after the applied measures for one year is 142.75 kWh/m². Given these data, the home remains in energy class “B” according to energy efficiency criteria (Fig. 3). The following data were received: for heating – 10,534 kWh; for DHW - 1080 kWh; for household needs – 2661 kWh.

Figure 5 shows the appearance of the installed heat pump, and Fig. 6 shows the data for electricity consumption from the heat pump for one year. It should be noted here that, in addition to heating, the unit also works for DHW.

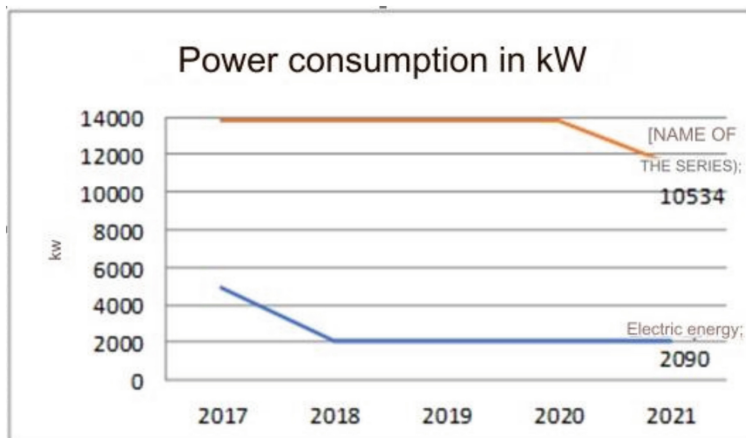


Fig. 5. Energy expenditure.

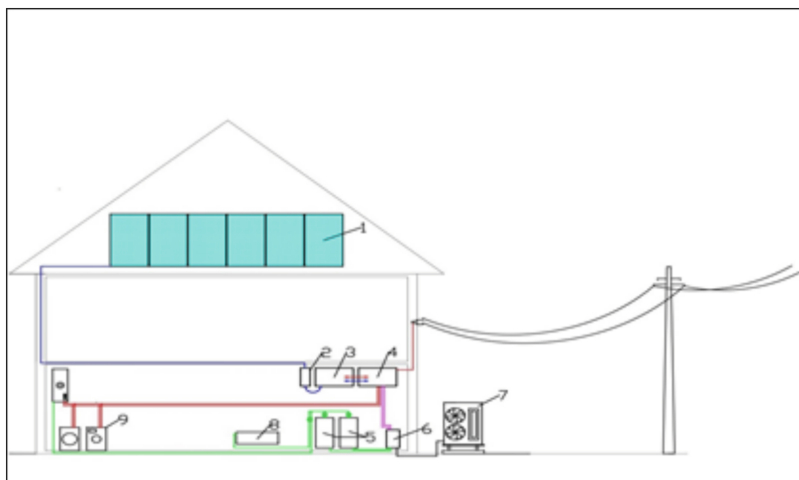


Fig. 6. Schematic diagram after heat pump installation. - 1 - photovoltaic panels; 2 - hybrid inverter; 3 - intelligent controller for managing energy flows; 4 - operating panel; 5 - buffer vessels; 6 - buffer vessel control controller; 7 - heat pump; 8 - heating; 9 - household energy consumers.

The heat pump heats DHW up to 50 °C. The boiler's electric heater is also controlled by the heat pump unit. After reaching temp. 50 °C, the heater is turned on, which only reheats the water to 65 °C. This system operation logic leads to a significant reduction in the energy consumption of the building. (Fig. 7).

The conclusion that can be drawn based on the results of the implemented improvements is that the energy consumption has decreased by 7789 kWh in one calendar year.

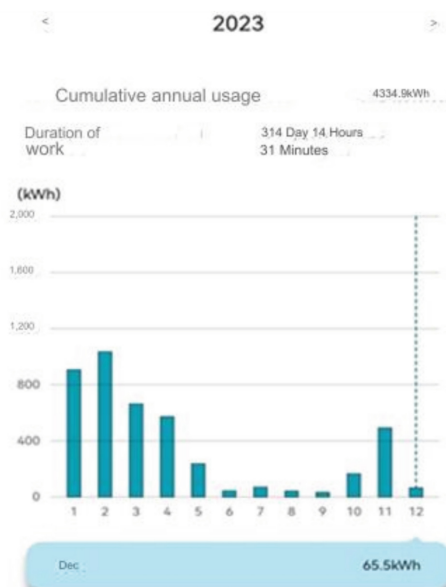


Fig. 7. The following data were obtained: for heating - 4335 kWh; for DHW - 360 kWh; for household needs - 2661 kWh.

Thus, the energy consumption of the building has a value of 73.56 kWh/m² for one year.

With these data, the home falls into energy class “A” according to energy efficiency criteria (Fig. 3).

In order to achieve high energy efficiency, measures must be taken to limit the building’s heat losses.

The next step that must be taken to increase the energy efficiency of the building is the laying of external thermal insulation.

Heat transfer coefficient U after firing and be equal to or less than 0.50 W/m²K. The measure is defined in Annex No. 3 of Ordinance No. 7 of 2004 on the energy efficiency of buildings.

The investigated building has a heat transfer coefficient of the external walls $U = 1.88$ W/m²K. In order to fulfill the condition of Regulation No. 7, GEOLAN stone wool 6 cm with a heat transfer coefficient $U = 0.035$ W/m²K must be laid. As a result, a heat transfer coefficient of the external walls $U = 0.45$ W/m²K will be achieved.

The total heat losses for the heating season (OTO kWh) for an external wall with an area of 10 m² in the Smolyan region, where DD (day degrees at 21 °C = 3300) are:

- Without thermal insulation

$$OTO = U \cdot 24h \cdot DD \cdot \frac{m^2}{1000}$$

$$OTO = 1,88 \cdot 24 \cdot 3300 \cdot \frac{10}{1000}$$

$$OTO = 1488, 96kWh$$

- With thermal insulation

$$OTO = U \cdot 24h \cdot DD \cdot \frac{m^2}{1000}$$

$$OTO = 0, 45 \cdot 24 \cdot 3300 \cdot \frac{10}{1000}$$

$$OTO = 356, 40kWh$$

where:

- U – coefficient of heat transfer;
- 24 h – 24/7;
- DD – dengradus;
- m^2 – area of the outer wall.

3 Conclusions

The comprehensive survey of the building reveals significant insights into its energy consumption patterns and the profound impact of thermal insulation on energy efficiency. The surveyed part of the building their net area of the external walls (without doors and windows) $80 m^2$. This parameter is crucial as it directly influences the building's heat retention and loss characteristics.

In the scenario without thermal insulation, the building requires approximately 11911.68 kWh to maintain an internal temperature of $21^\circ C$. This figure underscores the inherent inefficiency in buildings lacking proper insulation, as a significant amount of energy is wasted in compensating for the heat lost through the walls. Conversely, the introduction of thermal insulation dramatically reduces the energy requirement to 2851.2 kWh. This stark contrast not only highlights the effectiveness of insulation in minimizing heat loss but also underscores its role in promoting energy conservation and sustainability.

The analysis further delves into the performance of the heat pump, a critical component in the building's heating system. With a Coefficient of Performance (COP) at $-15^\circ C$ (water for heating at $+50^\circ C$) of 3.57, the energy consumption to maintain a temperature of $21^\circ C$ in the building is calculated to be 798.65 kWh/ m^2 . This figure is indicative of the heat pump's efficiency, even under challenging conditions, and its role in ensuring a comfortable indoor environment.

The energy consumption is further dissected into individual components, namely, heating (798.65 kWh), Domestic Hot Water (DHW) (360 kWh), and household needs (2661 kWh). This breakdown provides a detailed understanding of the energy distribution within the building, allowing for targeted strategies to optimize consumption and reduce costs.

The implementation of thermal insulation and an efficient heating system culminates in an annual energy consumption of approximately $38.19 kW/m^2$. This figure is not just

a testament to the effectiveness of the energy-saving measures but also a benchmark for sustainable building practices. The building's adherence to these stringent energy standards earns it a place in energy class "A+", a classification that denotes superior energy efficiency.

Moreover, the building's exemplary performance in energy conservation and efficiency propels it into the prestigious category of "Near Zero Energy Building". This status is not merely a label but a reflection of the building's alignment with contemporary environmental goals and its commitment to reducing its carbon footprint. The designation underscores the building's role as a model for sustainable construction and its contribution to the broader agenda of energy conservation and environmental stewardship.

In conclusion, the detailed analysis of the building's energy consumption patterns, the profound impact of thermal insulation, and the efficiency of the heating system collectively underscore the building's exemplary performance in energy conservation. The building's classification into energy class "A+" and its status as a "Near Zero Energy Building" are testaments to its alignment with the highest standards of energy efficiency and environmental sustainability. This case study serves as a benchmark for future construction projects, emphasizing the critical role of energy-efficient design and technology in shaping sustainable and environmentally responsible buildings.

References

1. Karlsson, A., Lindkvist, C., Wojtczak, E., Stachurska-Kadziak, K., Holm, D., Sornes, K.: Common barriers and challenges in current nZEB practice in Europe (2013)
2. California Energy Commission: Integrated Energy Policy Report (2013)
3. Ecofys, Politecnico di Milano, & University of Wuppertal, Towards nearly zero-energy buildings: Definition of common principles under the EPBD, Köln, Germany (2013)
4. Zaerov, E.: Use Of Perovskit In Solar Energy, Yearbook BFU 2018, Volume XXXVIII, pp. 255–260 (2018). ISSN: 1311-221X
5. Zaerov, E.: Study of the potential for hydrogen production with photovoltaic power plant and fuel cell Yearbook BFU 2015, volume XXXI, pp. 36–39 (2015). ISSN: 1311-221X
6. Sartori, I., Napolitano, A., Voss, K.: Net zero energy buildings: a consistent definition framework. *Energy Build.* (48), 220–232 (2012)
7. IPCC working group, climate Change 2014: Mitigation of Climate Change (Chapter 9 Buildings), Berlin, Germany (2014)
8. Faludi, J., Lepech, D.M., Loisos, G.: Using life cycle assessment methods to guide architectural decision-making for sustainable prefabricated modular buildings. *J. Green Build.* 3(7), 151–170 (2012)
9. Deru, M., Torcellini, P.: Source Energy and Emission Factors for Energy Use in Buildings, Technical Report NREL/TP-550-38617. Golden, CO: National Renewable Energy Laboratory (2007)
10. Torcellini, P., Pless, S., Deru, M., Crawley, D.: Zero Energy Buildings: A Critical Look at the Definition, National Renewable Energy Laboratory (NREL), Pacific Grove, California (2006)
11. Torcellini, P., Pless, S., Deru, M.: Zero Energy Buildings: A Critical Look at the Definition Preprint. ACEEE Summer Study (2006)
12. Silviya, A., Letskovska, N.A., Mollov Eldar, D., Zaerov: Inspection of buildings for energy efficiency. In: ICTRS 2021, November 15, 16, 2021, Virtual Conference, Bulgaria, pp. 37–42. ACM (2021). ISBN 978-1-4503-9018-7/21

13. Dolchinkov, R., Yovkov, A., Todorov, V., Ventsislavov, K.: Integrated platform for vehicle charging based on renewable energy resources. In: 12th International Conference, ICTRS 2023, Rhodes, Greece, 18–19 September 2023, Proceedings, Softcover (2023). ISBN 978-3-031-49262-4, eBook ISBN 978-3-031-49263-1
14. Dolchinkov, R.: Mechanisms and machines in RES. Electronic journal of CITN for computer science and communications, issue 3, pp. 31–42 (2013). ISSN 1314-7846
15. Matsankov, M., Ivanova, M.: Selection of optimal variant of hybrid system under conditions of uncertainty. In: The 2nd International Conference on Electrical Engineering and Green Energy Roma, Italy, 28–30 June 2019, E3S Web of Conferences, vol. 115, p. 01007 (2019). <https://www.e3s-conferences.org/articles/e3sconf/abs/2019/41/contents/contents.html>
16. Dolchinkov, R., Georgieva, P.: Efficiency of solar tracking systems. BFU Yearbook, volume XXVIII, pp. 243–255 (2012). ISSN 1311-221-X
17. Dolchinkov, R.: Teaching methods in computer design of technological systems, Seville, Spain, 6th International Conference of Education, Research and Innovation, pp. 5785–5795 (2013). ISBN 978-84-616-3849-9
18. Dolchinkov, R., Bangev, M.: Prevention of fires caused by electric arc. In: International Scientific Conference Blue Economy and Blue Development, pp. 441–451 (2018). ISBN: 978-619-7126-57-0
19. Zaerov, E.: Increase solar panel performance with flat reflectors, BFU - YEARBOOK Volume XLIV, pp. 290–296 (2021). ISSN: 1311-221X

Short Paper



Drone Technology and External Contextual Factors

Boris Shishkov^{1,2,3}(✉)

¹ Institute of Mathematics and Informatics, Bulgarian Academy of Sciences, Sofia, Bulgaria

² Faculty of Information Sciences, University of Library Studies and Information Technologies,
Sofia, Bulgaria

³ Institute IICREST, Sofia, Bulgaria

b.b.shishkov@iicrest.org

Abstract. Drone technology is applied in many domains to date, with clear societal benefits. Nevertheless, “the other side of the coin” concerns risks related to safety, privacy, accountability, and so on. Since we claim to be missing a sound and widely agreed-upon approach to tackle this problem, we are proposing our views accordingly, considering the context-awareness paradigm and its possible strengths with regard to drone technology. In this we are firstly addressing the challenge of maximizing the user-perceived effectiveness and the challenge of maintaining optimal system-internal processes; on top of that we are especially considering the external contextual factors, including rules, law-compliance, and public values. We are presenting just small illustrative examples and thorough validation of our proposed ideas is left for future research, since in the current paper we are reporting research-in-progress. Hence the contribution of the paper is two-fold – we not only align the context awareness paradigm to the drone technology application but we also make a special stress on the external contextual factors as claimed to be relevant with regard to the abovementioned problem.

Keyword: Drone technology · Context awareness · External factors

1 Introduction

Unmanned aerial vehicles [1] and unmanned underwater vehicles [2], collectively referred to as DRONES, both have an increasing application potential as it concerns numerous domains [3] - from monitoring in areas affected by disruptive events and support of rescue operations [4], through surveillance for the benefit of security servicing, agriculture-related tasks, weather forecasting, and so on [5], to advanced military missions [6]. Hence, drones are currently of wide societal value. Nevertheless, “the other side of the coin” concerns risks related to safety [9], privacy-violation [7], inadequate accountability [8], and so on. Thus, drone technology poses both BENEFITS and CONCERNS. Further, we argue that the ICT (Information and Communication Technology) Community still misses sound and widely agreed-upon approaches to tackle this problem [3]. Finally, we opt for considering CONTEXT AWARENESS as a useful and relevant paradigm in this regard [10]; the reasons for this choice are two-fold: (i) Risks often

concern things that are “outside” the done, which means that they are contextual issues; (ii) The need for constant behavior adaptation makes a drone a typical context-aware system.

In previous work, we have considered “hard concerns” vs “soft concerns”, with regard to context-aware systems - As “**HARD**” concerns we consider the drives towards maximization of the user-perceived effectiveness and system internal optimization, in the sense that any (technical) system is to be expected to fulfill some user needs and to also take care of its own “health”; As “**SOFT**” concerns we consider the drives towards keeping the (ICT) servicing in concert with societal values, norms, and regulations, in the sense that unlike the *hard concerns* (that are obviously essential in realizing a technical design), such societal issues come “in addition” even though they are not to be considered less important [11]. In the current paper, we label the soft concerns **EXTERNAL CONTEXTUAL FACTORS**.

In Sect. 2, we address the hard concerns with regard to drone technology, and in particular – the challenge of maximizing the user-perceived effectiveness and the challenge of maintaining optimal system-internal processes.

On top of that we emphasize (in Sect. 3) the external contextual factors, considering them most relevant to the risks mentioned in the first paragraph of the current section.

As it concerns validation, it is left for future research since this is a position paper reflecting research-in-progress; still we have provided small illustrative examples in the abovementioned sections.

Hence, the contribution of the current paper is two-fold – we not only align the context awareness paradigm to the drone technology application but we also make a special stress on the external contextual factors claimed to be relevant with regard to the mentioned problem.

2 Hard Concerns

As mentioned in the Introduction, we need a *conceptual frameworks* specifically to be able to assess, *at design time*, the utility of a context-aware system in an intended *context*. With such an assessment the designers and other stakeholders can decide whether the proposed system is ready for transfer to practice, or whether another design cycle for further improvement should be entered. In this way it is possible to reduce the risk that the *context-aware* system, once implemented in its *context*, does not fulfil the expectations of the stakeholders. In this regard, we will address *context-aware* systems aiming at better serving the user needs and aiming at maintaining optimal internal processes.

2.1 Conceptualizations

As a problem theory for *context-aware* systems we postulate that *end-users* (*users*, for short) of *information systems* often have different needs for services provided by such systems, where different needs correspond to different context situations. *Context-aware* (information) systems are a “treatment” for this problem if they can provide **context-specific services to users in accordance to their context-dependent needs**. “Context” here is the *context* of the *context-aware* system, where the former is a given

(i.e., not designed) and the latter is the object of design. A *context-aware* system that is transferred to practice would interact with its context. Two kinds of interactions can be distinguished: one for *collecting data on the context* and another one - for *delivering a service* that matches the *context*. The fact that the *service* is delivered to a *user* means that the user is part of the context. This makes perfect sense, as the *part-of* relation is an essential prerequisite for the system we want to design, viz. to make a connection between what the *context* is and what a *user* needs [10].

We frame the design problem with the diagram in Fig. 1. The diagram shows that a **user**, being *part of* a **context**, has *one or more user needs* (or sets of *user needs*), where each distinguished *user need* results from a corresponding unique **context situation**. A *context* can be conceived as a *temporal composition of one or more context situations*, where each *context situation* has a unique set of *properties* that collectively are relevant to a specific *user need*. A useful **context-aware system** is able to detect the *context situation* at hand and then offers one or more **situation-specific services** that satisfy the *needs* of the *user* being in, or experiencing, that situation.

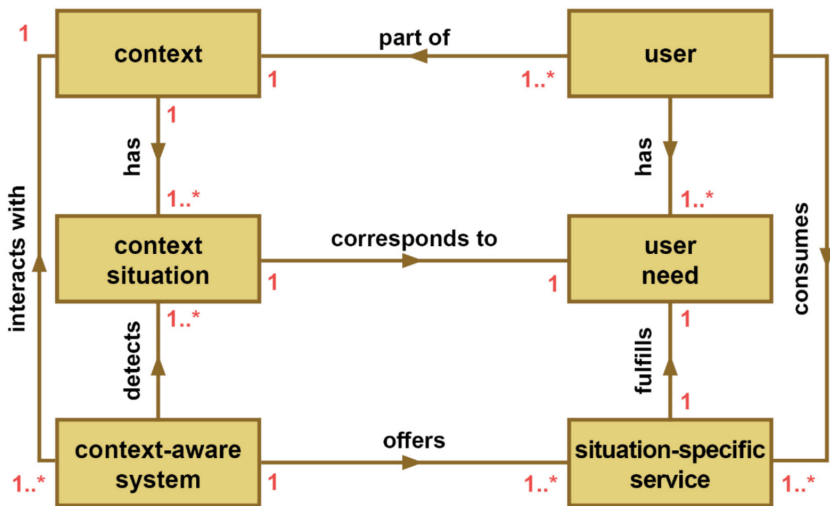


Fig. 1. Maximizing the user-perceived effectiveness - framing the problem of context awareness (Source: [10], p. 122; ©2021, Springer-Cham; reprinted with permission)

Further, it might be that “system health” is also of crucial importance, next to maximizing the user-perceived effectiveness, at least because in order to be capable of servicing the user adequately, the system itself should be in adequate condition – this means that optimal system-internal processes should be maintained. This means considering different process optimization needs for different context situation – see Fig. 2.

The diagram suggests that a **system**, being *part of* a **context**, has *one or more system needs* (or sets of *system needs*), where each distinguished *system need* results from a corresponding unique **context situation**. Each *context situation* has a unique set of *properties* that collectively are relevant to a specific *system need*. An adequate **system** should be capable of detecting the *context situation* at hand and then in the ability to

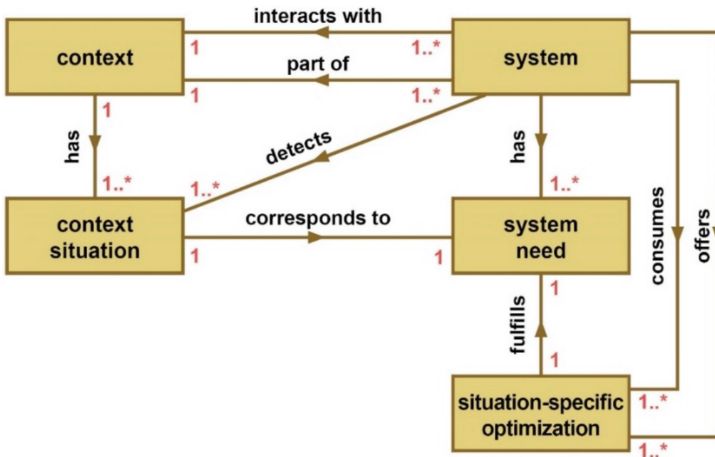


Fig. 2. Optimizing system-internal processes - framing the context awareness problem

offer one or more **situation-specific optimizations** that satisfy the *needs* of the *system* itself being in, or experiencing, that situation.

2.2 Exemplifications

In this section we will provide partial exemplifications of the above conceptualizations:

[**BORDER MONITORING**] A drone (SYSTEM) is fulfilling a mission in the sky, monitoring a land border area, for the benefit of a border police officer (USER). It is possible for the system to “know” if the user is in the local police station, “currently” using his or her desktop computer (Context Situation BM1) or the user is in a police vehicle, “currently” using the car multimedia platform (Context Situation BM2), or the user is walking in the area (Context Situation BM3). Context Situation BM1 suggests that much media-rich content can be transmitted to the user and the user would be capable of using it of full value, counting on powerful networking, hardware, and software. Context Situation BM2 suggests that the system does not do many transmissions of large data volumes (because of less powerful facilitation in the police vehicle), instead: more processing is done at the drone side and/or in the Cloud, such that mostly “summaries” are sent to the user. Context Situation BM3 suggest not only that mostly summaries are to be sent to the user (because the user only would count on his/her mobile device) but also the drone should send warnings if the border police officer is “too close” to identified trespassers (for example) that makes the user vulnerable. There may be also other context situations: the border police officer is neither using his or her desktop computer at the local police station, not is (s)he in his/her police vehicle, nor is (s)he using his or her mobile device – if this is because the border police officer is outside working hours, then the drone should identify the relevant border police officer to communicate with; otherwise, it should be assumed that something unexpected has happened (either an incident, or an out-of-battery situation, or something else) and the drone should send alarm to the corresponding police commander. Yet another possible context situation is

when the user requires something specific in a particular moment (for example: keep monitoring but in a particular direction) – then the drone should respond to this particular user need and provide situation-specific servicing accordingly. Finally, if the user has sent off an “emergency – need help” message, then the drone should identify the location of the user and establish all colleagues in close proximity to whom to send SOS triggers accordingly. There may be also other relevant context situations that are not discussed for the sake of brevity. This exemplification concerns context-aware servicing (in general) and maximization of the user-perceived effectiveness (in particular).

[DELIVERY OF GOODS] A drone (SYSTEM) is fulfilling a mission, aiming at delivering goods from Point A to Point B. One aspect that concerns system-internal processes is energy – the drone counts on a battery for being able to maintain these processes, for the sake of fulfilling the mission. Nevertheless, when the distance between Point A and Point B is not small, “undesirable” weather (such as strong wind, for example) might lead to more battery consumption than planned/calculated at the beginning of the mission. This in turn would change the so called “point of no return”, determining a closer (than planned) point whose passing by would result in drone’s inability to fly back to Point A (because of not enough battery power). Hence, initially, the drone is in normal state (Context Situation DG1) in which Point B appears to be between Point A and the *point of no return*. This could change if, for example, strong wind appears, causing the drone to use more energy in maintaining the flight, that in turn would lead to a critical state (Context Situation DG2) in which the re-calculated *point of no return* is already between Point A and Point B. Context Situation DG1 suggests that the drone mission could continue because a successful delivery (that would lead to maximizing the user-perceived effectiveness) would be followed by smooth mission completion (drone’s returning back to Point A) and in turn means good “system health” in the sense that all system-internal processes were optimal during the mission. Context Situation DG2 suggests that the drone would better fly back to Point A because maximizing (as much as POSSIBLE) the user-perceived effectiveness could wait for another mission; still maintaining the “system health” would be achieved. There may be also other relevant context situations that are not discussed for the sake of brevity. This exemplification concerns context-aware servicing (in general) and optimization of system-internal processes (in particular).

In summary, this section has presented background content featuring the so called *hard concerns* – *maximizing the user-perceived effectiveness* and *optimizing system-internal processes*, by providing conceptualizations and exemplifications accordingly. We call this “background content” because we argue that explicitly or implicitly *effectiveness* and *optimization* are woven in most drone system designs to date. Further, as it concerns the presented conceptualizations, maximizing the user-perceived effectiveness has been considered in previous work [10] while our explicit discussion (see above) on optimizing system-internal processes (see Fig. 2) is claimed to be an original contribution of the current paper. Still, we consider all this as a background upon which we would address the soft concerns, called in the paper “external contextual factors” – see Sect. 3. Finally, even though external contextual factors have been partially addressed in previous work (for example: addressing accountability-related concerns [8]) we argue

that we are still missing a holistic study in this direction, and Sect. 3 is expected to be contributing to filling in this gap.

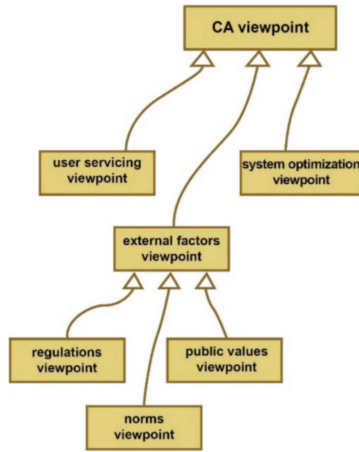


Fig. 3. Context awareness viewpoints (Source: [11], p. 255; ©2024, Springer-Cham; reprinted with permission)

3 External Contextual Factors

In this section, we will firstly provide a general introduction to external contextual factors and then we will consider a corresponding conceptualization and an exemplification, related to it.

3.1 External Contextual Factors – General Introduction

The three context awareness viewpoints, considered in previous work [11], are helpful in introducing external contextual factors – see Fig. 3.

As the figure suggests, external contextual factors may be about **REGULATIONS**, about **NORMS**, and/or about **PUBLIC VALUES** (not claiming exhaustiveness, we limit our scope to cover these three types): (i) Considering **regulations** concerns the goal of possibly integrating holistically legal compliance in the design of a drone system, enriched by “reasoning” that would be helpful in resolving tensions between legal requirements; said otherwise, that is about context-specific solutions to achieve legal compliance. An essential challenge in this regard is accounting for all relevant legal frameworks and synthesizing accordingly guidelines for legal reasoning. Unfortunately, an overemphasis of legal compliance by design might hamper the development of innovative artifacts [12]. (ii) Since a drone, even though often navigated from a ground station, may appear to be autonomous, considering **norms** concerns governing the drone’s behavior and norms themselves represent the rules and patterns of behavior, either formal or informal, explicit or implicit, existing within a society, an enterprise, or even a

small group of people working together to achieve a common goal [13]. (iii) Considering **public values**, such as safety, privacy, accountability, and trust, concerns the need for sticking to such widely accepted societal categories [14] – this is especially relevant to drone technology because in some situations, a drone could easily cause damages related to safety, privacy, and so on, that in turn would pose the need for tackling traceability, accountability, and so on.

In the remainder of the current paper, we would just consider external contextual factors, not distinguishing among regulations, norms, and public values – addressing each of them separately in relation to drone technology is left for future research.

3.2 Conceptualization

Properly addressing external contextual factors would mean considering different external (that are neither related to the drone system nor to the user) needs for different context situation – see Fig. 4.

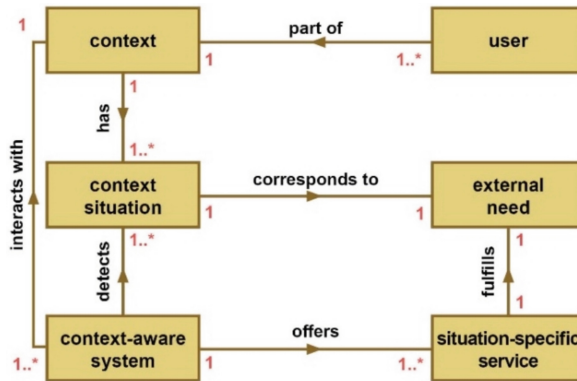


Fig. 4. Considering external factors - framing the context awareness problem

The diagram suggests that there are one or more **external needs** (or sets of *external needs*) where each distinguished *external need* results from a corresponding unique **context situation** (for example: in a particular situation, it is against the Law that the drone flights further or the drone should respect the privacy of nearby people (not photographing their faces)). Each *context situation* has a unique set of *properties* that collectively are relevant to a specific *external need*. An adequate **system** should be capable of detecting the *context situation* at hand and then in the ability to offer one or more **situation-specific services** (directed to the user) in whose realization the system is conforming with the external needs.

3.3 Exemplification

In this section we will provide partial exemplification of the above conceptualization:

[**SEA LIFEGUARD**] A drone (SYSTEM) is fulfilling a mission, aiming at monitoring a beach-sea area within a pre-defined perimeter; any item (a person, a boat or something else) that is at least 300 m away from the coast and at the same time – more than 50 m away from the closest “neighboring” item, is to be considered by the drone. Initially, the drone is in normal state (Context Situation SL1) in which there is no item to be approached. This could change if, for example, an item is spotted (for example, a boat) that is 400 m away from the coast with no other items within 50 m around it (Context Situation SL2). Context Situation SL1 suggests that the drone is just monitoring with no need to “zoom in” – hence, no external-contextual-factors-related issues are to be considered. Context Situation SL2 suggests that the drone would firstly need to approach the spotted item and then “zoom in”, such that a high-quality video is captured that is to be immediately sent to a corresponding costal Lifeguard Hub; the persons there would analyze the video and decide whether or not rescue activities are needed. Imagine that in the particular country, it is forbidden by law to photograph identification labels of boats unless an offence is taking place; imagine also that privacy standards “push” for not photo/video recording faces of persons without a corresponding permission. Hence, the drone should identify the boat identification number and also the faces of persons who are on the boat (if any); then upon capturing the video, the drone should “make sure” that the boat identification and the faces are both blurred, such that it is guaranteed that no boat identification details and no facial data are transmitted. There may be also other relevant context situations that are not discussed for the sake of brevity.

4 Conclusions

Even though drones are much useful to Society to date, there are usability risks that concern safety, privacy, accountability, and so on. Since those issues mostly concern the drone environment and also because a drone is considered a typical context-aware system, we have aligned the context awareness paradigm to the drone technology application, emphasizing on the external contextual factors. In particular: in Sect. 2 we have addressed the context awareness problem (superimposing it to drone technology) in two perspectives, namely – maximizing the user-perceived effectiveness and optimizing system-internal processes; on top of that, we have considered in more detail the external contextual factors perspective in Sect. 3.

In this, partially referring to previous work, we have provided conceptualizations followed by corresponding exemplifications. With these exemplifications not counting for proof-of-concept of full value and because this paper is reflecting research-in-progress, validation is planned for future research. We plan as future work also to tackle in more detail (with keeping the link to drone technology) each of the three types of external contextual factors considered in Sect. 3, namely – regulations, norms, and public values. We argue that an important challenge here is balancing this with possible external influences (mostly related to drone detection systems [15–19]) because a drone could just enter the scope of a drone detection system; then it is possible that the drone detection system “forces” the drone for actions (for example: forcing the drone to fly in a particular direction) that lead to an “unintended” violation of public values (for example: flying in a particular direction, forced by a drone detection system, the drone could “undesirably”

appear in an area where it is disturbing persons (privacy violation)). In this regard, we also need broader discussions concerning overarching regulations that would adequately govern the “relations” between a drone and a drone detection system.

References

1. IEEE Draft Standard for Drone Applications Framework. In: P1936.1, 2020, pp. 1–29 (2021)
2. Yar, G.N.A.H., Ahmad, A., Khurshid, K.: Low cost assembly design of unmanned underwater vehicle (UUV). In: International Bhurban Conference on Applied Sciences and Technologies (IBCAST), pp. 829–834. IEEE (2021)
3. Shishkov, B., Garvanova, G.: A review of pilotless vehicles. In: Shishkov, B., Lazarov, A. (eds.) Telecommunications and Remote Sensing. ICTRS 2023. Communications in Computer and Information Science, vol. 1990. Springer, Cham (2023)
4. Shishkov B., Branzov, T., Ivanova, K., Verbraeck A.: Using drones for resilience: a system of systems perspective. In: Proceedings of 10th International Conference on Telecommunications & Remote Sensing (ICTRS 2021). ACM, New York (2021)
5. Saha, A., Kumar, A., Sahu, A.K.: FPV drone with GPS used for surveillance in remote areas. In: 2017 Third International Conference on Research in Computational Intelligence and Communication Networks (ICRCICN), Kolkata, India, pp. 62–67 (2017)
6. Lee, M., et al.: A study on the advancement of intelligent military drones: focusing on reconnaissance operations. *IEEE Access* **12**, 55964–55975 (2024)
7. Gabriëlsson, J., Bugeja, J., Vogel, B.: Hacking a commercial drone with open-source software: exploring data privacy violations. In: 2021 10th Mediterranean Conference on Embedded Computing (MECO), Budva, Montenegro, pp. 1–5 (2021)
8. Shishkov, B., Hristozov, S., Janssen, M., Van den Hoven, J.: Drones in land border missions: benefits and accountability concerns. In: Proceedings of the 6th International Conference on Telecommunications and Remote Sensing (ICTRS 2017). ACM, New York (2017)
9. Okutake, T., Uchida, N., Yamamoto, N.: A collaborative safety flight control system for multiple drones. In: 2016 10th International Conference on Innovative Mobile & Internet Services in Ubiquitous Computing (IMIS), Fukuoka, Japan, pp. 371–375 (2016)
10. Shishkov, B., van Sinderen, M.: Towards well-founded and richer context-awareness conceptual models. In: Shishkov, B. (eds.) Business Modeling and Software Design. BMSD 2021. Lecture Notes in Business Information Processing, vol. 422. Springer, Cham (2021)
11. Shishkov, B.: Context awareness and external factors. In: Shishkov, B. (eds.) Business Modeling and Software Design. BMSD 2024. Lecture Notes in Business Information Processing, vol. 523. Springer, Cham (2024)
12. Hoess, A., Pocher, N., Roth, T.H., Fridgen, G.: Towards a design science research process for legal compliance by design. In: PACIS 2024 Proceedings 3 (2024). https://aisel.aisnet.org/pacis2024/track04_dessci/track04_dessci/3
13. Stamper, R., Liu, K., Hafkamp, M., Ades, Y.: Signs plus norms – one paradigm for organizational semiotics. In: The Proceedings of the 1st International Workshop on Computational Semiotics, 26–27 May 1997, Paris, France (1997)
14. Veluwenkamp, H., van den Hoven, J.: Design for values and conceptual engineering. *Ethics Inf. Technol.* **25**, 2 (2023). <https://doi.org/10.1007/s10676-022-09675-6>
15. Garvanov, I., Garvanova, M., Ivanov, V., Chikurtev, D., Chikurteva, A.: Drone Detection Based on Image Processing, 23rd International Symposium on Electrical Apparatus and Technologies (SIELA), Bourgas, Bulgaria, pp. 1–5 (2024). <https://doi.org/10.1109/SIELA61056.2024.10637850>

16. Garvanov, I., Pergelova, P., Nurdaulet, N.: Acoustic system for the detection and recognition of drones. In: Shishkov, B., Lazarov, A. (eds.) *Telecommunications and Remote Sensing. ICTRS 2023. Communications in Computer and Information Science*, vol. 1990. Springer, Cham (2023)
17. Garvanov, I., Garvanova, M., Borissova, D., Garvanova, G.: A model of a multi-sensor system for detection and tracking of vehicles and drones. In: Shishkov, B. (eds.) *Business Modeling and Software Design. BMSD 2023. Lecture Notes in Business Information Processing*, vol. 483. Springer, Cham (2023)
18. Garvanov, I., Garvanova, M., Ivanov, V., Lazarov, A., Borissova, D., Kostadinov, T.: Detection of unmanned aerial vehicles based on image processing. In: Shishkov, B., Lazarov, A. (eds.) *Telecommunications and Remote Sensing. ICTRS 2022. CCIS*, vol. 1730. Springer, Cham (2022)
19. Garvanov, I., Kanev, D., Garvanova, M., Ivanov, V.: Drone detection approach based on radio frequency detector. In: *2023 International Conference Automatics and Informatics (ICAI)*, Varna, Bulgaria, pp. 230–234 (2023). <https://doi.org/10.1109/ICAI58806.2023.10339072>

Author Index

B

Borissova, Daniela 60

D

Dolchinkov, Radostin 75

G

Garvanov, Ivan 28, 60

Garvanova, Magdalena 28, 60

K

Kerimbayev, Nurassyl 60

L

Lazarov, Andon 16

Letskova, Silvia 75

Lodkadhiev, Kristian 75

Lubaba, Samiha 3

M

Maltseva, Olga A. 43

Menlibay, Zhanbota 60

Mihaylov, Hristo 87

N

Nikitenko, Tatyana V. 43

P

Petersen, Brent R. 3

S

Seymenliyski, Kamen 75, 87

Shishkov, Boris 103

Simionov, Radoslav 75, 87

T

Todorov, Velizar 87

Y

Yovkov, Atanas 87

Z

Zaerov, Eldar 87